FINAL TECHNICAL REPORT

AWARD NUMBER: G19AP00093

Development of a liquefaction triggering procedure for megathrust events

by

Adrian Rodriguez-Marek,
Russell A. Green and Balakumar Anbazhagan

Period of Award (with no-cost extension):
August 10, 2019 to July 31, 2021

Principal Investigators:

Adrian Rodriguez-Marek
Russell A. Green

Virginia Polytechnic Institute and State University
Dept. of Civil and Environmental Engineering
750 Drillfield Drive
214 Patton Hall
Blacksburg, VA 24061
(540) 231-5778 (phone)
(540) 231-7532 (fax)
adrianrm@vt.edu

Research supported by the U. S. Geological Survey (USGS), Department of Interior, under USGS award number G19AP00093. The views and conclusions contained in this document are those of the authors and should not be interpreted as necessarily representing the official policies, either expressed or implied, of the U. S. Government.

ABSTRACT

Liquefaction is one of the major causes of ground failures during an earthquake. Recent evidence shows that the existing variants of the “simplified” liquefaction evaluation procedure lead to inaccurate results for megathrust earthquakes in subduction interfaces. To overcome this drawback and to achieve better prediction of liquefaction cases in subduction zones, this research intends to develop new empirical models that could be used for the prediction of liquefaction triggering in subduction zones. Towards this goal, new models for number of equivalent cycles (n_{eq}) and stress-reduction factor (r_d) have been proposed. The models are developed by regressing site response data obtained from 254 pairs of subduction ground motions and 77 representative soil profiles. To account for tectonic differences and magnitude scaling, separate models are developed for interface and intraslab earthquakes. The uncertainties involved in the proposed models are quantified through standard deviations of regression coefficients, event, site, and residual terms. The resulting models differ from other published models, especially the model for number of equivalent cycles. It was found that n_{eq} is greatly influenced by the fundamental site period. The model for r_d predicts higher values at shallow depths and lower values at deeper layers than other published models. Comparing the factors of safety against liquefaction with those from other existing models revealed that the use of models proposed in this research is more likely to reduce the “false positives” in liquefaction predictions, especially when design ground motion acceleration is high.

Table of Contents

List of Figures

List of Tables

Chapter 1

Introduction

Liquefaction is the phenomenon in which the contractive tendencies of saturated sandy soils under shear loading leads to an increase in excess pore pressures and the commensurate reduction in effective stress. The reduction in effective stress is a result of the complete or partial transfer of overburden stress to the pore fluid. The complete transfer of overburden stress to the pore fluid implies a near-zero shear strength of the soil and is called initial liquefaction or liquefaction triggering. This causes the soil to behave like a liquid (with significantly reduced shear strength) and potentially can lead to various ground failures including foundation failures, lateral spreading, and sand boils. In the case of earthquake-induced liquefaction, liquefaction is initiated by the earthquake shaking.

Earthquake-induced liquefaction poses significant challenges to geotechnical engineers around the world. The damaging effects of liquefaction was brought into the attention of the researchers after the 1964 Niigata, Japan, and Anchorage, Alaska earthquakes. Since then, there are numerous documented case histories of infrastructure damage caused by liquefaction around the world (Bennet, 1989; Holzer et al. 1999; Cubrinovski et al. 2011; Candia et al. 2017). Some of the well-known liquefaction cases that led to significant damage to infrastructure include the ground failures observed in 1971 San Fernando Valley earthquake, 1994 Northridge earthquake, 2011 Christchurch earthquake, and 2015 Illapel earthquake. Considering the hazard due to liquefaction and its risk to communities around the world, it is of utmost importance to reliably predict liquefaction triggering at a given site. Though there are several methodologies to evaluate liquefaction potential, recent evidence shows that the predictions using these methodologies can be inaccurate, especially in subduction zones. Building on this observation, this research focusses on developing a new model to evaluate liquefaction triggering due to subduction zone earthquakes. This chapter presents the objectives and motivation for the research detailed in this report.

1.1 Motivation

Considering the devastating effects of liquefaction, several studies have been performed to understand the liquefaction phenomenon and to mitigate its effects. Towards this goal, it is important to be able to predict liquefaction triggering at a given site. Currently, the most commonly used approach to evaluate liquefaction potential is the semi-empirical, stress-based "simplified" procedure (Cetin et al. 2004; Kayen et al. 2013; Boulanger and Idriss, 2014). While the recent variants of the simplified procedure produce similar results for scenarios that are well covered by the data, their predictions deviate for other scenarios (e.g., large magnitude subduction events). As a result, use of these existing procedures for sites that could be potentially affected by a subduction earthquake becomes questionable. This speculation has been reinforced through back analysis of liquefaction case histories of 2010 M_w8.8 Maule and 2015 M_w8.3 Illapel earthquakes in Chile (Montalva and Ruz, 2017) wherein majority of the "no liquefaction" scenarios are mispredicted. These mispredictions are potentially due to the empirical parts in the "simplified" procedure that originate from the data from shallow-crustal earthquakes in active tectonic regimes. The differences in tectonic regimes manifest in the empirical parts used in the "simplified" procedure. Therefore, this research intends to address this issue by developing a new liquefaction evaluation model for subduction zones. The potential for large subduction earthquakes to impact large parts of the world (the Pacific Northwest in the United States, Japan, west coast of South America, and New Zealand) and the lack of reliable predictions of liquefaction triggering for these regions provide the motivation for this research.

1.2 Objectives

The overall objective of this research is to develop a liquefaction triggering evaluation procedure for large subduction events. As discussed before, the differences in tectonic regimes manifest in the empirical components of the procedure, especially the Magnitude Scaling Factor (MSF) and the stress-reduction factor (r_d). Therefore, large emphasis in this research has been placed on the development of subduction zone-specific MSF and r_d relationships. The new relationships are developed using representative ground motions and geologic profiles. The overall objective of this research will be accomplished by incorporating the newly developed empirical relationships in the “unbiased” simplified procedure outlined in Green et al. (2019).

1.3 Organization of the report

Chapter 2 provides a brief background information on the important concepts pertaining to this research. It provides relevant information on the distinctive characteristics of subduction zone ground motions and also provides a brief outline of the “simplified” liquefaction evaluation procedure and its empirical parameters. Chapter 3 is the main body of the report that details all the work done in this research along with new findings and observations. It presents the new correlations for number of equivalent cycles (n_{eq}) and stress reduction factor (r_d). Chapter 4 summarizes the research findings and their significance. Finally, additional research details regarding the ground motions and soil profiles compiled in this study are provided in the appendices.

References

Bennett, M.J., 1989. Liquefaction analysis of the 1971 ground failure at the San Fernando Valley Juvenile Hall, California. Bulletin of the Association of Engineering Geologists, 26(2), pp.209-226.

Boulanger, R.W. and Idriss, I.M., 2014. CPT and SPT based liquefaction triggering procedures. Report No. UCD/CGM.-14/01, Center for Geotechnical Modeling, Department of Civil and Environmental Engineering, University of California at Davis, 134 pp.

Candia, G., De Pascale, G.P., Montalva, G. and Ledezma, C., 2017. Geotechnical aspects of the 2015 Mw 8.3 Illapel megathrust earthquake sequence in Chile. Earthquake Spectra, 33(2), pp.709-728.

Cetin, K.O., Seed, R.B., Der Kiureghian, A., Tokimatsu, K., Harder Jr, L.F., Kayen, R.E. and Moss, R.E., 2004. Standard penetration test-based probabilistic and deterministic assessment of seismic soil liquefaction potential. Journal of Geotechnical and Geoenvironmental Engineering, 130(12), pp.1314-1340.

Green, R.A., Bommer, J.J., Rodriguez-Marek, A., Maurer, B.W., Stafford, P.J., Edwards, B., Kruiver, P.P., De Lange, G. and Van Elk, J., 2019. Addressing limitations in existing ‘simplified’liquefaction triggering evaluation procedures: application to induced seismicity in the Groningen gas field. Bulletin of Earthquake Engineering, 17(8), pp.4539-4557.

Holzer, T.L., Bennett, M.J., Ponti, D.J. and Tinsley III, J.C., 1999. Liquefaction and soil failure during 1994 Northridge earthquake. Journal of Geotechnical and Geoenvironmental Engineering, 125(6), pp.438-452.

Kayen, R., Moss, R.E.S., Thompson, E.M., Seed, R.B., Cetin, K.O., Kiureghian, A.D., Tanaka, Y. and Tokimatsu, K., 2013. Shear-wave velocity–based probabilistic and deterministic assessment of seismic soil liquefaction potential. Journal of Geotechnical and Geoenvironmental Engineering, 139(3), pp.407-419.

Montalva, G. and Ruz, F., 2017. Liquefaction Evidence in the Chilean Subduction Zone. Proceedings from 3rd International conference on Performance Based Design in Earthquake Geotechnical Engineering. The International Society for Soil Mechanics and Geotechnical Engineering, Vancouver.

Chapter 2

Background

This chapter provides a brief outline of the concepts and background information necessary to understand the research presented in this report. First, a short discussion is presented on the characteristics of subduction zone ground motions and how they differ from motions from other tectonic regimes. This is followed by an overview of the “simplified” liquefaction evaluation procedure and its shortcomings as described in Green et al. (2019). Finally, the Magnitude Scaling Factor (MSF) and stress-reduction factor (r_d) are discussed in more detail along with a review of previous studies.

2.1 Subduction zone ground motions

According to the theory of plate tectonics, the tectonic plates in the earth’s crust move around due to, among other mechanisms, the convectional currents originating in the Mantle (layer of the earth beneath the crust). The plate movements cause them to collide (convergent boundary), move away (divergent boundary) or slide past (transform boundary) each other. Subduction is a process that takes place in a convergent plate boundary, where one plate with higher density (oceanic plate) sinks below the plate with lower density (continental plate). Earthquakes originating from such a process are called subduction earthquakes. There are two types of subduction earthquakes: 1. interface earthquakes are shallow events that occur at the interface between the two plates and 2. intraslab earthquakes are deep events that occur within the subducting plate. Figure 2.1 illustrates the subduction process occurring in Japan along with interface and intraslab events.

Subduction earthquakes are different from other tectonic earthquakes, essentially because of the tectonic processes involved. The largest earthquakes occur only in subduction zones as a result of the high compressive stresses and the large contact area between the plates. Pacheco and Sykes (1992) noted that around 90% of the total seismic moment released in the last century can be attributed to subduction earthquakes. Subduction zones lead to large strain build up due to interlocking of the plates over large areas which results in the potential for Megathrust earthquakes ($M_w > 8$). Because of the huge contact area between the subducting and over-riding plates, the resulting rupture process during an earthquake becomes complicated and distinct from other tectonic regimes (e.g., shallow-crustal events in active seismic regions). Rupture areas for subduction earthquakes are generally larger than those from other tectonic regimes. As a result of these differences in tectonic process, the resulting ground motions become distinct from those of shallow crustal earthquakes. The differences in the ground motions are illustrated in Figure 2.2 wherein the ground motions from 2010 M_w8.8 Maule, Chile earthquake (subduction event) is compared with the ground motion from 1994 M_w6.7 Northridge, California earthquake (shallow-crustal event).

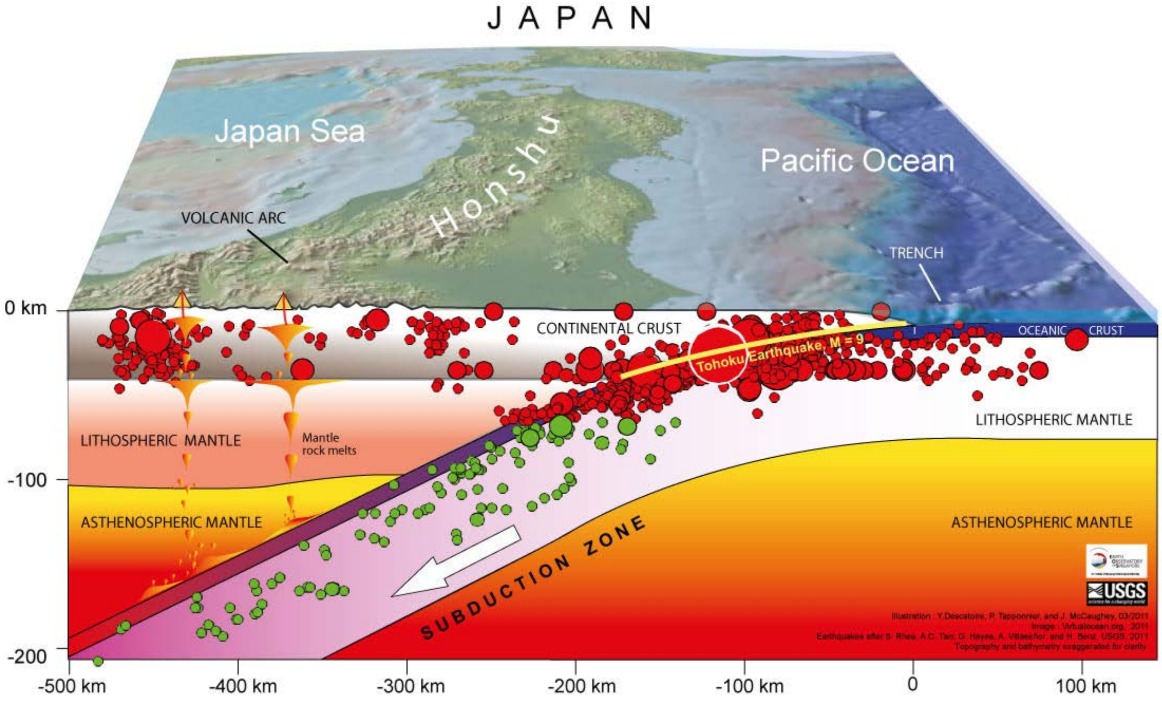

Fig 2.1 Illustration of the subduction zone in Japan. Interface earthquakes are indicated by red dots and Intraslab earthquakes are indicated by green dots. The size of the dots represents relative size of the earthquake (Image adopted from Earth Observatory 2011)

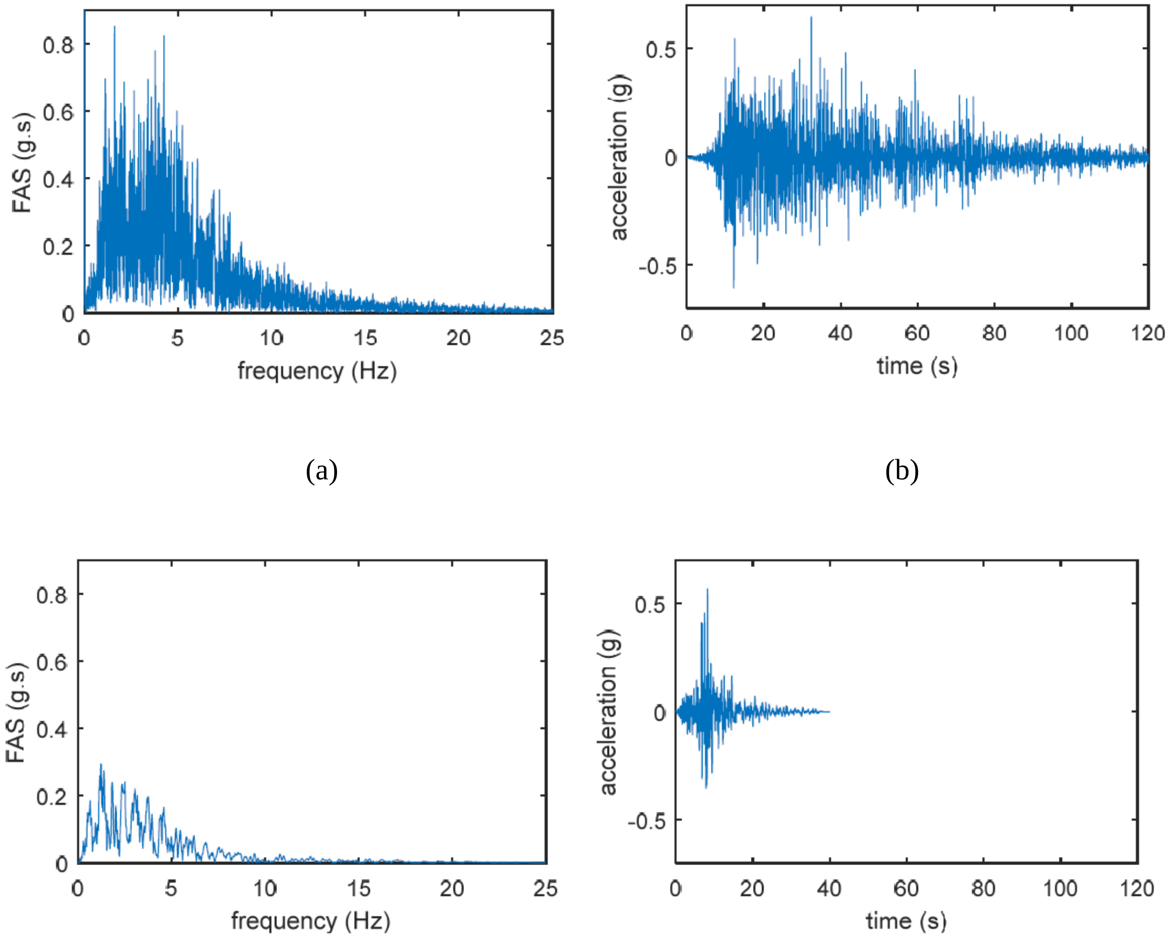

(a) (b)

(c) (d)

Fig 2.2 (a) Fourier Amplitude Spectrum (FAS) and (b) acceleration time history of the selected subduction ground motion record. (c) Fourier Amplitude Spectrum (FAS) and (d) acceleration time history of the selected shallow crustal ground motion record. The subduction motion is the San Pedro record from the Maule earthquake, and the shallow crustal record is the Castaic-Old Ridge Road record from the Northridge earthquake.

2.2 Evaluation of Liquefaction Triggering

Given the detrimental effects of liquefaction, it is important to evaluate sites with liquefaction potential. The stress-based approach, initially proposed by Whitman (1971) and then by Seed and Idriss (1971) is the most widely used procedure for evaluating liquefaction triggering. The "simplified" stress-based approach uses Newton's Second Law to estimate the shear stresses induced in the soil column (i.e., seismic demand) and uses empirical relationships derived from the analysis of field case histories to estimate the ability of the soil to resist liquefaction. The procedure does not require site response analysis to determine shear stresses and hence the adjective "simplified." The approach estimates factor of safety (FS) as the ratio of normalized Cyclic Resistance Ratio ($CRR_{7.5}$) to the normalized Cyclic Stress Ratio (CSR^*)

$$FS = \frac{CRR_{7.5}}{CSR^*} \tag{2.1}$$

The normalized Cyclic Stress Ratio represents the seismic demand that arises from the earthquake shaking whereas normalized Cyclic Resistance Ratio represents the limit state at which liquefaction occurs. CSR^* can be computed as

$$CSR^* = 0.65\ \frac{a_{max}}{g}\ \frac{\sigma_v}{\sigma'_{vo}}\ r_d\ \frac{1}{MSF\ \ K_\sigma\ K_\alpha} \tag{2.2}$$

where a_{max} is the Peak Ground Acceleration, g is the acceleration due to gravity in the same units as a_{max}, σ'_{vo} and σ_v are initial effective and total stresses, respectively. K_σ and K_α are factors to correct for overburden stress and initial static shear stress, respectively. The important empirical parameters used in the computation of CSR^* are the Magnitude Scaling Factor (MSF) and Stress-reduction factor (r_d). MSF is the factor that corrects for differences in the duration of the ground motion to the duration of the reference event (M_w7.5) in terms of number of equivalent cycles (n_{eq}). r_d is the factor to account for the non-rigid response of the soil column. By plotting CSR^* versus normalized Standard Penetration Test (SPT) blow count ($N_{1,60cs}$) and identifying liquefaction observations from non-liquefaction cases, a boundary separating both types of observations can be obtained. This boundary is essentially the $CRR_{7.5}$ curve representing the capacity of the soil to resist liquefaction. Over the years, various in-situ properties were correlated to $CRR_{7.5}$. These include $N_{1,60cs}$ (Idriss and Boulanger 2008), normalized Cone Penetration Test (CPT) tip resistance (q_{c1Ncs}) (Moss et al. 2006), and normalized small-strain shear wave velocity (V_{s1}) (Kayen et al. 2013). Considering the uncertainties in all the parameters involved in the approach and the $CRR_{7.5}$ curve, liquefaction evaluation can also be viewed from a probabilistic standpoint (Boulanger and Idriss 2012; Cetin et al. 2004).

The simplified procedure is semi-empirical because of the empirical parameters that are central to this procedure, especially MSF and r_d. Because the $CRR_{7.5}$ curve is derived from field case histories analyzed using the MSF and r_d relationships, the $CRR_{7.5}$ inherently includes any bias in the MSF and r_d relationships (Green et al. 2019). The empirical essence embedded in the procedure make predictions for scenarios not captured by range of the data used in its development questionable. To the introduction of uncertainty in predictions as a result of the inherent bias in the $CRR_{7.5}$ curve, the correlations for MSF and r_d should be consistent with $CRR_{7.5}$ curve. Green et al. (2019) outlines the “unbiased” procedure wherein site-specific MSF and r_d relationships are used in conjunction with $CRR_{7.5}$ curve developed using the similar approach used for developing MSF and r_d relationships. For example, employing MSF and r_d relationships developed using a certain approach, but using a $CRR_{7.5}$ curve obtained from MSF and r_d relationships developed using a different approach will lead to inaccurate results.

2.3 Magnitude Scaling Factor (MSF)

As described previously, MSF is the factor that accounts for duration of earthquake shaking. It is defined as the ratio of number of equivalent cycles for a reference $M_w7.5$ earthquake to the number of equivalent cycles for the event of interest with magnitude M raised to the power b. The value of b is generally obtained from laboratory data and is the slope of the plot between log(CSR) and log(N_{liq}) (number of cycles to initiate liquefaction).

$$MSF = \left\{\frac{n_{eq,M7.5}}{n_{eq}}\right\}^{b} \tag{2.3}$$

The number of equivalent cycles (n_{eq}) plays a major role in computing MSF. n_{eq} can be understood as the number of sinusoidal cycles with uniform amplitude needed to represent an irregular earthquake load. Fundamental to the computation of n_{eq} is the Palmgren-Miner (P-M) fatigue theory (Palmgren 1924; Miner 1945). The theory rests on the cumulative damage hypothesis that accounts for the progression of failure/damage from the initial loading cycle to the final. Detailed overview of P-M theory can be found in numerous studies (Collins 1981; Green and Terri 2005; Hancock and Bommer 2005). Nevertheless, a brief review is presented herein.

According to Miner (1945), the cumulative damage D can be expressed as:

$$D = \sum_{i} \frac{w_i}{W} = \sum_{i} \frac{n_i}{N_i} \tag{2.4}$$

where W is the total work absorbed at failure, w_i is the work absorbed after n_i cycles of uniform cyclic stress with amplitude S_i and N_i is the number of cycles of uniform cyclic stress of amplitude S_i needed to reach failure. In an irregular loading, as in many practical applications, there will be multiple distinct peaks in the stress history; thus, it is important to summate the damage caused due to each peak amplitude. Equation (2.4) essentially represents the cumulative damage caused by an erratic stress loading. With the same analogy, the cumulative damage caused by uniform stress load of n_{eq} cycles with amplitude S_{ref} can be expressed as

$$D = \frac{n_{eq}}{N_{ref}} \tag{2.5}$$

where N_{ref} is the number of cycles of amplitude S_{ref} at failure. The number of equivalent cycles, n_{eq}, can be easily determined by equating the expressions in (2.4) and (2.5).

$$n_{eq} = \sum_i N_{ref} \frac{n_i}{N_i} \tag{2.6}$$

Seed et al. (1975) adapted Equation (2.6) for application in liquefaction of soils. The number of equivalent cycles is computed as a weighted average of the number of peaks in the stress time history weighted by the laboratory-based normalized CSR-N_{liq} curve (also called as Weighing factor or WF curve). Figure 2.3 presents an example curve from Seed et al. (1975). The x-axis of the curve is essentially the term $\frac{N_{ref}}{N_i}$ in Equation (2.6). For reading values off the curve and obtaining n_i, peak-counting methods are used. Hancock and Bommer (2005) presents a detailed overview of various types of peak-counting methods available. The goal of the peak counting method is to obtain a histogram of peak amplitudes (analogous to n_i-normalized S_i plot) in the normalized time history (normalized by the maximum value). For each value of n_i, the corresponding value of $\frac{N_{ref}}{N_i}$ can be read off the curve for the corresponding value of normalized S_i.

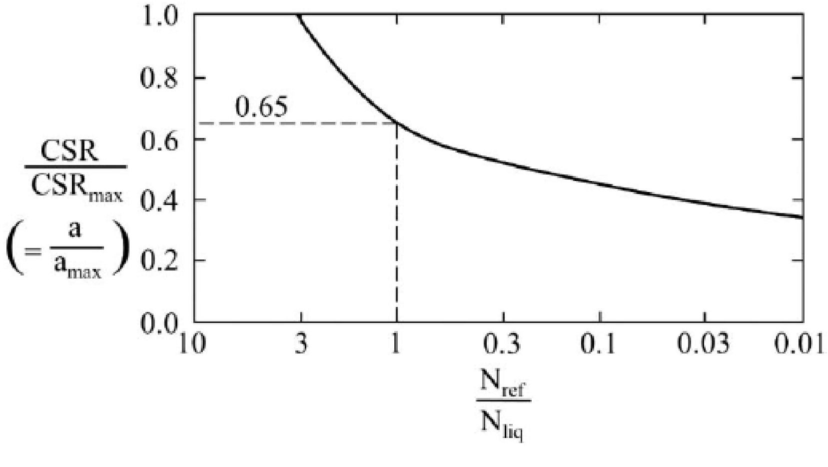

Fig 2.3 Weighing Factor curve used by Seed et al. (1975) to compute n_{eq}

There are a few shortcomings to the Seed et al. (1975) implementation of P-M theory to compute n_{eq}. While the practical shortcomings include proper selection of WF curve, proper selection of peak counting method, and accounting for multi-directional shaking, the major issue lies with the inherent assumption that damage accumulation is linear. This assumption does not hold in reality because the area under the hysteresis loop for a soil sample does not remain constant when it is subjected to uniform cyclic load. Overcoming this drawback, Green and Terri (2005) proposed an alternative implementation of P-M theory wherein n_{eq} is computed as the ratio of total dissipated energy due to the earthquake load ($\sum_i w_i$) to the dissipated energy (w_{ref}) from one reference cycle with amplitude τ_{ref} .

$$n_{eq} = \frac{\sum_i w_i}{w_{ref}} \tag{2.7}$$

w_{ref} can in turn be computed from the soil's equivalent viscous damping ratio using Equation (2.8).

$$w_{ref} = \frac{2\pi D_\gamma {\tau_{ref}}^2}{G_\gamma} \tag{2.8}$$

where G_γ and D_γ are the shear modulus and damping ratio at strain γ corresponding to the reference shear stress τ_{ref}. τ_{ref} is determined as 0.65 times the maximum shear stress induced due to earthquake shaking.

Several studies have been performed to develop correlations for n_{eq} (Liu et al. 2001; Cetin 2000; Biondi et al. 2004; Lasley et al. 2017). While most of the traditionally used correlations (Seed et al. 1975; Cetin 2000) are based on Seed et al.'s variant of P-M fatigue theory, more recent correlations (Lee 2009; Lasley et al. 2017; Green et al. 2020) are based on Green and Terri's variant of P-M fatigue theory. Because of the shortcomings of the Seed et al. variant, the correlations based on the Green and Terri approach are considered more appropriate. Over the years, the n_{eq} correlations improvised as a result of growing ground motion database and the strength of functional forms used for regression. Seed et al. (1975) used ~60 motions to develop the correlations, whereas Green et al. (2020) makes use of simulation techniques to obtain over 3800 motions for developing the correlations. However, the ground motion databases used to develop recent models originate from different tectonic regimes, and none from subduction zone earthquakes. Almost all the correlations were developed using the ground motions from active shallow-crustal tectonic regime. A few studies (Lasley et al. 2017; Lee 2009) developed correlations for stable continental regions. Green et al. (2020) focused on the Groningen region in the Netherlands which is affected by induced seismicity. Several functional forms have been employed over the years. Lasley et al. (2017) provides a comprehensive review on the functional forms used in various studies. The most common parameters used in correlations are moment magnitude (M_w), closest distance from the rupture plane to the site (R_{rup}) and peak horizontal ground acceleration (a_{max}) at the surface of the soil profile. Green et al. (2020) has used average small-strain shear-wave velocity in the top 12 m ($V_{s,12}$) to predict n_{eq}. Other ground motion parameters such as 5-95% significant duration, Arias Intensity, and site parameters such as fundamental site period have also been used in some studies (Castiglia and Magistris 2018; Di Filippo et al. 2013; Kishida and Tsai 2014).

2.4 Stress reduction factor (r_d)

The stress reduction factor (r_d) is defined as the ratio of shear stress induced in a flexible soil column at depth z to the shear stress induced at the base of a rigid soil column. Applying Newton's second law of motion, the shear stress at the base of a rigid soil column can be easily computed. However, shear stresses in a flexible soil column are generally obtained through site response analysis. Avoiding the need for performing site response analysis, r_d allows for the estimation of shear stresses at a given depth in a soil column from the shear stresses at the base of a rigid soil column. In a sense, r_d is the parameter that "*simplifies*" the liquefaction evaluation procedure. Figure 2.4 illustrates how r_d plays a significant role in the "simplified" liquefaction evaluation procedure.

CSR for induced at the base of a non-rigid soil column:

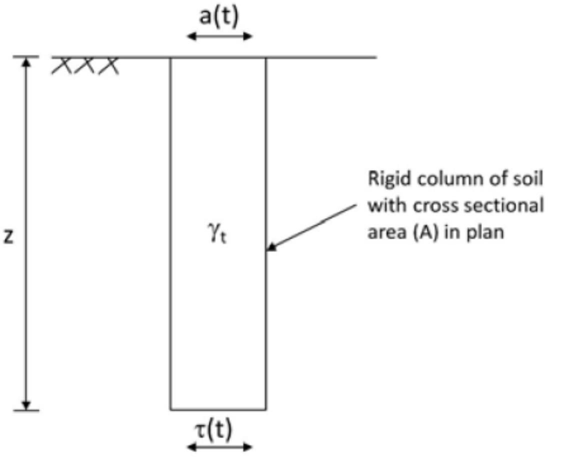

$$F(t) = m \cdot a(t)$$

$$= z \cdot A \cdot \frac{\gamma_t}{g} \cdot a(t)$$

$$\tau_{rigid}(t) = \frac{F(t)}{A} = \frac{a(t)}{g} \cdot \sigma_v$$

$$\tau_{rigid\ avg} = 0.65 \cdot \tau_{rigid\ max}$$

$$= 0.65 \cdot \frac{a_{max}}{g} \cdot \sigma_v$$

$$r_d = \frac{\tau_{non\text{-}rigid\ avg}}{\tau_{rigid\ avg}}$$

$$CSR = 0.65 \cdot \frac{a_{max}}{g} \cdot \frac{\sigma_v}{\sigma'_{vo}} \cdot r_d$$

F(t) = inertial force in rigid soil column induced by earthquake shaking
m = mass of soil column of having a cross-sectional area A and length z
a(t) = time dependent earthquake acceleration at the surface of the soil profile
γ_t = total unit weight of soil
g = coefficient of acceleration due to gravity
σ_v = total vertical stress at the base of the soil column
σ'_{vo} = effective vertical stress at the base of the soil column
a_{max} = peak ground acceleration at the surface of the soil profile
$\tau_{rigid}(t)$ = time dependent earthquake-induced shear stress at the base of a rigid soil column
$\tau_{rigid\ avg}$ = "average" earthquake-induced shear stress at the base of a rigid soil column
$\tau_{non\text{-}rigid\ avg}$ = "average" earthquake-induced shear stress at the base of a non-rigid soil column

Fig 2.4 Illustration of stress reduction factor (from Lasley et al. 2016)

Unlike the number of equivalent cycles, the computation of stress reduction factor is straight-forward and holds less ambiguity. The shear stresses induced in a flexible soil column at depth z is computed from numerical site response analysis and the shear stresses at the base of a rigid soil column can be computed from Newton's second law of motion as described in Figure 2.4. The r_d is then defined as the ratio of shear stress at the base of the rigid soil column to the shear stress at depth z in a flexible soil column.

Several correlations have been proposed for r_d over the years. Seed and Idriss (1971) proposed the first r_d correlation using site response data from limited number of ground motions and soil profiles. It was followed by the correlations by Liao and Whitman (1986) wherein r_d is a bilinear function of depth. Youd et al. (2001) liquefaction evaluation procedure uses the r_d relationship proposed by Liao and Whitman (1986). Idriss (1999) developed r_d correlations from performing several hundred site response analyses. He considers the effect of earthquake magnitude and depth of the soil layer in the functional form. The most widely used liquefaction evaluation procedures today (Idriss and Boulanger 2008; Boulanger and Idriss 2014) employ the relationship proposed by Idriss (1999). The correlation proposed by Cetin (2000) used a more comprehensive database and employed M_w, a_{max}, and $V_{s,12}$ as predictive parameters. Kishida et al. (2009) had employed fundamental site period (T_s), small-strain shear wave velocities (V_s), response spectral ratio for the surface ground motion (S_1) and a_{max} for developing the correlation. Other recent studies based on comprehensive databases and improved functional forms include Lasley et al. (2016) and Green et al. (2020). While most of the relationships were developed for active shallow-crustal tectonic regimes, Lasley et al. (2016) and Green et al. (2020) developed relationships for stable continental tectonic regimes and the Groningen region in the Netherlands affected by induced seismicity. There are no relationships currently available for subduction zones.

References

Berrill, J.B. and Davis, R.O., 1982. Energy dissipation and seismic liquefaction in sands. Earthquake Engineering and Structural Dynamics, 10(1), pp.59-68.

Biondi, G., Cascone, E. and Maugeri, M., 2004. Number of uniform stress cycles equivalent to seismic loading. Proceedings of 11th ICSDEE & 3rd ICEGE. Berkeley, CA, USA, 2, pp.705-712.

Boulanger, R.W. and Idriss, I.M., 2012. Probabilistic standard penetration test–based liquefaction–triggering procedure. Journal of Geotechnical and Geoenvironmental Engineering, 138(10), pp.1185-1195.

Boulanger, R.W. and Idriss, I.M., 2014. CPT and SPT based liquefaction triggering procedures. Report No. UCD/CGM.-14/01, Center for Geotechnical Modeling, Department of Civil and Environmental Engineering, University of California at Davis, 134 pp.

Castiglia, M. and de Magistris, F.S., 2018. Prediction of the number of equivalent cycles for earthquake motion. Bulletin of Earthquake Engineering, 16(9), pp.3571-3603.

Çetin, K.Ö., 2000. Reliability-based assessment of seismic soil liquefaction initiation hazard. PhD dissertation. University of California, Berkeley.

Cetin, K.O., Seed, R.B., Der Kiureghian, A., Tokimatsu, K., Harder Jr, L.F., Kayen, R.E. and Moss, R.E., 2004. Standard penetration test-based probabilistic and deterministic assessment of seismic soil liquefaction potential. Journal of Geotechnical and Geoenvironmental Engineering, 130(12), pp.1314-1340.

Collins, J. A., 1981. Failure of materials in mechanical design: Analysis, prediction, prevention, Wiley, New York.

Di Filippo, G., Biondi, G. and Cascone, E., 2013. Nuovi modelli previsionali per la valutazione del numero di cicli di carico equivalente. Incontro Annuale dei Ricercatori di Geotecnica. 2013- IARG 2013 Perugia

Earth Observatory., 2011. The great East Japan (Tohoku) 2011 earthquake: Important lessons from old dirt. https://www.earthobservatory.sg/news/great-east-japan-tohoku-2011-earthquake-important-lessons-old-dirt. Last accessed on August 6th, 2021

Green, R.A. and Terri, G.A., 2005. Number of equivalent cycles concept for liquefaction evaluations—Revisited. Journal of Geotechnical and Geoenvironmental Engineering, 131(4), pp.477-488.

Green, R.A., Bommer, J.J., Rodriguez-Marek, A., Maurer, B.W., Stafford, P.J., Edwards, B., Kruiver, P.P., De Lange, G. and Van Elk, J., 2019. Addressing limitations in existing 'simplified'liquefaction triggering evaluation procedures: application to induced seismicity in the Groningen gas field. Bulletin of Earthquake Engineering, 17(8), pp.4539-4557.

Green, R.A., Bommer, J.J., Stafford, P.J., Maurer, B.W., Kruiver, P.P., Edwards, B., Rodriguez-Marek, A., de Lange, G., Oates, S.J., Storck, T. and Omidi, P., 2020. Liquefaction Hazard in the Groningen Region of the Netherlands due to Induced Seismicity. Journal of Geotechnical and Geoenvironmental Engineering, 146(8), p.04020068.

Hancock, J. and Bommer, J.J., 2005. The effective number of cycles of earthquake ground motion. Earthquake Engineering and Structural Dynamics, 34(6), pp.637-664.

Idriss, I. M., 1999. An update to the Seed-Idriss simplified procedure for evaluating liquefaction potential. Proceedings from TRB Workshop on New Approaches to Liquefaction Analysis, U.S. Department of Transportation, Federal Highway Administration, Washington, DC.

Idriss, I.M. and Boulanger, R.W., 2008. Soil liquefaction during earthquakes. Monograph MNO-12, Earthquake Engineering Research Institute, Oakland, CA.

Kayen, R., Moss, R.E.S., Thompson, E.M., Seed, R.B., Cetin, K.O., Kiureghian, A.D., Tanaka, Y. and Tokimatsu, K., 2013. Shear-wave velocity–based probabilistic and deterministic assessment of seismic soil liquefaction potential. Journal of Geotechnical and Geoenvironmental Engineering, 139(3), pp.407-419.

Kishida, T. and Tsai, C.C., 2014. Seismic demand of the liquefaction potential with equivalent number of cycles for probabilistic seismic hazard analysis. Journal of Geotechnical and Geoenvironmental Engineering, 140(3), p.04013023.

Kishida, T., Boulanger, R.W., Abrahamson, N.A., Driller, M.W. and Wehling, T.M., 2009. Seismic response of levees in the Sacramento-San Joaquin Delta. Earthquake spectra, 25(3), pp.557-582.

Lasley, S.J., Green, R.A. and Rodriguez-Marek, A., 2016. New stress reduction coefficient relationship for liquefaction triggering analyses. Journal of Geotechnical and Geoenvironmental Engineering, 142(11), p.06016013.

Lasley, S.J., Green, R.A. and Rodriguez-Marek, A., 2017. Number of equivalent stress cycles for liquefaction evaluations in active tectonic and stable continental regimes. Journal of Geotechnical and Geoenvironmental Engineering, 143(4), p.04016116.

Lee, J., 2009. Engineering characterization of earthquake ground motions. Ph.D. dissertation, University of Michigan, Ann Arbor.

Liao, S. S. C., and Whitman, R. V., 1986. Catalogue of liquefaction and non-liquefaction occurrences during earthquakes. Department of Civil Engineering, Massachusetts Institute of Technology, Cambridge.

Liu, A.H., Stewart, J.P., Abrahamson, N.A. and Moriwaki, Y., 2001. Equivalent number of uniform stress cycles for soil liquefaction analysis. Journal of Geotechnical and Geoenvironmental Engineering, 127(12), pp.1017-1026.

Miner, M.A., 1945. Cumulative Damage in Fatigue. Transactions, ASME, 67, A159-A164.

Moss, R.E., Seed, R.B., Kayen, R.E., Stewart, J.P., Der Kiureghian, A. and Cetin, K.O., 2006. CPT-based probabilistic and deterministic assessment of in situ seismic soil liquefaction potential. Journal of Geotechnical and Geoenvironmental Engineering, 132(8), pp.1032-1051.

Pacheco, J.F. and Sykes, L.R., 1992. Seismic moment catalog of large shallow earthquakes, 1900 to 1989. Bulletin of the Seismological Society of America, 82(3), pp.1306-1349.

Palmgren, A., 1924. Die Lebensdauer Von Kugella Geru, ZVDI, 68, 339-341.

Seed, H.B. and Idriss, I.M., 1971. Simplified procedure for evaluating soil liquefaction potential. Journal of the Soil Mechanics and Foundations division, 97(9), pp.1249-1273.

Seed, H.B., Idriss, I.M., Makdisi, F., Banerjee, N., 1975. Representation of Irregular Stress Time Histories by Equivalent Uniform Stress Series in Liquefaction Analysis, Report No. EERC 75-29, Earthquake Engineering Research Center, College of Engineering, University of California, Berkeley.

Whitman, R.V., 1971. Resistance of soil to liquefaction and settlement. Soils and Foundations, 11(4), pp.59-68.

Youd, T.L., Idriss, I.M., Andrus, R.D., Arango, I., Castro, G., Christian, J.T., Dobry, R., Finn, W.D.L., Harder, L.F., Hynes, M.E., Ishihara, K., Koester, J.P., Liao, S.S.C, Marcuson, III, W.F., Martin, G.R., Mitchell, J.K., Moriwaki, Y., Power, M.S., Robertson, P.K., Seed, R.B., and Stokoe, II, K.H., 2001. Liquefaction Resistance of Soils: Summary Report from the 1996 NCEER and 1998 NCEER/NSF Workshops on Evaluation of Liquefaction Resistance of Soils. Journal of Geotechnical and Geoenvironmental Engineering, 127, pp.297-313.

Chapter 3

Liquefaction triggering model for subduction zone earthquakes

3.1 Abstract

Earthquake-induced liquefaction poses a significant threat to infrastructure around the world. The most commonly used procedure for evaluating liquefaction triggering is the stress-based, semi-empirical “simplified” procedure. Though the existing variants of the simplified procedure yield good results for scenarios that are representative of those used in the derivation of the procedure, they are less accurate in evaluating liquefaction triggering for megathrust earthquakes in subduction zones. The shortcomings of the existing variants originate from the empirical parts of the procedure which are derived from data from active shallow-crustal tectonic regimes. The differences in the characteristics of tectonic regimes render the predictions from existing variants questionable in subduction zones. Therefore, this study aims to develop empirical relationships for liquefaction triggering models to be used in subduction zones. Relationships are developed for number of equivalent cycles (n_{eq}) and stress reduction factor (r_d) based on site response data obtained from representative ground motions and geologic profiles. Additionally, separate models are presented for interface and intraslab events which allows for better quantification of uncertainty. It has been noted that the models predict higher n_{eq} than other published models; partly due to the differences in the characteristics of ground motions and partly due to the site characteristics. The model for r_d predicts lower values than other models at shallow depths but predicts higher values as the depth increases. In comparison to other published models, the models proposed herein are tailored specifically for use in subduction zones and, therefore, result in less bias and uncertainty.

Keywords: Liquefaction triggering, number of equivalent cycles, stress reduction factor, subduction zone

3.2 Introduction

Seismically induced liquefaction and its related effects are some of the major causes for infrastructure damage due to earthquakes. To assess the liquefaction hazard, the most commonly used approach in practice is the stress-based "simplified" procedure originally introduced by Whitman (1971) and Seed and Idriss (1971). The "simplified" approach is semi-empirical, meaning that some parts of the analysis are empirical and based on observations over a number of events. Over the years, the empirical parts in the analysis have paved way for a number of variants of the procedure (Cetin et al. 2004; Idriss and Boulanger 2008; Boulanger and Idriss 2014; Kayen et al. 2013; Green et al. 2019, 2020). One of the empirical parts in the analysis is the normalized Cyclic Resistance Ratio ($CRR_{7.5}$) curve which is used to estimate the capacity or resistance of the soil to liquefaction triggering. $CRR_{7.5}$ is commonly correlated to Standard Penetration Test (SPT) normalized blow count ($N_{1,60cs}$), Cone Penetration Test (CPT) normalized tip resistance (q_{c1Ncs}), or normalized small-strain shear wave velocity (V_{s1}) measurements from the site. The other empirical part in the simplified model relates to the seismic load in the form of the normalized Cyclic Stress Ratio (CSR^*). The general formulation for CSR^* is as follows:

$$CSR^* = 0.65\,\frac{a_{max}}{g}\,\frac{\sigma_v}{\sigma'_{vo}}\,r_d\,\frac{1}{MSF}\frac{1}{K_\sigma K_\alpha} \tag{3.1}$$

where a_{max} is the peak ground acceleration at the profile surface, $\sigma'_{vo}$and σ_v are the initial effective and total stresses, respectively, g is the gravitational acceleration in the same units as a_{max}, and K_σ and K_α are the factors to correct for overburden stress and initial static shear stress, respectively. Two important empirical parameters used in the computation of CSR^* are the Magnitude Scaling Factor (MSF) and stress-reduction factor (r_d). MSF is the factor that corrects for the ground motion duration to the reference event (M7.5) in terms of number of equivalent cycles (n_{eq}) and r_d is the factor accounting for the non-rigid response of the soil column.

While the variants of the simplified procedure work good for seismic scenarios representative of those used to develop the $CRR_{7.5}$ curves, they are less accurate in predicting liquefaction triggering for megathrust earthquakes. Montalva and Ruz (2017) illustrated how the existing variants of the simplified procedure mispredicted liquefaction case histories due to M_w8.3 Illapel (2015) and M_w8.8 Maule (2010) earthquakes in Chile. Also, Alberto-Hernandez and Towhata (2017) argued that back analyses performed on liquefaction case histories in Japan, Chile, and New Zealand reveal discrepancies between predictions and actual observations. It is speculated that the reason for the mispredictions is the difference in tectonic regimes that would be reflected in the empirical parts of the approach, especially MSF and r_d. The existing variants of the simplified procedure uses the MSF and r_d relationships developed based on the data from active shallow-crustal tectonic regimes (e.g., California). This makes the use of these relationships questionable in other tectonic regimes (e.g., Chile). Lasley et al. (2016) and Green et al. (2019, 2020) also highlighted the importance of tectonic regimes in developing liquefaction triggering models.

Several relationships for n_{eq} have been developed (Lasley et al. 2016, 2017; Lee 2009; Cetin 2000; Biondi et al. 2004; Green et al. 2020). The differences between studies involve improved functional forms, size of database, tectonic setting and the computation of n_{eq}. n_{eq} can be computed either by using the Seed et al. (1975) implementation of Palmgren-Miner (P-M) fatigue theory (Stafford and Bommer 2009; Biondi et al. 2004) or the Green and Terri (2005) implementation of P-M fatigue theory (Lasley et al. 2017; Green et al. 2020). While there are correlations available for stable continental and active shallow-crustal tectonic regimes, no correlations are available for subduction zones. Also, in the existing relationships, the accounting of multidirectional shaking has been handled using various approaches. On the other hand, studies on r_d are comparatively straight-forward and involve less ambiguity. Important correlations for r_d that are widely used include Idriss (1999) and Cetin et al. (2004).

The objective of this study is to establish empirical relationships for number of equivalent cycles and stress-reduction factor that can be reliably used to predict liquefaction triggering in subduction zones when used along with an unbiased liquefaction triggering curve (i.e., Green et al. 2019). The primary motivation for this study is to ensure the applicability of the simplified approach for megathrust earthquakes in subduction zones. The empirical relations developed herein are based on representative soil profiles and subduction ground motions. Site response analyses are performed using 77 well-characterized representative geologic profiles and 254 pairs of ground motion records from subduction zone events. Darendeli and Stokoe (2001) modulus reduction and damping curves are used to model the non-linearity in the equivalent linear approach. Based on the site response data, mixed effects regression, considering the soil profiles and earthquake events as random effects, has been performed to develop the proposed models for number of equivalent cycles (n_{eq}) and stress reduction factor (r_d).

In the following sections, a brief overview of the ground motions and soil profiles used in this study are presented. The effect of predominant site period on the number of equivalent cycles is briefly discussed. Next, the models developed for n_{eq} and r_d are discussed in detail. Finally, the models developed in the study are compared with other published models.

3.3 Ground motions

The ground motion records used in the study are a subset of subduction zone motions recorded around the globe. The data are obtained from four ground motion databases: NGA Subduction project (Bozorgnia and Stewart 2020), KiK-net database processed by Bahrampouri et al. (2021a), Chilean ground motion database from Datacenterhub (Montalva and Bastias 2017) and Siber-Risk (Siber-Risk 2020). Since the records are intended to be used as input motions in site response analyses, only recordings at rock were selected. To this effect, the time-averaged small-strain shear wave velocity of the upper 30 m of the profile ($V_{s,30}$) of all the recording sites from which records were selected are greater than 650 m/s. Since the study is focused mainly on megathrust earthquakes in subduction zone regimes with significance to existing liquefaction case histories, only events with moment magnitudes greater than 5.5 are considered in the study (e.g., Green and Bommer 2019). In total, 254 pairs of horizontal ground motion records from 65 subduction events are obtained. The size of the compiled database is dominated by 46 interface events compared to 19 intraslab events. The moment magnitude range of the compiled database is 5.6 - 9.12 and the rupture distance (R_{rup}), measured as the closest distance of the site from the surface of the fault rupture, ranges from 20km – 205 km. Other event and station metadata are also obtained from the databases. Figure 3.1 shows the distribution of the magnitude versus source-to-site distance (R_{rup}) for the interface and intraslab events.

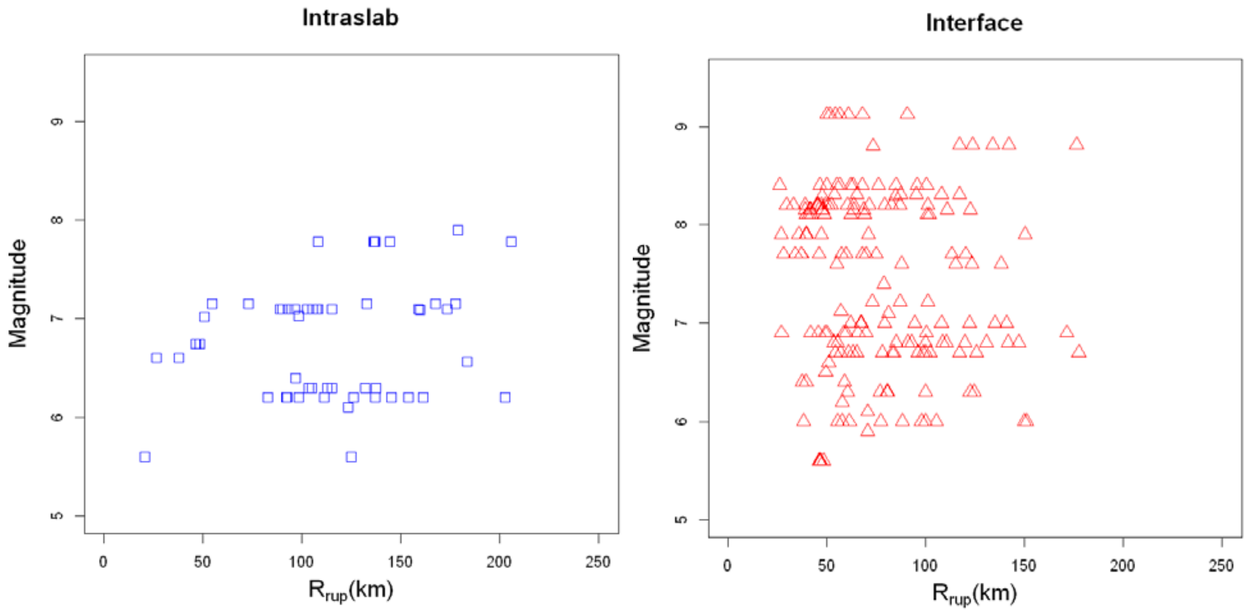

(a) (b)

Fig 3.1 Magnitude versus rupture distance distribution for (a) Intraslab and (b) Interface ground motion records. Each point in the plot represents a pair of horizontal ground motions.

3.4 Geologic profiles

The soil profiles used in the present study are obtained from various sources covering major subduction regions across the world. All these sites were characterized either as a part of post-earthquake investigation after subduction earthquakes or as an effort to classify seismic stations that record subduction ground motions, though all the sites did not necessarily experience surface manifestation of liquefaction. However, the depths of exploration have been limited in most of the studies. For example, an effort to characterize shear wave velocity profiles for recording stations in Seattle, Washington (Wong et al. 2011) only explored depths down to 30 m – 50 m. Similar to Wong et al. (2011), other studies also mainly focused on characterizing $V_{s,30}$ for use in ground motion models. The limited depth of site characterization affected how profiles are modeled in the site response analysis. Therefore, only those profiles that were characterized down to bedrock have been considered in this study. In total, 27 soil profiles were compiled. Other missing soil properties such as unit weights, plasticity index, and over consolidation ratio (OCR) are assumed based on soil description and shear wave velocities of the layers. In some cases, the shear wave velocity of the bed rock was increased (to a maximum of 900 m/s) to get higher impedance contrast.

The profiles from Chile and Peru are obtained from Rodriguez-Marek et al. (2010). According to Rodriguez-Marek et al. (2010), the soils presented in their study are typical of those found in Southern Peru and Northern Chile, composed mainly of sandy gravels with significant proportion of boulders. The recently formed river beds contain loose sands and include fine-grained soils. This depositional environment with dense sands and gravels are formed due to the sharp topographic relief between the Andes Mountains and the Pacific Ocean. The soil profiles used in this study also consist of dense sands and gravels, match the description and thus, can be claimed as representative profiles of the region.

The soil profiles in Washington state are obtained from the Seattle region. According to Troost and Booth (2008), the depth to bedrock in Seattle region varies from 0 to ~550 m. The bedrock in the Seattle region dips approximately 20 degrees towards the south. Therefore, northern Seattle has shallow bedrock while the southern parts have deeper sediments. Wong et al. (2011) also describe most deposits as glacial till. This matches the description found in the USGS report (Yount and Gower 1991) and Troost and Booth (2008). Based on this observation, the profiles used in the present study with depth to bedrock ~40 to 50 m can be considered representative of the region.

The soil profiles from Japan are obtained from Next Generation Liquefaction (NGL) database (Zimmaro et al. 2019) and the GEER report of the 2016 Kumamoto Earthquake (Kayen et al. 2017).

To check the sufficiency of the profiles for this study, the characteristics of the soil profiles are compared with those compiled by Cetin (2000). The database compiled by Cetin (2000) consists of 50 well-characterized profiles from post-earthquake investigations exclusively in California. Figure 3.2 presents the shear wave velocity profiles for both databases. Some stark differences can be observed. It is noted that the Cetin (2000) profiles are characterized to larger depths compared to the profiles in the present study. The shear wave velocities in the soil layers also tend to be different. Figure 3.3a illustrates these differences as a distribution of depth to bedrock versus $V_{s,30}$. Cetin's profiles are deep and soft in general whereas the profiles in the present study are comparatively shallow and stiff. This major difference between the databases can be parameterized using predominant site period (T_s) which captures both depth to bedrock and layer velocities. Figure 3.3b shows the clear contrast in T_s between the databases under consideration.

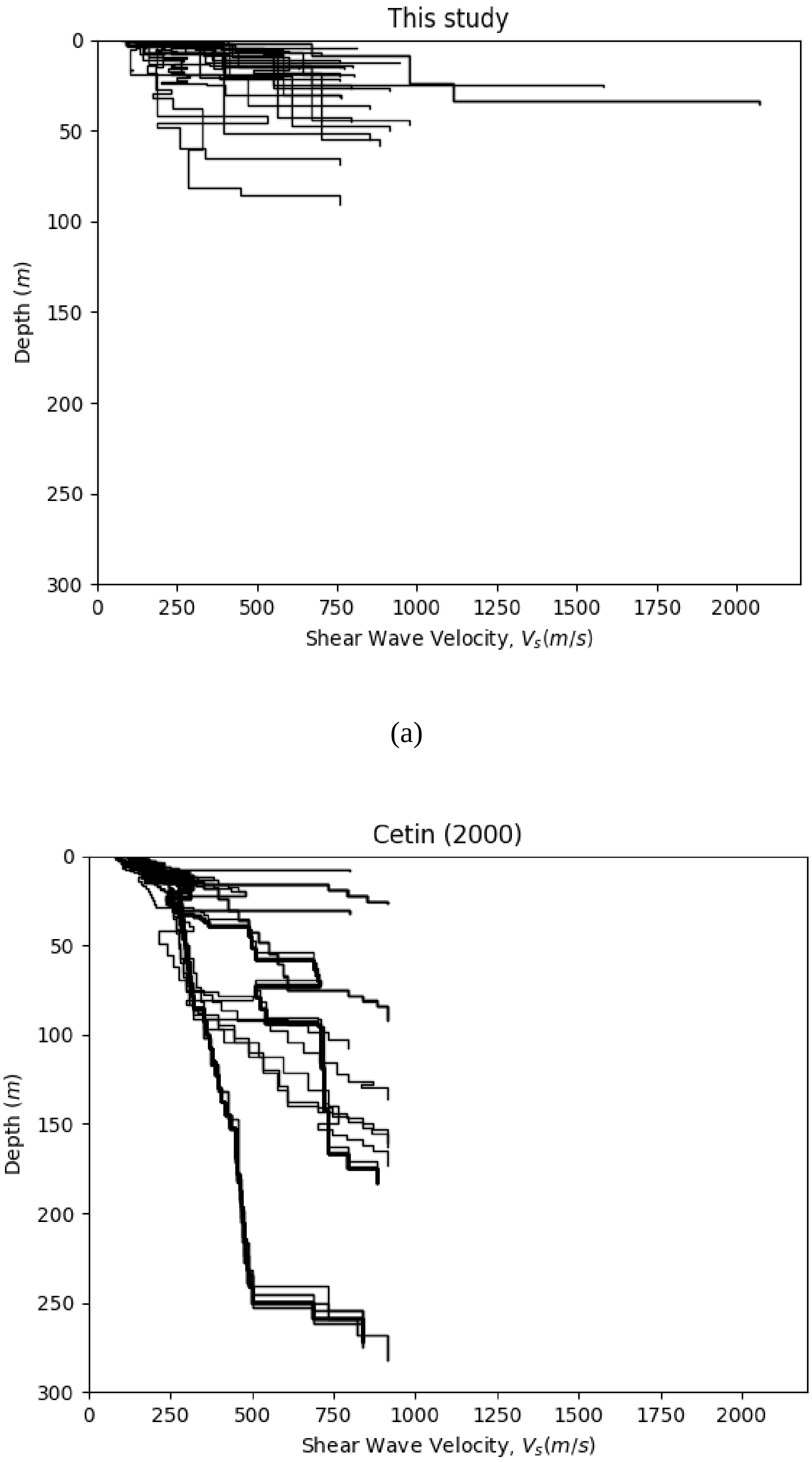

(a)

(b)

Fig 3.2 Shear wave velocity profiles (a) Database used in the present study (b) Cetin’s database

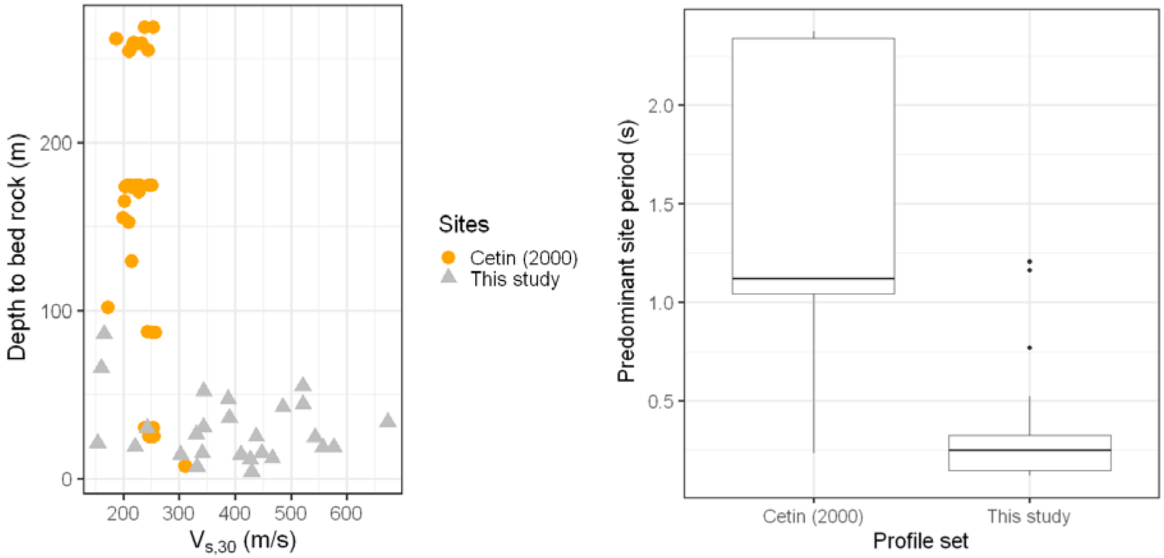

(a) (b)

Fig 3.3 Differences between the databases: (a) Depth to bedrock plotted against $V_{s,30}$ for the soil profiles used in the present study and Cetin (2000); and (b) Box-and-whisker plot showing the contrast in the predominant site period (T_s). The boxes represent the interquartile range (25th to 75th percentile) of the dataset. The horizontal line inside the box represents the median. The lines pointing outward from the boxes represent variability in the data outside the interquartile range. Finally, the dots represent outliers in the dataset.

Given this contrast in site period, the impact of this difference on n_{eq} and r_d must be checked in order to avoid any bias resulting from differences in site period. Therefore, site response analyses were performed on both profile sets using the compiled subduction ground motions. n_{eq} and r_d are computed for both the databases and compared. n_{eq} values between the databases are observed to be significantly different from each other, whereas the r_d values remain almost the same. Given the striking contrast in site period between the two databases, n_{eq} values are plotted against magnitude for varying site periods in Figure 3.4. The red line indicates a Locally Estimated Scatterplot Smoothing (LOESS) fit to all the datapoints corresponding to T_s > 1 s which essentially represents the profiles compiled by Cetin (2000). The green line indicates a LOESS fit to all the datapoints corresponding to T_s< 1s (representing the profiles compiled in the present study). It can be clearly seen that the n_{eq} increases as site period decreases. This observation presses the need to use a wider range of site periods if any potential bias with site period were to be avoided. Therefore, the 27 profiles compiled as part of this study are determined to be insufficient. Based on the assumption that the Cetin (2000) profiles reflect profiles that could be potentially impacted by subduction zone events, the profiles from Cetin's database are also included in our study. Therefore, in total 77 soil profiles are used in the final site response analyses and subsequent model development.

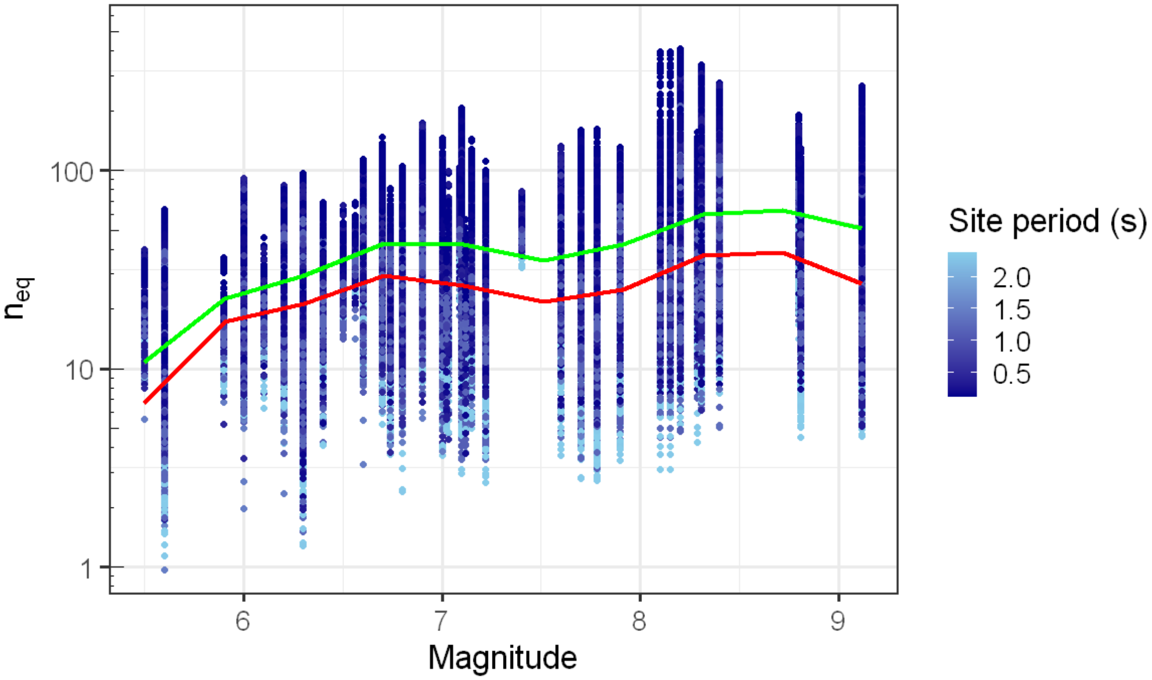

Fig 3.4 n_{eq} plotted against earthquake magnitude for different site periods indicated by the color bar. The red line indicates a LOESS fit to all the datapoints corresponding to T_s > 1 s. The green line indicates a LOESS fit to all the datapoints corresponding to T_s< 1s. The data shown here correspond to the depth range 3 – 10 m.

3.5 Site response analysis

Site response analyses are performed using the equivalent linear 1-D site response program ShakeVT2 (Thum et al. 2019). Darendeli and Stokoe (2001) modulus reduction and damping curves are used to model the soil non-linearity. In total, 19,712 site response analyses have been performed that yielded n_{eq} and r_d values for each liquefiable stratum. n_{eq} is computed using the implementation P-M fatigue theory as proposed by Green and Terri (2005). Multidirectional shaking is accommodated by adding the dissipated energy from each horizontal component of ground motion and setting the amplitude of equivalent cycles to 0.65 times the geometric mean of maximum shear stress in a given layer. For r_d, geometric mean of r_d from the two horizontal components is used. The analyses that resulted in an a_{max} greater than 1 g were ignored. The reason for this is the large strain component (greater than 1%) that makes the results questionable because the non-linearity in those cases is not appropriately captured by the equivalent linear approach. Moreover, cases when the a_{max} is greater than 1 g are likely not to be borderline cases for liquefaction evaluation, thus refinement of the n_{eq} or r_d models are not critical. Since no liquefaction cases have been observed deeper than 20 m (Cetin 2000), the depth range for model development is restricted to top 20 m. Finally, over 200,000 data points were generated and used in the regression models.

3.6 Model Development

The overall models for n_{eq} and r_d are developed through mixed effects regression implemented using the R package *lmer* (Bates et al. 2015). Earthquake events and soil profiles are regarded as random effects in the regression. To avoid any potential bias due to comparatively larger number of interface events in the ground motion database, an additional flag term that identifies an event as interface or intraslab has been added in the regression as a nested random effect along with the events. In addition to the overall models, regressions are performed separately for interface and intraslab events. The reason for this is twofold. First, it was observed that magnitude scaling is different for interface and intraslab events. Second, this reduces aleatory variability leading to better quantification of uncertainties. The functional forms for the regressions are chosen based on residual analysis and the trends observed in event and site terms.

Regression coefficients and standard deviations for event, site, and residual terms are obtained for the overall, Interface and Intraslab models – for both n_{eq} and r_d. The standard errors of the regression coefficients are obtained through a bootstrapping technique (Efron and Tibshirani 1994). The implementation of the bootstrapping procedure is as follows:

(i) From the entire set of data, 10,000 data points are randomly selected.

(ii) Mixed effects regression is carried out using the selected 10,000 data points and the regression coefficients are obtained. The obtained coefficients are recorded.

(iii) Steps (i) and (ii) are repeated for 1,000 iterations and regression coefficients are obtained.

(iv) At the end of Step (iii), the mean and standard deviation for each coefficient obtained from 1,000 iterations are computed and recorded.

3.6.1 Number of equivalent cycles

The model for the number of equivalent cycles is based on the functional form used by Lasley et al. (2017). The functional form is given in Equation (3.2):

$$\ln\left(n_{eq}\right) = a_1 + a_2\, M + a_3 \ln(a_{max}) + a_4 \ln(V_{s,30}) + \delta_{site} + \delta_{type} + \delta_{event} + \delta_{res} \tag{3.2}$$

where $a_1, a_2, a_3,$ and a_4 are regression coefficients; δ_{site}, δ_{event}, δ_{type}, and δ_{res} are profile (or site), event (nested with the type of event; interface or intraslab), type (interface or intraslab), and residual terms, respectively, with zero mean and standard deviations of τ_{site}, τ_{event}, τ_{type}, and σ_{res}, respectively.

It has been observed that the magnitude and $V_{s,30}$ terms (i.e., a_2 and a_4, respectively) are correlated with the intercept term (i.e., a_1) in the functional form. It has also been noted that the $V_{s,30}$ strongly influences the intercept such that the magnitude slope (i.e., a_2) could not be constrained through regression. This introduced trends in the event terms (δ_{event}) when plotted against magnitude. Therefore, the magnitude slope, a_2, has been fixed manually through grid search such that the event terms do not show any remaining trends. Figure 3.5 shows the event and site terms plotted against Magnitude and $V_{s,30}$, respectively.

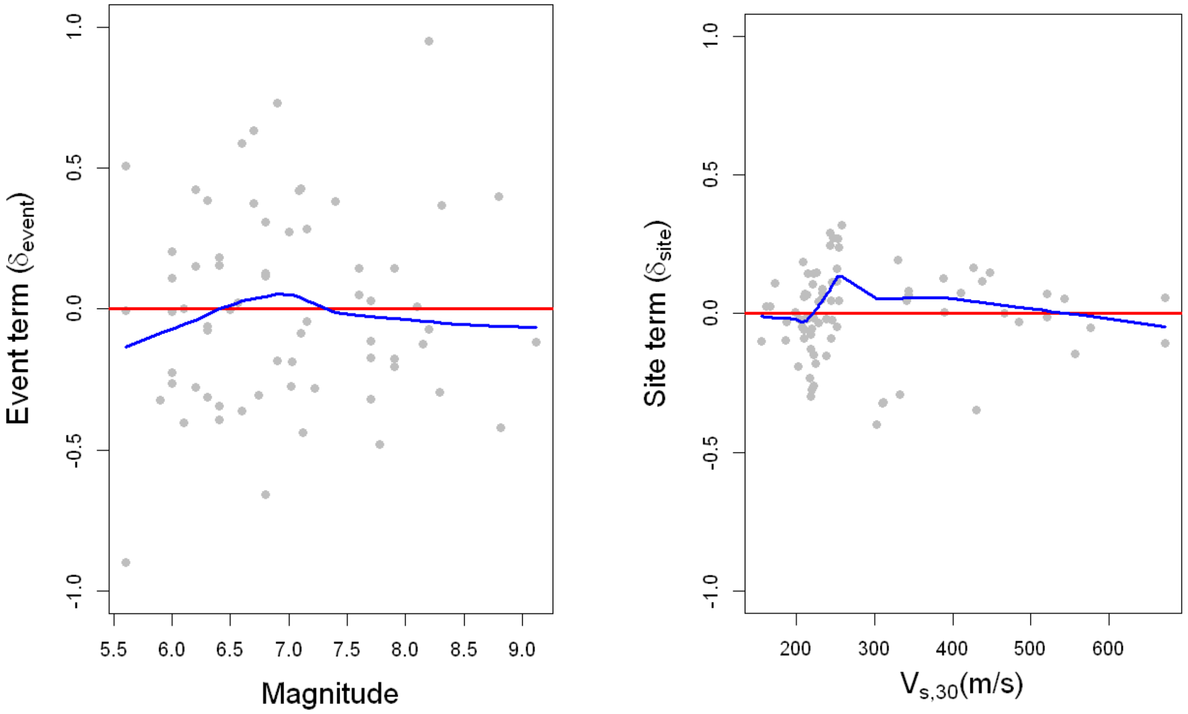

(a) (b)

Fig 3.5 (a) Event term plotted against Magnitude, and (b) Site term plotted against $V_{s,30}$. Blue lines indicate LOESS fit to the datapoints

Figure 3.6 shows the total residual plots. No trends can be observed in the plots against magnitude, $V_{s,30}$, or predominant site period, but there is a slight upward deviation from the zero line at higher a_{max} values. A small upward trend at very shallow depths can also be observed. However, these average mispredictions are well below one standard deviation of the model (0.6 log units). Therefore, the performance of the model is judged to be appropriate. The residual plot against site period shown in Figure 6e do not show any trends; therefore, there is no need to add site period as a predictor variable in the model.

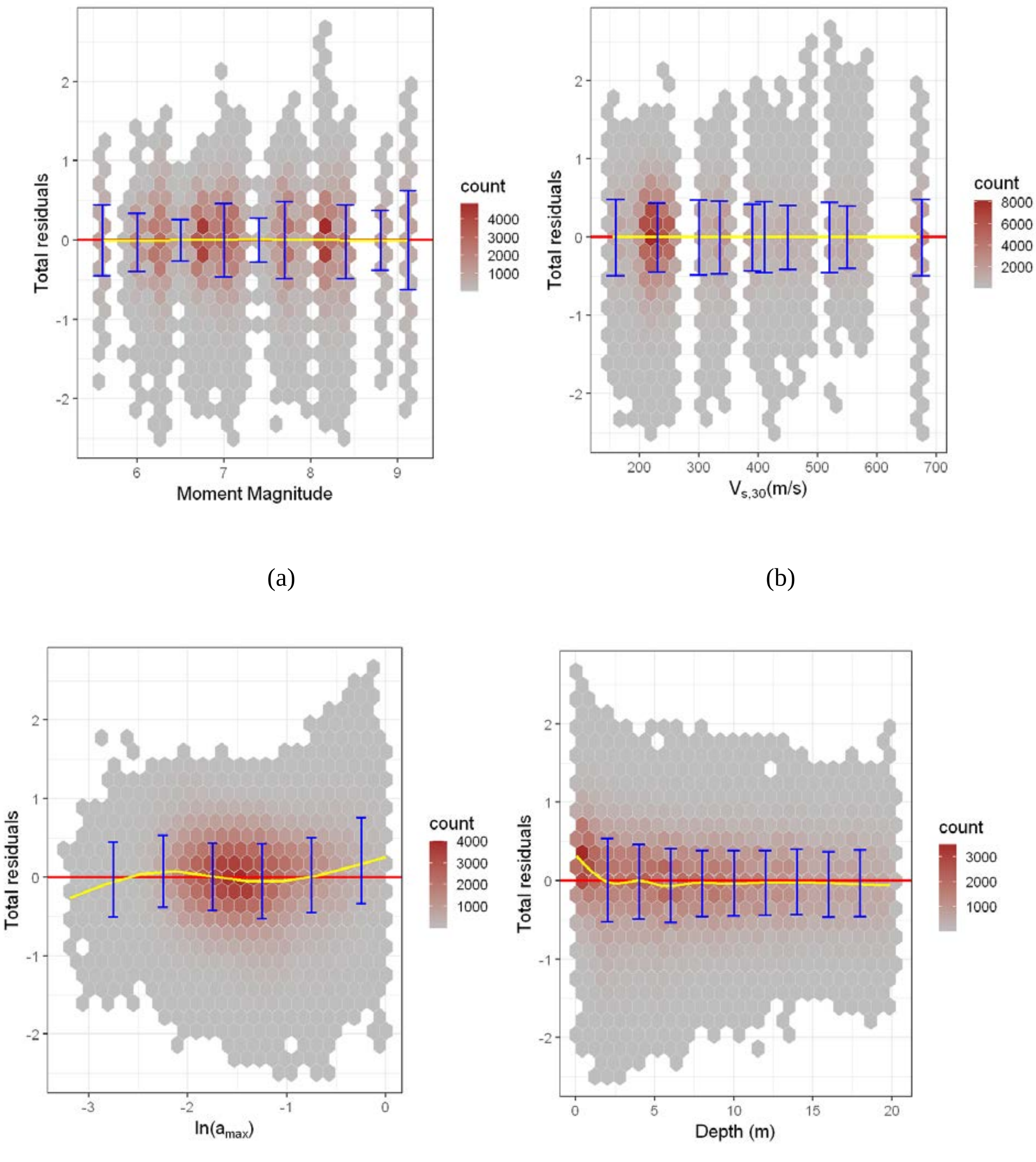
Total residuals
Moment Magnitude
count
4000
3000
2000
1000
Total residuals
$V_{s,30}$(m/s)
count
8000
6000
4000
2000
Total residuals
$\ln(a_{max})$
count
4000
3000
2000
1000
Total residuals
Depth (m)
count
3000
2000
1000

(a) (b)

(c) (d)

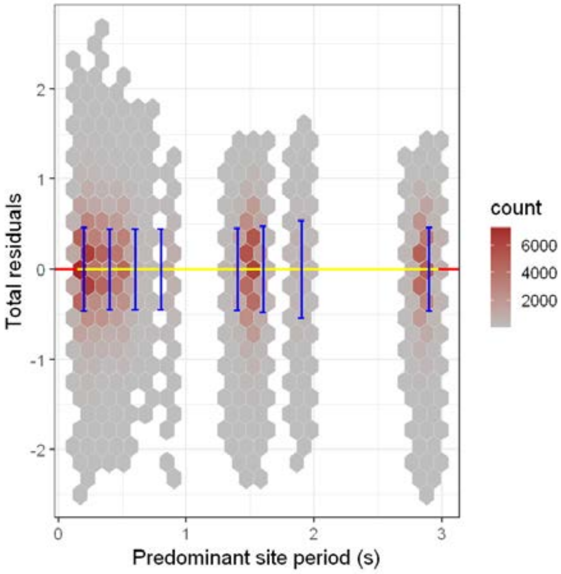

(e)

Fig 3.6 Total residuals of the overall model plotted against: (a) moment magnitude, (b) $V_{s,30}$, (c) a_{max}, (d) depth, and (e) predominant site period. Red lines indicate the zero line; yellow lines indicate local smoothing of the residuals. The blue error bars indicate the mean and standard deviation of the binned residuals. Residuals are represented by hexagonal cells with the color code indicating the number of data points.

The regression coefficients and their standard errors are presented in Table 1. The standard errors of all the coefficients are low (generally expected to be one magnitude lower than the mean). However, the standard error for the coefficient a_1 is slightly higher in all the cases. The low values of standard error for other coefficients indicate that the regressed coefficients are well constrained by the data. Since coefficient a_2 in the overall and Interface models was constrained through grid search, its standard error could not be computed. The standard deviation of the site term is the lowest for the Interface model, whereas the standard deviation of the event term is the lowest for the Intraslab model. Assuming that the event, site, and residual terms are independent, the total standard deviation can be computed using Equation (3.3).

$$\sigma_{total} = \sqrt{\tau_{event}{}^{2} + \tau_{site}{}^{2} + \sigma_{res}{}^{2}} \tag{3.3}$$

σ_{total} is the greatest for the overall model. Comparing the values in the present study with the standard deviations published in Lea17 (Lasley et al. 2017), it was observed that the event and site standard deviations are considerably lower than those from Lea17.

Similar to the observation by Lea17, n_{eq} is found not to be a function of depth. However, analysis of total residuals revealed that the total standard deviation for the model is a function of depth. The standard deviation tends to be higher at the surface, decreases as the depth increases, and becomes constant at a saturation depth. Hence, a depth-dependent standard deviation model has been developed using the functional form shown in Equation (3.4).

$$\sigma_{n_{eq}} = \max\left(\sigma_{surf} - \frac{z}{z_o}\left(\sigma_{surf} - \sigma_{depth}\right),\ \sigma_{depth}\right) \tag{3.4}$$

where σ_{surf} is the standard deviation near surface, z is depth in meters, z_o represents the saturation depth (in meters) at which the standard deviation becomes constant, and σ_{depth} is the constant standard deviation beyond z_o

Table 3.1 Regression coefficients for the n_{eq} model

Coefficients	Overall model		Interface model		Intraslab model	
	Mean	Standard Error	Mean	Standard Error	Mean	Standard Error
a_1	-5.7506	0.1156	-6.0352	0.1334	-4.7662	0.3027
a_2	0.3775	-	0.4172	-	0.2370	0.0172
a_3	-0.4535	0.0163	-0.4268	0.0190	-0.5200	0.0368
a_4	1.035	0.0171	1.0320	0.0199	1.0238	0.0353
τ_{site}	0.1523	-	0.1481	-	0.1503	-
τ_{event}	0.3472	-	0.3447	-	0.3428	-
τ_{type}	0.0717	-	-	-	-	-
σ_{res}	0.4662	-	0.4654	-	0.4639	-

σ_{total}	0.6051	-	0.5978	-	0.5961	-
σ_{surf}	0.5686	-	0.5628	-	0.5804	-
z_o	8.1350	-	8.0910	-	8.3553	-
σ_{depth}	0.4245	-	0.4268	-	0.4109	-

The models developed in the present study are compared with each other and with other published models: Lea17 and Green et al. (2020) (Gea20). Lea17 model used herein corresponds to the model for shallow-crustal active tectonic regime. Gea20 model was developed for Groningen gas field in the Netherlands. However, n_{eq} values used in developing Gea20 model were computed from single component of ground motion; therefore, the predictions by Gea20 are multiplied by 2 for appropriateness in comparisons. Figure 3.7 shows the comparison of the models developed in the present study. Interface model predicts higher n_{eq} than the Intraslab model for M_w8 scenario, but predicts lower n_{eq} for M_w6 scenario. Clearly, the reason for this observation is the magnitude scaling term. The slope a_2 is greater for the Interface model compared to Intraslab model. This observation once again justifies the separate models for interface and intraslab events.

Figure 3.8 presents the comparison of the "overall" model developed in the present study with Lea17 and Gea20 for two different $V_{s,30}$ scenarios. For $V_{s,30}$ = 360 m/s, the present model predicts much higher values than other models. The reason for this observation can be understood in two ways. First, the difference in ground motions, arising due to difference in tectonic regimes, is reflected in the number of cycles, and second, the differences in soil profiles used across studies.

The ground motion characteristics vary between tectonic regimes. The differences in significant duration of the ground motions across tectonic regimes have been studied by various researchers (Bahrampouri et al. 2021b; Lee and Green 2014; Jaimes and Garcia-Soto 2021). Bahrampouri et al. (2021b) observed that subduction motions have higher duration than shallow-crustal ground motions for similar magnitude-distance scenarios. In this study, a significant positive correlation was found between n_{eq} and

5-75% significant duration. Similar observations have also been made by other studies for shallow-crustal events in active tectonic and stable continental tectonic regimes (Lasley et al. 2017; Castiglia and Magistris 2018; Di Filippo et al. 2013). Thus, it is reasonable to expect large n_{eq} for subduction ground motions considering the long duration ground motions for subduction zone events.

Another interpretation for the high n_{eq} values can be made through the site characteristics. Figure 8b shows the comparison for $V_{s,30}$ = 230 m/s, which is representative of the soil profiles used by Lea17. In this case, the predictions of the new models are consistent with that of other models. The difference between Figures 8a and 8b clearly demonstrates the influence of site characteristics on the new models. As discussed in previous sections (Figure 3.4), n_{eq} is greatly influenced by fundamental period of the soil column. The addition of sites with short periods can significantly increase the number of cycles and hence influence the model. The high values of n_{eq} observed can simply be understood as a direct result of the shallow stiff sites used in the study. This behavior is captured by $V_{s,30}$ scaling in the model which is substantiated by strong correlation between fundamental site period and $V_{s,30}$.

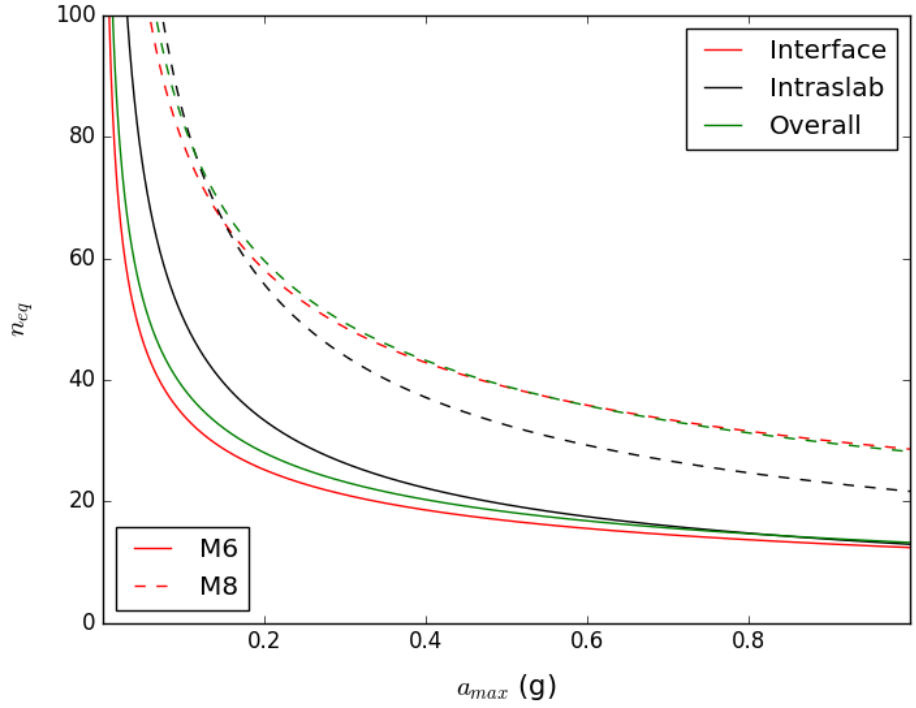

Fig 3.7 Comparison of the n_{eq} models developed in the present study. The models are plotted for $V_{s,30}$ = 360 m/s

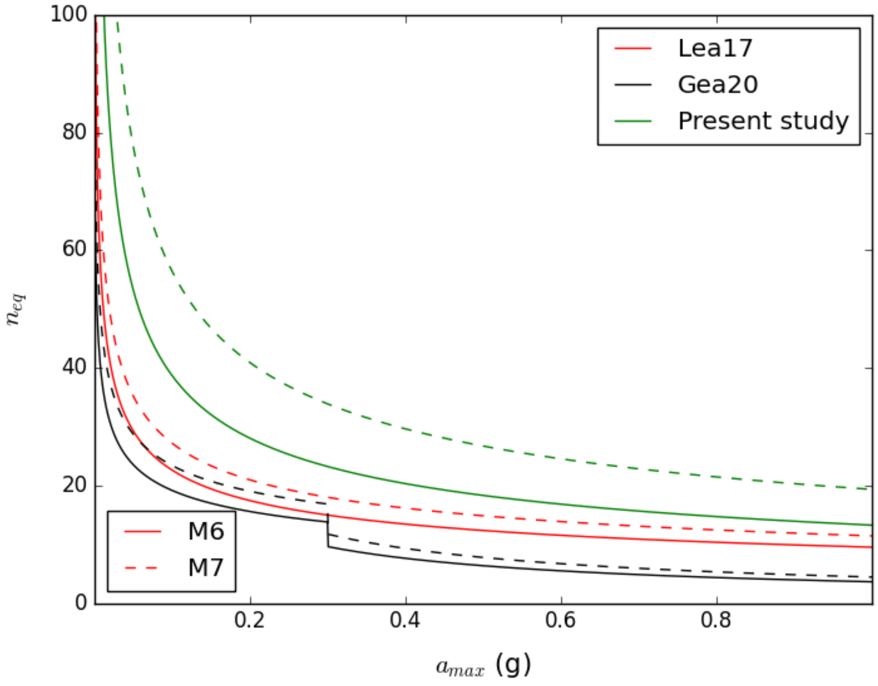

(a)

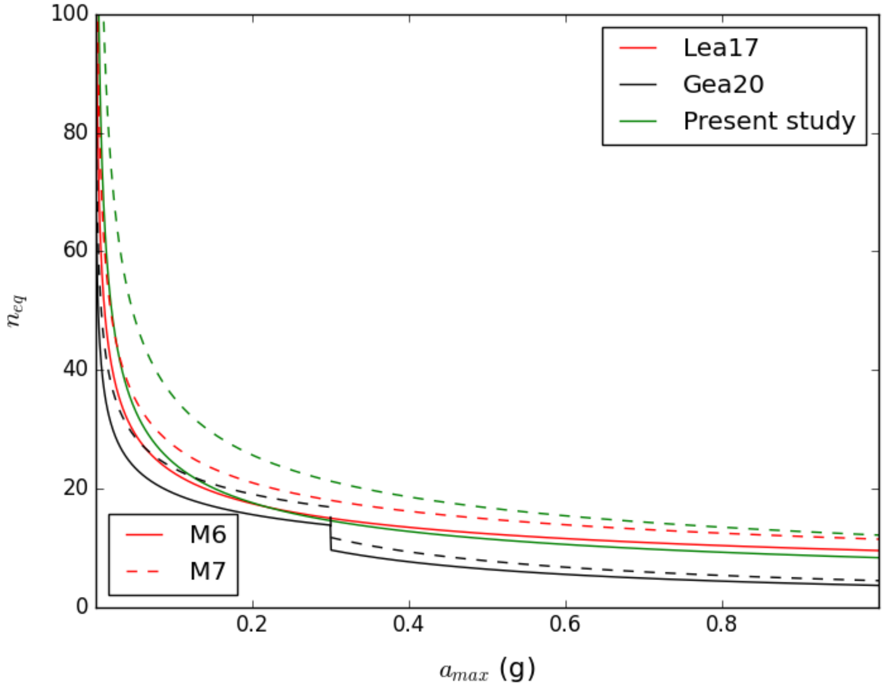

(b)

Fig 3.8 Comparison of the overall model for n_{eq} developed in the present study with Lea17 and Gea20. The models are plotted for (a) $V_{s,30}$ = 360 m/s and $V_{s,12}$ = 170 m/s, (b) $V_{s,30}$ = 230 m/s and $V_{s,12}$ = 170 m/s. Lea17 plotted here correspond to the WUS and accounts for multidirectional shaking.

The models developed in the present study are evaluated using the model efficiency coefficient (E) developed by Nash and Sutcliffe (1970). The coefficient is calculated using Equation (3.5).

$$E = 1 - \frac{\sum\left(n_{eq,actual} - n_{eq,predicted}\right)^2}{\sum\left(n_{eq,actual} - \overline{n_{eq,actual}}\right)^2} \qquad (3.5)$$

where $n_{eq,actual}$ and $n_{eq,predicted}$ are the observed and predicted n_{eq} values, respectively, and $\overline{n_{eq,actual}}$ is the mean of the observed n_{eq} values. The parameter E can take values from $-\infty$ to 1. The value of 1 indicates perfect fit. Negative values of the parameter indicate that the mean value of the observations (i.e., $\overline{n_{eq,actual}}$) is a better predictor than the model. Figure 3.9 presents the evaluation of the models developed in the present study along with Lea17 and Gea20 models. Interface and Intraslab models perform better than the overall model. It can be seen that the models developed in the present study perform better than Lea17 (developed for WUS) and Gea20 (developed for Groningen gas field in The Netherlands) in terms of predictions. However, these are not direct comparisons because the validity range of the models (for example magnitude range) are different. Nonetheless, this analysis indicates that the model captures well the trends in the data.

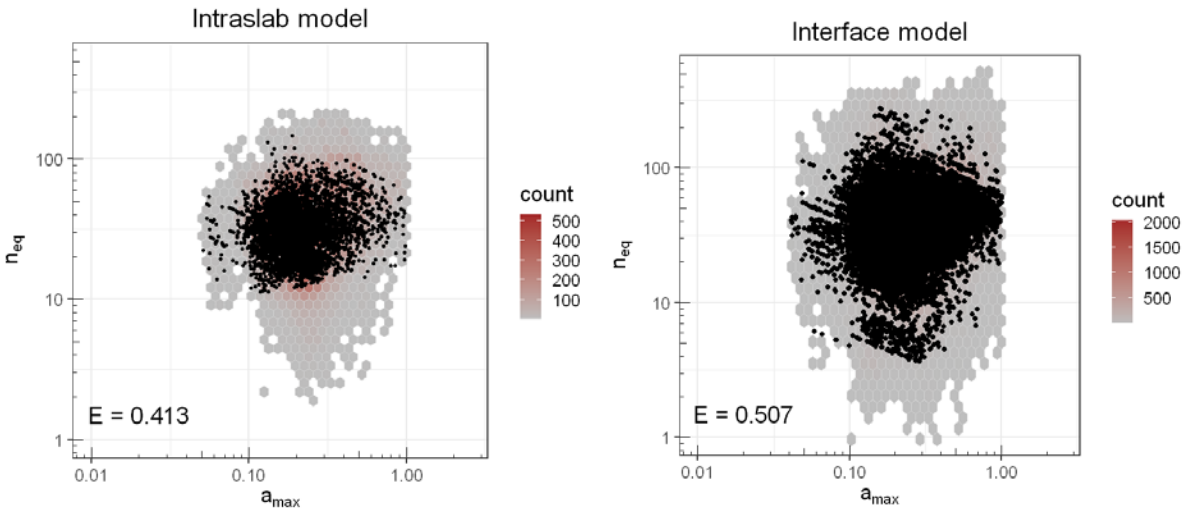

(a) (b)

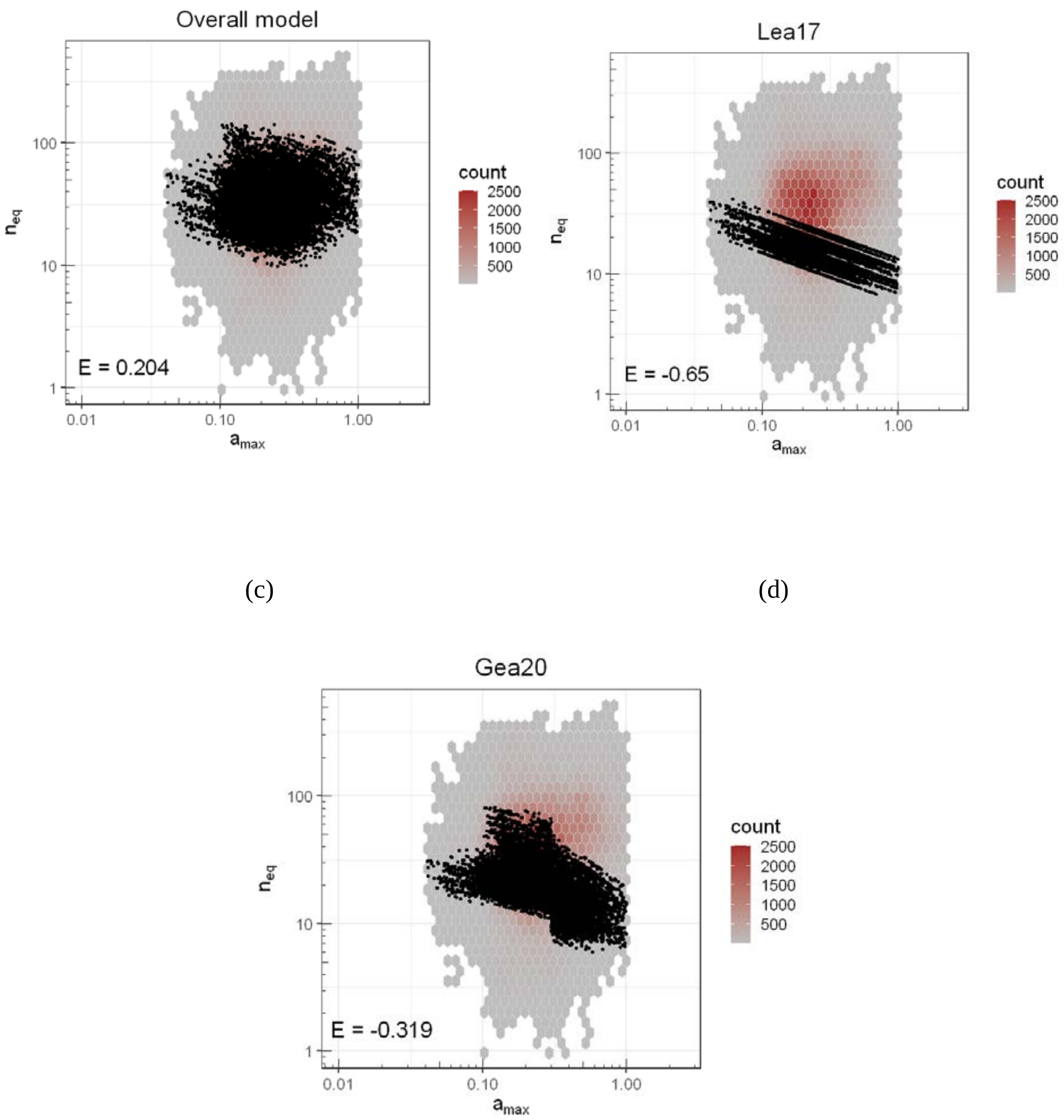

(c) (d)

(e)

Fig 3.9 Heat map showing the density of observed n_{eq} along with the predictions based on the models (a) Overall model (b) Intraslab model (c) Interface model (d) Lea17 and (e) Gea20. The hexagonal cells represent the observations with the color code indicating the count. The black dots are predictions by respective models. Gea20 predictions are multiplied by 2 to account for both the components of ground motion.

3.6.2 Stress reduction factor

The model for the stress reduction factor is based on the functional form used by Green et al. (2020). The functional form is presented in Equations (3.6) and (3.7). The functional form of Lasley et al. (2016) (Lea16) was also considered, but resulted in more bias and larger standard deviation for the model. Therefore, the Gea20 functional form was adopted. The stability of the site term is used as the basis for choosing between $V_{s,12}$ and $V_{s,30}$ as predictive variables. While there is no clear bias in the site term for the model with $V_{s,12}$, the model with $V_{s,30}$ shows slight bias for sites with high $V_{s,30}$. Also, the uncertainty (standard deviation) of the site term decreases slightly when $V_{s,12}$ is employed instead of $V_{s,30}$. Even though the use of $V_{s,12}$ in the model is not consistent with the n_{eq} model, based on these observations, the model with the $V_{s,12}$ term is selected and investigated further.

$$r_d = 1 - \frac{A_{rd}}{1 + \exp\left(-\frac{\ln(z) - (b_2 + b_6 M)}{b_3 + b_7 M}\right)} + \delta_{type} + \delta_{event} + \delta_{site} + \delta_{res} \tag{3.6}$$

$$A_{rd} = b_1 + b_4 M + b_5 \ln(a_{max}) + b_8 V_{s,12} \tag{3.7}$$

where b_1 to b_8 are regression coefficients; δ_{site}, δ_{event}, δ_{type}, and δ_{res} are profile (or site), event (nested with the type of event; interface or intraslab), type of event, and residual terms, respectively, with zero mean and standard deviations τ_{site}, τ_{event}, τ_{type}, and σ_{res}, respectively. Figure 3.10 presents the event term and site term plotted against magnitude and $V_{s,12}$ respectively.

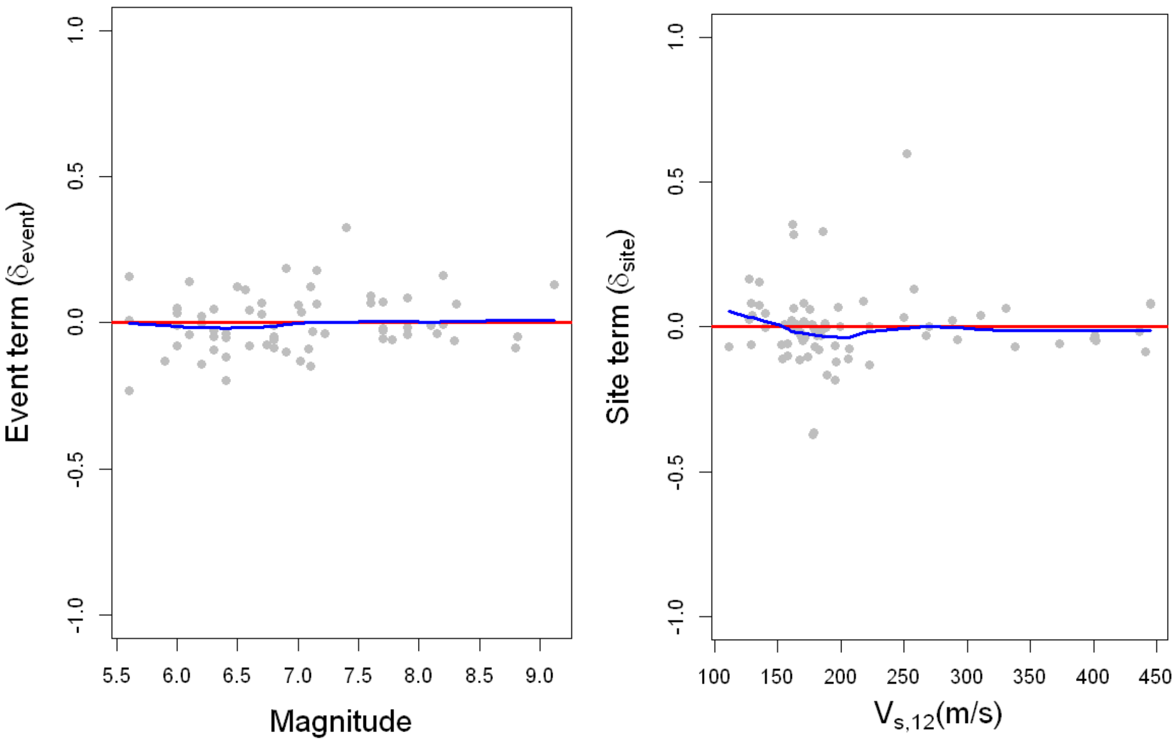

(a) (b)

Fig 3.10 (a) Event term plotted against magnitude (b) Site term plotted against $V_{s,12}$. Blue lines indicate LOESS fit to the datapoints

Figure 3.11 shows the total residual plots. No trends can be observed in the plots against magnitude, $V_{s,12}$, depth, and predominant site period. There is a slight upward deviation from the zero line at low values of a_{max}. However, these average mispredictions are well below one standard deviation of the model (0.2 units). It can also be noted that the residual plot against site period does not show any trends; therefore, there is no need to introduce site period in the model.

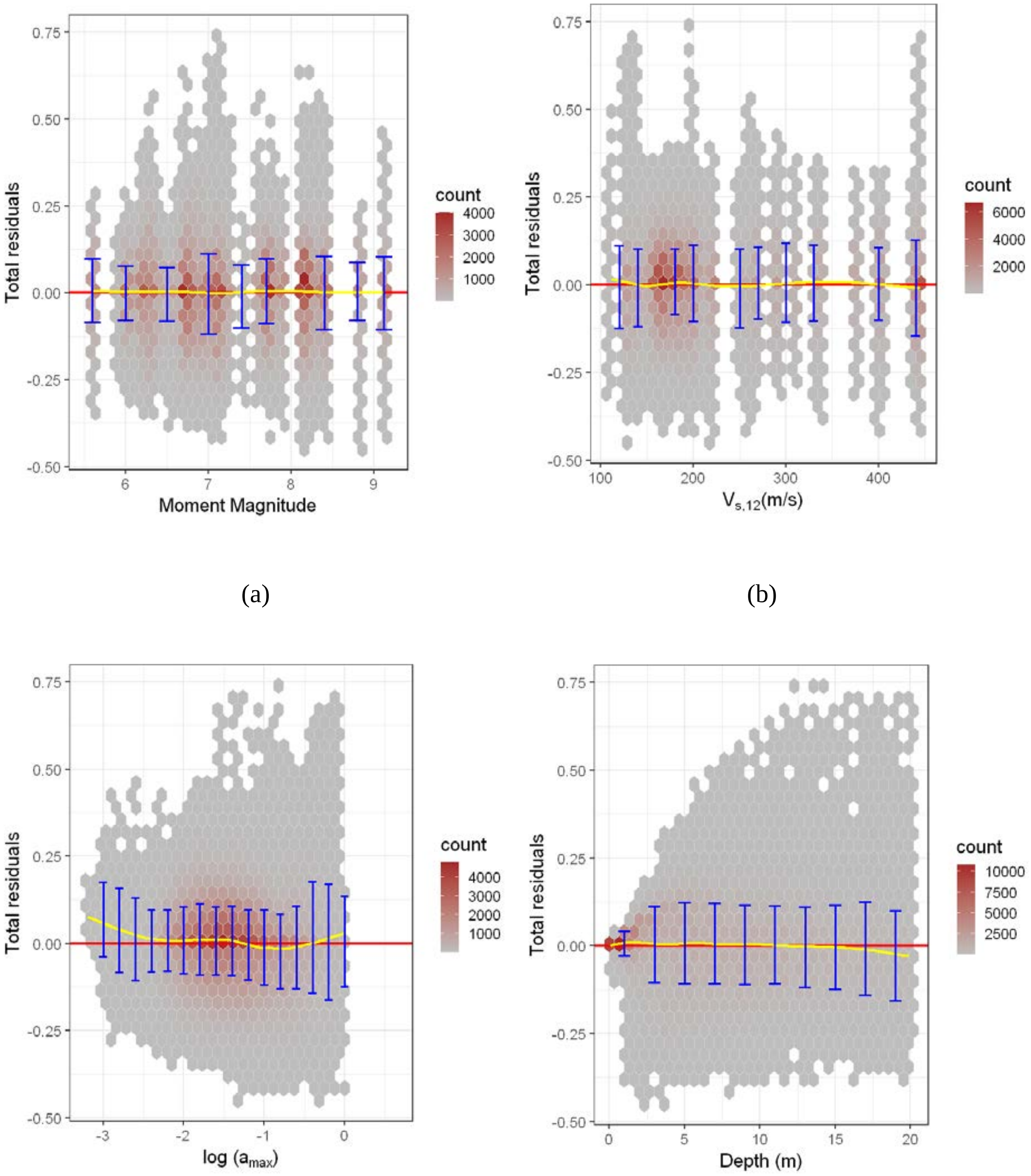

Total residuals
0.75
0.50
0.25
0.00
-0.25
-0.50
Moment Magnitude
6
7
8
9
count
4000
3000
2000
1000
V$_{s,12}$(m/s)
100
200
300
400
6000
4000
2000
log (a$_{max}$)
-3
-2
-1
0
Depth (m)
5
10
15
20
10000
7500
5000
2500

(a)

(b)

(c)

(d)

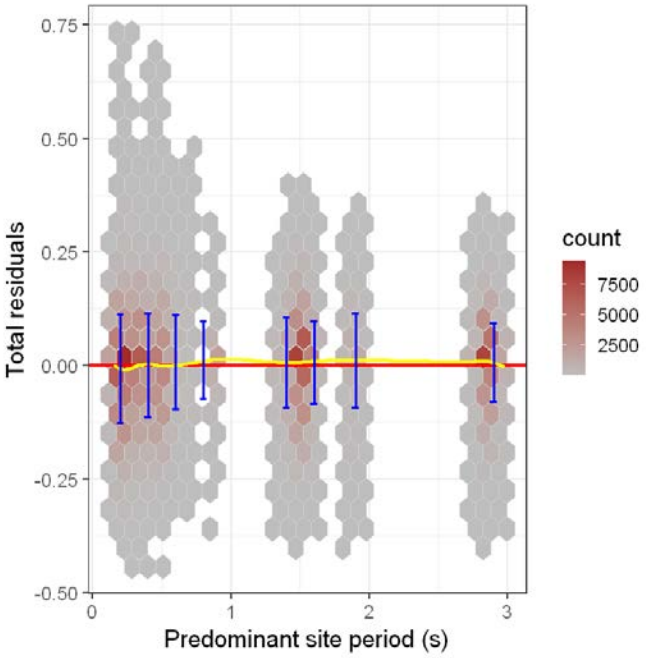

(e)

Fig 3.11 Total residuals of the model plotted against (a) Moment magnitude, (b) $V_{s,12}$, (c) a_{max}, (d) Depth, and (e) Predominant site period. Red lines indicate the zero line; Yellow lines indicate local smoothing of the residuals using LOESS fit. The blue error bars indicate the mean and standard deviation of the binned residuals. Residuals are represented by hexagonal cells with the color code indicating the number of data points.

The regression coefficients and their standard errors are presented in Table 3.2. The standard errors of all the coefficients are low (generally expected to be one magnitude lower than the mean). The standard deviation of the site term is the lowest for the Intraslab model; whereas the standard deviation of the event term is the lowest for the Interface model.

The analysis of total residuals showed that the total standard deviation decreases significantly at shallow depths. r_d values tend to approach 1 near the profile surface, and therefore, there is no spread in the data at shallow depths. This leads to more certain predictions at shallow depths. To capture this, a heteroscedastic standard deviation as a function of depth is proposed in Equation (3.8).

$$\sigma_{r_d} = \frac{b_9}{1 + \exp(b_{10} \cdot z)} \tag{3.8}$$

where b_9 and b_{10} are regression coefficients; and $\boldsymbol{z}$ is depth in meters.

Table 3.2 Regression coefficients for the r_d model

Coefficients	Overall model		Interface model		Intraslab model	
	Mean	Standard Error	Mean	Standard Error	Mean	Standard Error
b_1	1.5041	0.0680	1.5204	0.0717	1.2998	0.0532
b_2	1.0812	0.1098	1.2101	0.1129	0.4767	0.1352
b_3	0.6460	0.0657	0.6998	0.0699	0.0244	0.0848
b_4	-0.1022	0.0096	-0.1066	0.0098	-0.0645	0.0087
b_5	0.2357	0.0200	0.3006	0.0186	-0.0732	0.0215
b_6	0.0673	0.0154	0.0514	0.0155	0.1546	0.0218
b_7	-0.0105	0.0092	-0.0178	0.0094	0.0833	0.0133
b_8	-0.0010	3.3E-05	-0.0010	3.3E-05	-0.0008	2.9E-05
b_9	0.2024	-	0.2032	-	0.1988	-
b_{10}	-1.3285	-	-1.3660	-	-1.2997	-
τ_{site}	0.1157	-	0.1184	-	0.1138	-
τ_{event}	0.0968	-	0.0956	-	0.0980	-
τ_{type}	0.0086	-	-	-	-	-
σ_{res}	0.1054	-	0.1038	-	0.1074	-
σ_{total}	0.1842	-	0.1842		0.1846	-

The performance of the models developed in the study were again evaluated using the model efficiency coefficient shown in Equation (3.5). Figure 3.12 presents the evaluation of the models developed in the present study along with the Lea16 and Gea20 models. It can be seen that the models developed in the present study perform better than Lea16 (developed for WUS) and Gea20 (developed for Groningen gas field) in terms of predictions.

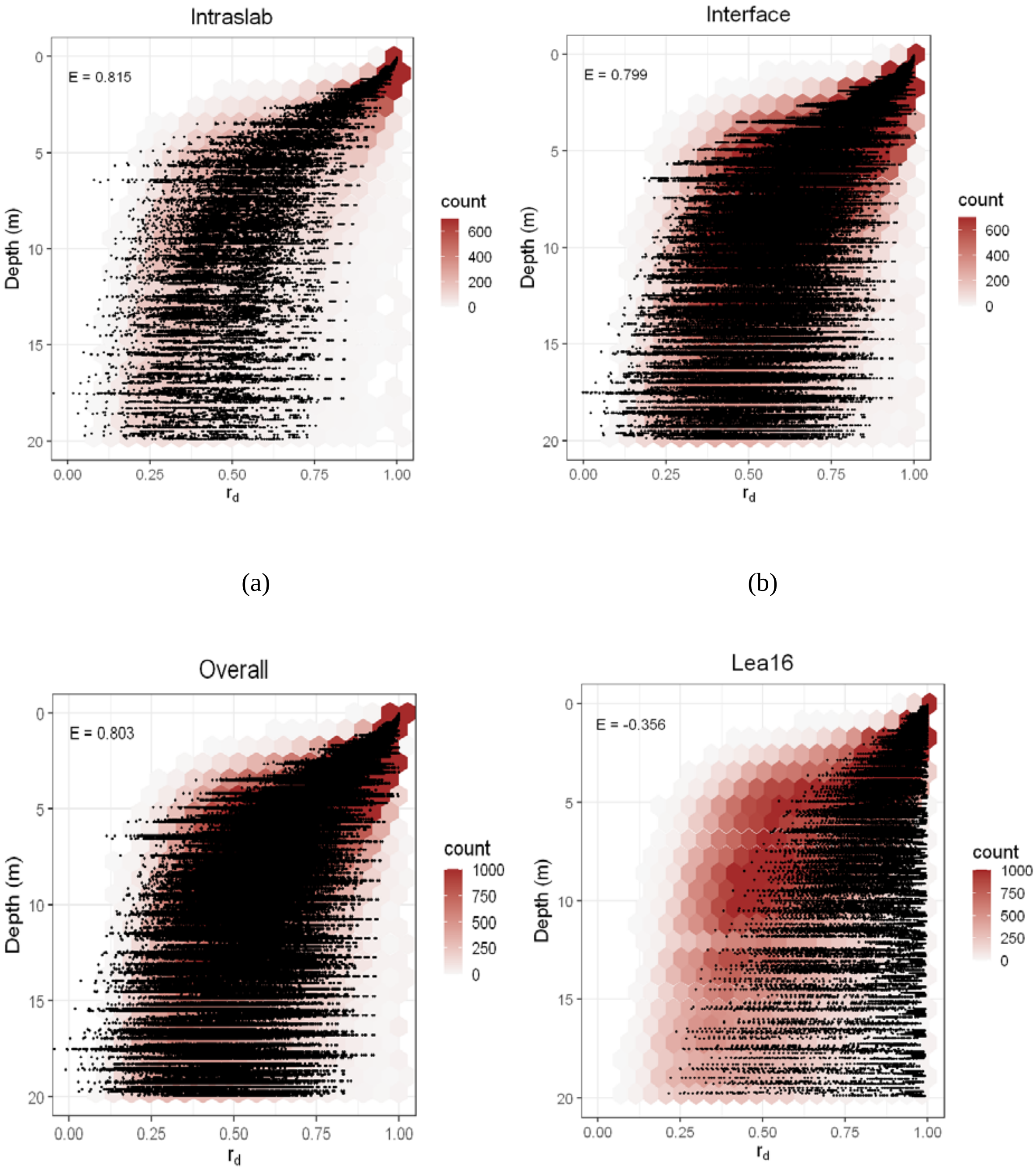

(a)

(b)

(c)

(d)

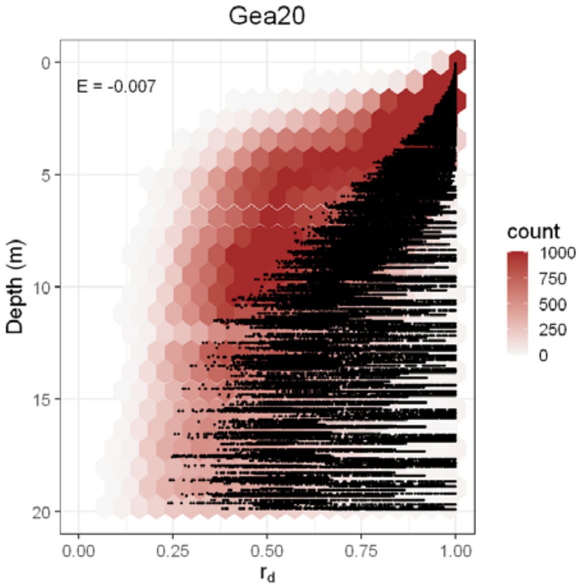

(e)

Fig 3.12 Heat map showing the density of observed r_d along with the predictions based on (a) Intraslab model (b) Interface model (c) Overall model (d) Lea16 and (e) Gea20. The hexagonal cells represent the observations with the color code indicating the count. The black dots are predictions by respective models.

Figure 3.13 shows the comparison of the models developed in the present study. It can be seen that the Interface model predicts higher r_d than Intraslab model. Figure 3.14 presents the comparison of the "Overall' model developed in the present study with Lea16 and Gea20. The present model predicts lower values than Gea20. The model predicts lower values than Lea16 at shallow depths and higher values than Lea16 at large depths.

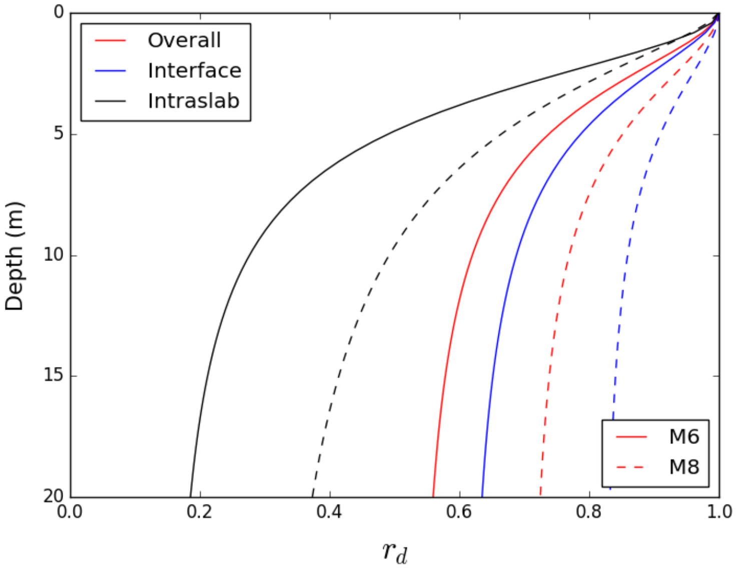

Fig 3.13 Comparison of the r_d models developed in the present study. The models are plotted for $V_{s,12}$ = 170 m/s and a_{max} = 0.35 g

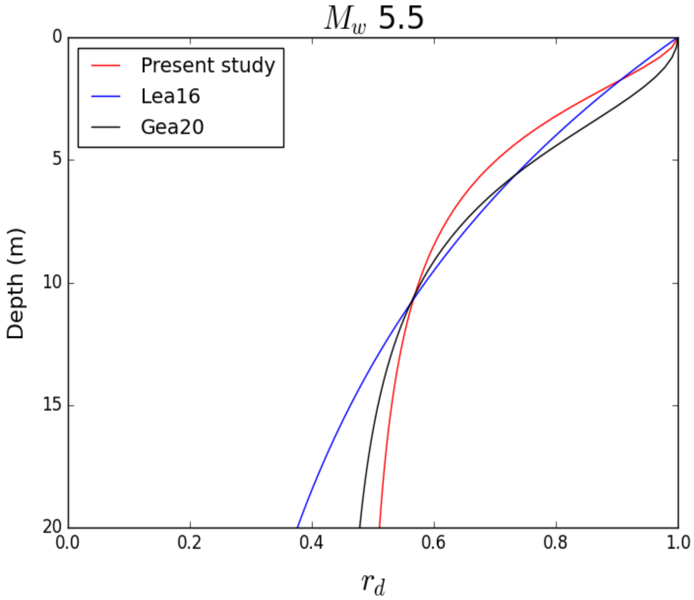

(a)

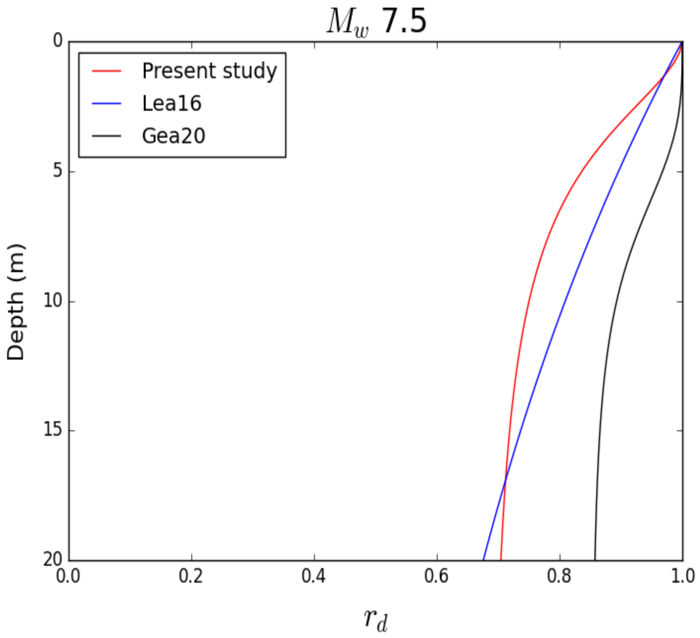

(b)

Fig 3.14 Comparison of the overall model for r_d developed in the present study with Lea16 and Gea20 for (a) M_w 5.5 and (b) M_w 7.5 scenarios. The models are plotted for $V_{s,12}$ = 170 m/s and a_{max} = 0.35 g. Lea16 plotted here correspond to WUS model.

3.7 Discussion

To understand the implications of using the proposed models in evaluating liquefaction triggering, factors of safety against liquefaction computed using these models are compared with those obtained using Green et al. (2019) (Gea19) for active shallow crustal tectonic regime. Factor of safety against liquefaction (FS) is defined as the ratio of normalized Cyclic Resistance Ratio ($CRR_{7.5}$) to the normalized CSR (CSR^*) as shown in Equation (3.9).

$$FS = \frac{CRR_{7.5}}{CSR^*} \tag{3.9}$$

For a given soil profile, the ratio of CSR^*computed using subduction zone specific models proposed in this study (${CSR^*}_{Sub}$) to that of Gea19 (${CSR^*}_{Gea19}$) can be easily derived from Equation (3.1) as given in Equation (3.10).

$$\frac{{CSR^*}_{Sub}}{{CSR^*}_{Gea19}} = \left(\frac{r_d}{MSF}\right)_{Sub} \cdot \left(\frac{MSF}{r_d}\right)_{Gea19} \tag{3.10}$$

Assuming identical $CRR_{7.5}$, the ratio of Factors of safety against liquefaction is given by,

$$\frac{FS_{Sub}}{FS_{Gea19}} = \left(\frac{r_d}{MSF}\right)_{Gea19} \cdot \left(\frac{MSF}{r_d}\right)_{Sub} \tag{3.11}$$

$(MSF)_{Gea19}$ and $(r_d)_{Gea19}$ are magnitude scaling factor and stress reduction factor proposed in Gea19, respectively, whereas, $(MSF)_{Sub}$ and $(r_d)_{Sub}$ are the subduction zone specific models developed in this study. $(r_d)_{Sub}$ can be obtained using Equations (3.6, 3.7), whereas $(MSF)_{Sub}$ can be computed using Equation (3.12).

$$MSF_{Sub} = \left\{\frac{14}{n_{eq}\ (M,\ a_{max},\ V_{s,30})}\right\}^{0.28} \tag{3.12}$$

The numerator in the expression above is the number of equivalent cycles for the reference earthquake ($M = 7.5,\ a_{max} = 0.35$) in the active shallow-crustal tectonic regime and is computed using Lea17. The denominator is the number of equivalent cycles for the subduction earthquake of interest and is computed using Equation (3.2). The value of $b = 0.28$ represents the slope of the CSR – N_{liq} curve and is suggested by Ulmer (2019) for clean sands. Ulmer (2019) used contours of constant dissipated energy from modulus reduction and damping curves to obtain the *b*-value. Figure 3.15 presents the comparison of factors of safety obtained from subduction models and those obtained from Gea19 for an arbitrary site with $V_{s,30}$ = 230 m/s and $V_{s,12}$ = 170 m/s. The subduction models result in lower factors of safety compared to Gea19 except for scenarios with high values of a_{max} (i.e., $FS_{Sub} < FS_{Gea19}$). This implies that Gea19 model would result in "false negatives" if used to evaluate liquefaction for a subduction zone event, especially when a_{max} is low. For M$_w$ 8.5 earthquake, the ratio of factor of safety increases when a_{max} = 0.25 g, but decreases when a_{max} = 1 g. This observation gains significance because of the potential of megathrust earthquakes in subduction zones. The likelihood of "false positives" (i.e., $FS_{Sub} > FS_{Gea19}$) when evaluating liquefaction potential for subduction zone events using Gea19 will be high for scenarios with large values of a_{max}, whereas, the scenarios with low values of a_{max} will result in more "false negatives."

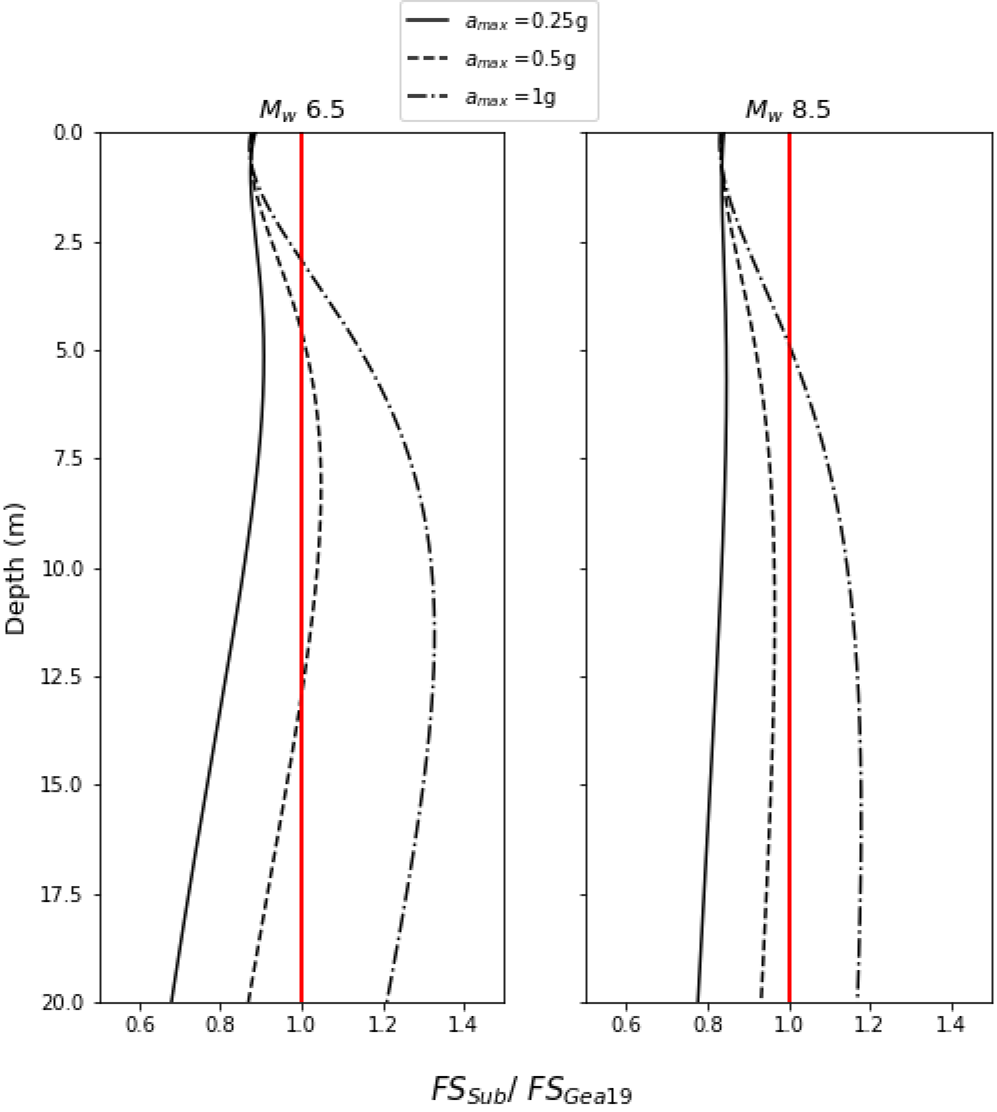

Fig 3.15 Ratio of factor of safety from subduction models to that of Gea19 plotted against depth for different magnitude and a_{max}. The values are plotted for a site with $V_{s,30}$ = 230 m/s and $V_{s,12}$ = 170 m/s. The red line indicates a ratio of 1.

3.8 Conclusion

Given the significant risk to infrastructure posed by liquefaction, it is of paramount importance that the prediction of liquefaction triggering at a site is reliable. The use of existing variants of the "simplified" procedure for megathrust earthquakes in subduction zones is questionable because of the empirical relationships inherent to the procedure, especially n_{eq} and r_d, involved in the analysis. In this study, empirical equations are developed for number of equivalent cycles (n_{eq}) and stress reduction factor (r_d) that can be reasonably used for evaluating liquefaction triggering during subduction zone events around the world. The proposed relationships are intended to be used in conjunction with the framework of "simplified" liquefaction evaluation procedure. The models are developed by regressing site response data obtained using representative soil profiles and subduction ground motions. It is observed that the number of equivalent cycles is closely correlated with predominant site period; deep soft sites with long site period resulted in larger n_{eq} compared to stiff shallow sites with short period. Hence, to avoid bias, soil profiles with wider range of site period are used in the study. However, the model does not use site period as a parameter; instead uses $V_{s,30}$ which is closely correlated to the site period. $V_{s,30}$ term employed in the model works as a proxy for site period capturing the dependence of n_{eq} on site period.

In addition to an overall model, which will make practical application simple, separate models were developed for interface and intraslab events to better quantify uncertainties in prediction. In general, n_{eq} models developed in this study show stronger and much refined scaling with $V_{s,30}$ compared to other models. The r_d models developed in the study predict softer response at shallow depths compared to other models. The models are developed using subduction ground motions and given the differences with other models, it could lead to highly erroneous results if applied in other tectonic settings. The proposed correlations are valid for magnitude range 5.5 – 9.1 and rupture distance of 20 – 225 km. The models should be used with caution for cases where design a_{max} exceeds 1g. Developed utilizing a comprehensive set of soil profiles and representative ground motions, the models proposed in this study make better predictions than other models and should result in less bias and better quantification of uncertainties.

References

Alberto-Hernandez, Y. and Towhata, I., 2017. New insight in liquefaction after recent earthquakes: Chile, New Zealand and Japan. In Earthquakes-Tectonics, Hazard and Risk Mitigation (pp. 117-137). IntechOpen Limited London.

Bahrampouri, M., Rodriguez-Marek, A. and Green, R.A., 2021. Ground motion prediction equations for significant duration using the KiK-net database. Earthquake Spectra, 37(2), pp.903-920.

Bahrampouri, M., Rodriguez-Marek, A., Shahi, S. and Dawood, H., 2021. An updated database for ground motion parameters for KiK-net records. Earthquake Spectra, 37(1), pp.505-522.

Bates, D., Maechler, M., Bolker, B., and Walker, S., 2015. Fitting linear mixed-effects models using lme4. Journal of Statistical Software, 67(1), 1–48.

Biondi, G., Cascone, E. and Maugeri, M., 2004. Number of uniform stress cycles equivalent to seismic loading. Proceedings of 11th ICSDEE & 3rd ICEGE. Berkeley, CA, USA, 2, pp.705-712.

Boulanger, R.W. and Idriss, I.M., 2014. CPT and SPT based liquefaction triggering procedures. Report No. UCD/CGM.-14, 1.

Bozorgnia, Y. and Stewart, J.P., 2020. Data Resources for NGA-Subduction Project, PEER Report 2020/02. Berkeley, Pacific Earthquake Engineering Research Center.

Castiglia, M. and de Magistris, F.S., 2018. Prediction of the number of equivalent cycles for earthquake motion. Bulletin of Earthquake Engineering, 16(9), pp.3571-3603.

Çetin, K.Ö., 2000. Reliability-based assessment of seismic soil liquefaction initiation hazard. PhD dissertation. University of California, Berkeley.

Cetin, K.O., Seed, R.B., Der Kiureghian, A., Tokimatsu, K., Harder Jr, L.F., Kayen, R.E. and Moss, R.E., 2004. Standard penetration test-based probabilistic and deterministic assessment of seismic soil liquefaction potential. Journal of Geotechnical and Geoenvironmental Engineering, 130(12), pp.1314-1340.

Darendeli, M.B. and Stokoe, K.H., 2001.Development of a new family of normalized modulus reduction and material damping curves. Geotechnical Engineering Report. GD01-1, University of Texas at Austin.

Di Filippo, G., Biondi, G. and Cascone, E., 2013. Nuovi modelli previsionali per la valutazione del numero di cicli di carico equivalente. Incontro Annuale dei Ricercatori di Geotecnica. 2013- IARG 2013 Perugia

Efron, B. and Tibshirani, R.J., 1994. An introduction to the bootstrap. Vol. 57, CRC press, Chicago.

Green, R.A. and Bommer, J.J., 2019. What is the smallest earthquake magnitude that needs to be considered in assessing liquefaction hazard?. Earthquake Spectra, 35(3), pp.1441-1464.

Green, R.A. and Terri, G.A., 2005. Number of equivalent cycles concept for liquefaction evaluations—Revisited. Journal of Geotechnical and Geoenvironmental Engineering, 131(4), pp.477-488.

Green, R.A., Bommer, J.J., Rodriguez-Marek, A., Maurer, B.W., Stafford, P.J., Edwards, B., Kruiver, P.P., De Lange, G. and Van Elk, J., 2019. Addressing limitations in existing 'simplified'liquefaction triggering evaluation procedures: application to induced seismicity in the Groningen gas field. Bulletin of Earthquake Engineering, 17(8), pp.4539-4557.

Green, R.A., Bommer, J.J., Stafford, P.J., Maurer, B.W., Kruiver, P.P., Edwards, B., Rodriguez-Marek, A., de Lange, G., Oates, S.J., Storck, T. and Omidi, P., 2020. Liquefaction Hazard in the Groningen Region of the Netherlands due to Induced Seismicity. Journal of Geotechnical and Geoenvironmental Engineering, 146(8), p.04020068.

Idriss, I. M., 1999. An update to the Seed-Idriss simplified procedure for evaluating liquefaction potential. Proceedings from TRB Workshop on New Approaches to Liquefaction Analysis, U.S. Department of Transportation, Federal Highway Administration, Washington, DC.

Idriss, I.M. and Boulanger, R.W., 2008. Soil liquefaction during earthquakes. Monograph MNO-12, Earthquake Engineering Research Institute, Oakland, CA.

Jaimes, M.A. and García-Soto, A.D., 2021. Ground-Motion Duration Prediction Model from Recorded Mexican Interplate and Intermediate-Depth Intraslab Earthquakes. Bulletin of the Seismological Society of America, 111(1), pp.258-273.

Kayen, R., Moss, R.E.S., Thompson, E.M., Seed, R.B., Cetin, K.O., Kiureghian, A.D., Tanaka, Y. and Tokimatsu, K., 2013. Shear-wave velocity–based probabilistic and deterministic assessment of seismic soil liquefaction potential. Journal of Geotechnical and Geoenvironmental Engineering, 139(3), pp.407-419.

Kayen, R.E., Dashti, S., Kokusho, T., Hazarika, H., Franke, K., Oettle, N.K., Wham, B., Calderon, J.R., Briggs, D., Guillies, S. and Cheng, K., 2017. Geotechnical aspects of the 2016 Mw 6.2, Mw 6.0, and Mw 7.0 Kumamoto earthquakes. Geotechnical Extreme Events Reconnaissance Association.

Lasley, S.J., Green, R.A. and Rodriguez-Marek, A., 2016. New stress reduction coefficient relationship for liquefaction triggering analyses. Journal of Geotechnical and Geoenvironmental Engineering, 142(11), p.06016013.

Lasley, S.J., Green, R.A. and Rodriguez-Marek, A., 2017. Number of equivalent stress cycles for liquefaction evaluations in active tectonic and stable continental regimes. Journal of Geotechnical and Geoenvironmental Engineering, 143(4), p.04016116.

Lee, J. and Green, R.A., 2014. An empirical significant duration relationship for stable continental regions. Bulletin of earthquake engineering, 12(1), pp.217-235.

Lee, J., 2009. Engineering characterization of earthquake ground motions. Ph.D. dissertation, University of Michigan, Ann Arbor.

Montalva, G. and Bastias, N., 2017.Chilean Strong Ground Motion. https://datacenterhub.org/resources/chilean_motion (last accessed August 5,2021).

Montalva, G. and Ruz, F., 2017. Liquefaction Evidence in the Chilean Subduction Zone. Proceedings from 3rd International conference on Performance Based Design in Earthquake Geotechnical Engineering. The International Society for Soil Mechanics and Geotechnical Engineering, Vancouver.

Nash, J.E. and Sutcliffe, J.V., 1970. River flow forecasting through conceptual models part I—A discussion of principles. Journal of Hydrology, 10(3), pp.282-290.

Rodriguez-Marek, A., Bay, J.A., Park, K., Montalva, G.A., Cortez-Flores, A., Wartman, J. and Boroschek, R., 2010. Engineering analysis of ground motion records from the 2001 Mw 8.4 Southern Peru earthquake. Earthquake Spectra, 26(2), pp.499-524.

Seed, H.B. and Idriss, I.M., 1971. Simplified procedure for evaluating soil liquefaction potential. Journal of the Soil Mechanics and Foundations division, 97(9), pp.1249-1273.

Seed, H.B., Idriss, I.M., Makdisi, F., Banerjee, N. (1975). Representation of Irregular Stress Time Histories by Equivalent Uniform Stress Series in Liquefaction Analysis, Report No. EERC 75-29, Earthquake Engineering Research Center, College of Engineering, University of California, Berkeley.

SIBER-RISK.,2020. SIBER-RISK strong motion database. https://siberrisk.ing.puc.cl/StrongMotionDatabase (accessed July 24, 2021).

Stafford, P.J. and Bommer, J.J., 2009. Empirical equations for the prediction of the equivalent number of cycles of earthquake ground motion. Soil Dynamics and Earthquake Engineering, 29(11-12), pp.1425-1436.

Thum, T. S., S. Lasley, R. A. Green, and A. Rodriguez-Marek., 2019. ShakeVT2: A computer program for equivalent linear site response analysis, Center for Geotechnical Practice and Research (CGPR) Report #98, The Charles E. Via, Jr. Department of Civil and Environmental Engineering, Virginia Tech.

Troost, K.G. and Booth, D.B., 2008. Geology of Seattle and the Seattle area, Washington. Reviews in Engineering Geology, 20(0), pp.1-36.

Wong, I.G., Stokoe, K.H., Cox, B.R., Lin, Y.C. and Menq, F.Y., 2011. Shear-wave velocity profiling of strong motion sites that recorded the 2001 Nisqually, Washington, earthquake. Earthquake Spectra, 27(1), pp.183-212.

Yount, J.C. and Gower, H.D., 1991. Bedrock geologic map of the Seattle 30 by 60 Quadrangle, Washington. United States Geological Survey Report - Open-File Report 91-147.

Zimmaro, P., Brandenberg, S.J., Stewart, J.P., Kwak, D.Y., Franke, K.W., Moss, R.E.S., Cetin, K.O., Can, G., Ilgac, M., Stamatakos, J., Juckett, M., Mukherjee, J., Murphy, Z., Ybarra, S., Weaver, T., Bozorgnia, Y. and Kramer, S.L., 2019. Next-Generation Liquefaction Database. Next-Generation Liquefaction Consortium. DOI: 10.21222/C2J040.

Chapter 4

Conclusion

4.1 Summary

The framework of simplified liquefaction evaluation procedure has a few drawbacks. One such drawback is that the empirical correlations inherent to the procedure are limited by the characteristics of the dataset used to develop them. This can potentially render the correlations biased when extrapolated to the conditions outside the original dataset. In order to achieve an unbiased evaluation of liquefaction, it is essential to develop site/region-specific correlations for the empirical parameters, especially MSF and r_d (Green et al. 2019). Given that no such relationships exist for subduction zones, this research focused on developing an unbiased liquefaction evaluation model with subduction zone-specific relations. New empirical relationships have been developed for the number of equivalent cycles and the stress reduction factor using representative ground motions and soil profiles. The relationships are applicable for subduction zone earthquakes in the magnitude range 5.5 – 9.1 and rupture distance (R_{rup}) of 20 – 205 km. However, it should be noted that the relationships proposed herein cannot be used in conjunction with any variant of the simplified procedure, rather it should be employed with the procedures developed using similar approaches (Green et al. 2019) to obtain unbiased predictions. The predictions of the resulting equations match well with the observations specific to subduction zones. The correlations proposed in this research can be used to obtain more robust results with better quantification of uncertainties.

The characteristics of soil profiles, especially fundamental period of the soil column, along with ground motion characteristics such as ground motion duration, have been found to greatly influence the number of equivalent cycles. Though the stress reduction factor relationships developed in this study differ from other studies based on different tectonic regimes, the difference in the values is not as strong as that for the equivalent number of cycles.

Recent liquefaction case histories in Chile and Japan highlight the necessity of an unbiased liquefaction evaluation procedure. The potential for similar large subduction earthquakes to affect large parts of the world including the coasts of Oregon, Washington, and Alaska makes this research significant. The results of this study will directly improve the prediction of liquefaction cases due to large magnitude ($M_w > 8$) earthquakes in the United States and around the world. Furthermore, it will also advance the understanding of liquefaction occurrence due to strong ground motion.

4.2 Future work

Given the importance of unbiased prediction of liquefaction triggering in subduction zones, more research on understanding the occurrence of liquefaction and validation of several liquefaction procedures for large magnitude earthquakes are warranted. Understanding liquefaction due to large magnitude events, specially at distances very close to the rupture, involves studying the dynamic soil behavior (modulus reduction and damping) at very large strains. More research should be directed towards non-linear soil behavior, especially at large strains. Also, the existing stress-based and energy-based liquefaction procedures for predicting liquefaction triggering should be validated for liquefaction cases due to megathrust earthquakes. Recent efforts like Next Generation Liquefaction (NGL) and Geotechnical Extreme Event Reconnaissance (GEER) could provide the resources for such studies. With the increasing popularity of probabilistic analysis and Performance-Based Earthquake Engineering (PBEE), uncertainties in the parameters used in the evaluation procedure and their propagation could be another focus for future research.

References

Green, R.A., Bommer, J.J., Rodriguez-Marek, A., Maurer, B.W., Stafford, P.J., Edwards, B., Kruiver, P.P., De Lange, G. and Van Elk, J., 2019. Addressing limitations in existing 'simplified'liquefaction triggering evaluation procedures: application to induced seismicity in the Groningen gas field. Bulletin of Earthquake Engineering, 17(8), pp.4539-4557.

Appendix A

Project Data

The data generated in this project consists of soil profiles used in the site response analyses, and ground motions used for the site response analyses. The information on the ground motion data is included in Appendix B. The ground motion time histories were obtained directly from the indicated references (NGA Subduction project: Bozorgnia and Stewart 2020; KiK-net database: Bahrampouri et al. 2021a; Chilean ground motion database: Montalva and Bastias 2017; and Siber-Risk; Siber-Risk 2020). These data are available from their respective data portals. The compilation of site response data is discussed in the main report. The profiles are compiled in Appendix C of this report. Additional data is given in terms of the R-code used for regression. This code is included in Appendix C of this report.

Appendix B

Subduction ground motions

The details of the subduction ground motions compiled in this study is provided in the table below. R_{rup} represents the closest distance from the recording station to the fault surface and M_w represents moment magnitude.

Table B1. Subduction ground motions compiled in this study

S. No	File Name 1	File Name 2	Earthquake	Year	M_w	R_{rup} (km)	Database	Event Type
1	NGAsubRSN1002800_BRLKBHE	NGAsubRSN1002800_BRLKBHN	Iniskin	2016	7.15	167.49	NGA Sub	Intraslab
2	NGAsubRSN4000156_CA5-EW	NGAsubRSN4000156_CA5-NS	Tohoku	2011	9.12	90.60	NGA Sub	Interface
3	NGAsubRSN4000192_D2E-EW	NGAsubRSN4000192_D2E-NS	Tohoku	2011	9.12	56.32	NGA Sub	Interface
4	NGAsubRSN4000193_D30-EW	NGAsubRSN4000193_D30-NS	Tohoku	2011	9.12	60.74	NGA Sub	Interface
5	NGAsubRSN4000463_IWTH23S2	NGAsubRSN4000463_IWTH23W2	Tohoku	2011	9.12	54.18	NGA Sub	Interface
6	NGAsubRSN4000518_MYGH04S2	NGAsubRSN4000518_MYGH04W2	Tohoku	2011	9.12	67.94	NGA Sub	Interface
7	NGAsubRSN4001062_MYG011EW	NGAsubRSN4001062_MYG011NS	Tohoku	2011	9.12	49.98	NGA Sub	Interface
8	NGAsubRSN4007340_IWTH09S2	NGAsubRSN4007340_IWTH09W2	Miyagi	2011	7.15	177.45	NGA Sub	Intraslab

9	NGAsubRSN4007347_IWTH17S2	NGAsubRSN4007347_IWTH17W2	Miyagi	2011	7.15	132.59	NGA Sub	Intraslab
10	NGAsubRSN4007389_MYGH04S2	NGAsubRSN4007389_MYGH04W2	Miyagi	2011	7.15	73.02	NGA Sub	Intraslab
11	NGAsubRSN4022568_IWTH17EW2	NGAsubRSN4022568_IWTH17NS2	SouthSanriku	2003	7.03	98.30	NGA Sub	Intraslab
12	NGAsubRSN4022835_HDKH05EW2	NGAsubRSN4022835_HDKH05NS2	Tokachi-oki	2003	8.29	84.61	NGA Sub	Interface
13	NGAsubRSN4024986_MYGH04S2	NGAsubRSN4024986_MYGH04W2	Miyagi	2005	7.22	100.86	NGA Sub	Interface
14	NGAsubRSN4024992_MYGH11S2	NGAsubRSN4024992_MYGH11W2	Miyagi	2005	7.22	86.80	NGA Sub	Interface
15	NGAsubRSN4028592_HKD113-EW	NGAsubRSN4028592_HKD113-NS	Tokachi-oki	2003	8.29	47.60	NGA Sub	Interface
16	NGAsubRSN4040376_G-1-EW	NGAsubRSN4040376_G-1-NS	Miyagi	2005	7.22	72.91	NGA Sub	Interface
17	NGAsubRSN4040378_G-3-EW	NGAsubRSN4040378_G-3-NS	Miyagi	2005	7.22	72.91	NGA Sub	Interface
18	NGAsubRSN4040379_G-4-EW	NGAsubRSN4040379_G-4-NS	Miyagi	2005	7.22	72.91	NGA Sub	Interface
19	NGAsubRSN4040396_G-1-EW	NGAsubRSN4040396_G-1-NS	Tohoku	2011	9.12	51.43	NGA Sub	Interface
20	NGAsubRSN4040397_G-2-EW	NGAsubRSN4040397_G-2-NS	Tohoku	2011	9.12	51.43	NGA Sub	Interface
21	NGAsubRSN4040459_G-4-EW	NGAsubRSN4040459_G-4-NS	Miyagi	2011	7.15	54.61	NGA Sub	Intraslab
22	NGAsubRSN6000990_PAPUD--L	NGAsubRSN6000990_PAPUD--T	Punitaqui	1997	7.09	159.40	NGA Sub	Intraslab
23	NGAsubRSN6001144_CERRO-EW	NGAsubRSN6001144_CERRO-NS	Tarapaca	2005	7.78	205.65	NGA Sub	Intraslab
24	NGAsubRSN6001149_IQUIQ-EW	NGAsubRSN6001149_IQUIQ-NS	Tarapaca	2005	7.78	136.17	NGA Sub	Intraslab
25	NGAsubRSN6001150_IDIEM--L	NGAsubRSN6001150_IDIEM--T	Tarapaca	2005	7.78	136.42	NGA Sub	Intraslab
26	NGAsubRSN6001151_PLAZA--L	NGAsubRSN6001151_PLAZA--T	Tarapaca	2005	7.78	136.76	NGA Sub	Intraslab

27	NGAsubRSN6001153_PICA-EW	NGAsubRSN6001153_PICA-NS	Tarapaca	2005	7.78	107.90	NGA Sub	Intraslab
28	NGAsubRSN6001154_PISAG--L	NGAsubRSN6001154_PISAG--T	Tarapaca	2005	7.78	144.50	NGA Sub	Intraslab
29	NGAsubRSN6001243_CENTR-EW	NGAsubRSN6001243_CENTR-NS	Antofagasta	2007	6.74	46.41	NGA Sub	Intraslab
30	NGAsubRSN6001245_MICHI-EW	NGAsubRSN6001245_MICHI-NS	Antofagasta	2007	6.74	48.11	NGA Sub	Intraslab
31	NGAsubRSN6001373_HMBCXHLE	NGAsubRSN6001373_HMBCXHLN	Iquique	2014	8.15	47.95	NGA Sub	Interface
32	NGAsubRSN6001375_PB01HLE	NGAsubRSN6001375_PB01HLN	Iquique	2014	8.15	110.67	NGA Sub	Interface
33	NGAsubRSN6001376_PB02HLE	NGAsubRSN6001376_PB02HLN	Iquique	2014	8.15	122.59	NGA Sub	Interface
34	NGAsubRSN6001385_PB11HLE	NGAsubRSN6001385_PB11HLN	Iquique	2014	8.15	63.49	NGA Sub	Interface
35	NGAsubRSN6001389_PSGCXHLE	NGAsubRSN6001389_PSGCXHLN	Iquique	2014	8.15	41.65	NGA Sub	Interface
36	NGAsubRSN6001394_TA01HNE	NGAsubRSN6001394_TA01HNN	Iquique	2014	8.15	47.35	NGA Sub	Interface
37	NGAsubRSN6001801_ROBL090	NGAsubRSN6001801_ROBL360	Maule	2010	8.81	141.99	NGA Sub	Interface
38	NGAsubRSN6001803_SLUC090	NGAsubRSN6001803_SLUC360	Maule	2010	8.81	123.71	NGA Sub	Interface
39	NGAsubRSN6001804_ANTU090	NGAsubRSN6001804_ANTU360	Maule	2010	8.81	116.93	NGA Sub	Interface
40	NGAsubRSN6001805_CLCH-E	NGAsubRSN6001805_CLCH-N	Maule	2010	8.81	133.66	NGA Sub	Interface
41	NGAsubRSN6001819_PAP-L	NGAsubRSN6001819_PAP-T	Maule	2010	8.81	176.17	NGA Sub	Interface
42	NGAsubRSN6002201_T08AHNE	NGAsubRSN6002201_T08AHNN	Iquique	2014	8.15	41.25	NGA Sub	Interface
43	NGAsubRSN6002202_T09AHNE	NGAsubRSN6002202_T09AHNN	Iquique	2014	8.15	38.82	NGA Sub	Interface
44	NGAsubRSN6002241_CO03HNE	NGAsubRSN6002241_CO03HNN	Coastal Chile	2015	8.31	64.93	NGA Sub	Interface

45	NGAsubRSN6002257_VA01HNE	NGAsubRSN6002257_VA01HNN	Coastal Chile	2015	8.31	107.82	NGA Sub	Interface
46	NGAsubRSN6002259_VA03HNE	NGAsubRSN6002259_VA03HNN	Coastal Chile	2015	8.31	117.15	NGA Sub	Interface
47	NGAsubRSN6002262_GO04HNE	NGAsubRSN6002262_GO04HNN	Coastal Chile	2015	8.31	87.36	NGA Sub	Interface
48	NGAsubRSN6003445_PB05HHE	NGAsubRSN6003445_PB05HHN	Antofagasta	2007	6.74	46.09	NGA Sub	Intraslab
49	NGAsubRSN6003922_PB02HHE	NGAsubRSN6003922_PB02HHN	Antofagasta	2011	6.56	183.42	NGA Sub	Intraslab
50	NGAsubRSN6004288_PATCXHLE	NGAsubRSN6004288_PATCXHLN	Iquique	2014	8.15	68.56	NGA Sub	Interface
51	NGAsubRSN6005358_C09OHNE	NGAsubRSN6005358_C09OHNN	Coastal Chile	2015	8.31	95.14	NGA Sub	Interface
52	NGAsubRSN6005360_C11OHNE	NGAsubRSN6005360_C11OHNN	Coastal Chile	2015	8.31	53.64	NGA Sub	Interface
53	NGAsubRSN7004767_ILA050--E	NGAsubRSN7004767_ILA050--N	Hualien City	2002	7.12	57.03	NGA Sub	Interface
54	NGAsubRSN7006045_KAU042--E	NGAsubRSN7006045_KAU042--N	Hengchun	2006	7.02	50.51	NGA Sub	Intraslab
55	GO02_50405_71654_EW	GO02_50405_71654_NS	50405	2013	5.5	117.96	Datacenterhub	Intraslab
56	GO01_50498_72177_EW	GO01_50498_72177_NS	50498	2014	7.7	113.06	Datacenterhub	Interface
57	HMBCX_50498_72178_EW	HMBCX_50498_72178_NS	50498	2014	7.7	46.02	Datacenterhub	Interface
58	MNMCX_50498_72179_EW	MNMCX_50498_72179_NS	50498	2014	7.7	120.26	Datacenterhub	Interface
59	PB01_50498_72180_EW	PB01_50498_72180_NS	50498	2014	7.7	74.64	Datacenterhub	Interface
60	PB02_50498_72181_EW	PB02_50498_72181_NS	50498	2014	7.7	57.20	Datacenterhub	Interface
61	PB11_50498_72190_EW	PB11_50498_72190_NS	50498	2014	7.7	69.80	Datacenterhub	Interface
62	RANC02S_50001_20003_EW	RANC02S_50001_20003_NS	50001	1985	7.9	70.83	Datacenterhub	Interface

63	RANC03S_50001_20004_EW	RANC03S_50001_20004_NS	50001	1985	7.9	26.79	Datacenterhub	Interface
64	MAUL06S_50001_20014_EW	MAUL06S_50001_20014_NS	50001	1985	7.9	46.99	Datacenterhub	Interface
65	VALP02S_50001_20016_EW	VALP02S_50001_20016_NS	50001	1985	7.9	39.27	Datacenterhub	Interface
66	VALP07R_50001_20020_EW	VALP07R_50001_20020_NS	50001	1985	7.9	35.57	Datacenterhub	Interface
67	VALP01R_50001_20024_EW	VALP01R_50001_20024_NS	50001	1985	7.9	39.54	Datacenterhub	Interface
68	MAUL06S_50002_20033_EW	MAUL06S_50002_20033_NS	50002	1985	7.1	81.09	Datacenterhub	Interface
69	SERE03R_50028_20051_EW	SERE03R_50028_20051_NS	50028	2002	5.9	70.63	Datacenterhub	Interface
70	SERE03R_50030_20053_EW	SERE03R_50030_20053_NS	50030	2002	6.4	58.77	Datacenterhub	Interface
71	SERE03R_50032_20055_EW	SERE03R_50032_20055_NS	50032	2003	6.8	53.34	Datacenterhub	Interface
72	SERE03R_50054_20067_EW	SERE03R_50054_20067_NS	50054	2006	6.4	39.43	Datacenterhub	Interface
73	SERE03R_50057_20068_EW	SERE03R_50057_20068_NS	50057	2007	5.4	48.04	Datacenterhub	Interface
74	ANTO04R_50062_20074_EW	ANTO04R_50062_20074_NS	50062	2007	7.7	33.96	Datacenterhub	Interface
75	TARA11R_50062_20086_EW	TARA11R_50062_20086_NS	50062	2007	7.7	67.62	Datacenterhub	Interface
76	TARA02R_50070_20099_EW	TARA02R_50070_20099_NS	50070	2008	5.1	63.44	Datacenterhub	Interface
77	TARA02R_50084_20116_EW	TARA02R_50084_20116_NS	50084	2009	6.5	49.25	Datacenterhub	Interface
78	MAUL01R_50089_20153_EW	MAUL01R_50089_20153_NS	50089	2010	6.2	57.53	Datacenterhub	Interface
79	GO01_50091_20157_EW	GO01_50091_20157_NS	50091	2014	8.1	100.51	Datacenterhub	Interface
80	HMBCX_50091_20158_EW	HMBCX_50091_20158_NS	50091	2014	8.1	48.69	Datacenterhub	Interface

81	MNMCX_50091_20159_EW	MNMCX_50091_20159_NS	50091	2014	8.1	68.86	Datacenterhub	Interface
82	PB08_50091_20167_EW	PB08_50091_20167_NS	50091	2014	8.1	101.67	Datacenterhub	Interface
83	PB11_50091_20170_EW	PB11_50091_20170_NS	50091	2014	8.1	61.85	Datacenterhub	Interface
84	T03A_50091_20175_EW	T03A_50091_20175_NS	50091	2014	8.1	40.87	Datacenterhub	Interface
85	T05A_50091_20176_EW	T05A_50091_20176_NS	50091	2014	8.1	40.84	Datacenterhub	Interface
86	PB01_50092_20180_EW	PB01_50092_20180_NS	50092	2014	7.7	74.65	Datacenterhub	Interface
87	PB02_50092_20181_EW	PB02_50092_20181_NS	50092	2014	7.7	57.20	Datacenterhub	Interface
88	PB11_50092_20187_EW	PB11_50092_20187_NS	50092	2014	7.7	69.81	Datacenterhub	Interface
89	T09A_50091_20190_EW	T09A_50091_20190_NS	50091	2014	8.1	39.48	Datacenterhub	Interface
90	T08A_50091_20191_EW	T08A_50091_20191_NS	50091	2014	8.1	42.10	Datacenterhub	Interface
91	T09A_50116_20356_EW	T09A_50116_20356_NS	50116	2014	4.9	49.50	Datacenterhub	Interface
92	T09A_50118_20366_EW	T09A_50118_20366_NS	50118	2014	5.4	100.67	Datacenterhub	Interface
93	T09A_50122_20390_EW	T09A_50122_20390_NS	50122	2014	5	95.30	Datacenterhub	Interface
94	T03A_50124_20394_EW	T03A_50124_20394_NS	50124	2014	6.6	50.80	Datacenterhub	Interface
95	T01A_50188_20631_EW	T01A_50188_20631_NS	50188	2014	5.6	46.81	Datacenterhub	Interface
96	T03A_50188_20633_EW	T03A_50188_20633_NS	50188	2014	5.6	45.99	Datacenterhub	Interface
97	T05A_50188_20635_EW	T05A_50188_20635_NS	50188	2014	5.6	46.13	Datacenterhub	Interface
98	T08A_50188_20638_EW	T08A_50188_20638_NS	50188	2014	5.6	48.29	Datacenterhub	Interface

99	TA02_50188_20644_EW	TA02_50188_20644_NS	50188	2014	5.6	46.36	Datacenterhub	Interface
100	GO03_50354_20665_EW	GO03_50354_20665_NS	50354	2013	6.8	92.73	Datacenterhub	Interface
101	GO01_50092_20694_EW	GO01_50092_20694_NS	50092	2014	7.7	113.05	Datacenterhub	Interface
102	HMBCX_50092_20695_EW	HMBCX_50092_20695_NS	50092	2014	7.7	46.02	Datacenterhub	Interface
103	MNMCX_50092_20696_EW	MNMCX_50092_20696_NS	50092	2014	7.7	120.26	Datacenterhub	Interface
104	T03A_50092_20698_EW	T03A_50092_20698_NS	50092	2014	7.7	37.10	Datacenterhub	Interface
105	T05A_50092_20699_EW	T05A_50092_20699_NS	50092	2014	7.7	37.01	Datacenterhub	Interface
106	T09A_50092_20701_EW	T09A_50092_20701_NS	50092	2014	7.7	59.65	Datacenterhub	Interface
107	T01A_50459_20705_EW	T01A_50459_20705_NS	50459	2014	5.3	51.60	Datacenterhub	Interface
108	T03A_50459_20707_EW	T03A_50459_20707_NS	50459	2014	5.3	51.18	Datacenterhub	Interface
109	T04A_50459_20708_EW	T04A_50459_20708_NS	50459	2014	5.3	51.11	Datacenterhub	Interface
110	T05A_50459_20709_EW	T05A_50459_20709_NS	50459	2014	5.3	51.06	Datacenterhub	Interface
111	T08A_50459_20712_EW	T08A_50459_20712_NS	50459	2014	5.3	51.31	Datacenterhub	Interface
112	PB02_50179_20811_EW	PB02_50179_20811_NS	50179	2014	5.1	64.28	Datacenterhub	Intraslab
113	PB02_50180_20827_EW	PB02_50180_20827_NS	50180	2014	5.6	20.62	Datacenterhub	Intraslab
114	LMEL_50335_20896_EW	LMEL_50335_20896_NS	50335	2012	5.6	124.73	Datacenterhub	Intraslab
115	V02A_50670_90064_EW	V02A_50670_90064_NS	50670	2015	8.2	32.84	Datacenterhub	Interface
116	V02A_50672_90076_EW	V02A_50672_90076_NS	50672	2015	7.6	115.02	Datacenterhub	Interface

117	CO03_50682_90098_EW	CO03_50682_90098_NS	50682	2015	6	99.94	Datacenterhub	Interface
118	CO03_50684_90105_EW	CO03_50684_90105_NS	50684	2015	6.3	76.63	Datacenterhub	Interface
119	CO03_50670_90019_EW	CO03_50670_90019_NS	50670	2015	8.2	51.99	Datacenterhub	Interface
120	VA03_50670_90024_EW	VA03_50670_90024_NS	50670	2015	8.2	63.42	Datacenterhub	Interface
121	CO03_50671_90030_EW	CO03_50671_90030_NS	50671	2015	6.8	146.88	Datacenterhub	Interface
122	VA03_50671_90034_EW	VA03_50671_90034_NS	50671	2015	6.8	141.57	Datacenterhub	Interface
123	CO03_50672_90040_EW	CO03_50672_90040_NS	50672	2015	7.6	87.83	Datacenterhub	Interface
124	VA03_50672_90044_EW	VA03_50672_90044_NS	50672	2015	7.6	123.23	Datacenterhub	Interface
125	C19O_50670_90505_EW	C19O_50670_90505_NS	50670	2015	8.2	29.33	Datacenterhub	Interface
126	C07O_50687_91066_EW	C07O_50687_91066_NS	50687	2015	6.7	83.81	Datacenterhub	Interface
127	CO03_50687_91079_EW	CO03_50687_91079_NS	50687	2015	6.7	95.97	Datacenterhub	Interface
128	20050613_7.9Mw_19.32S_69.04W_111KM_ARICA CERRO LA CRUZ_EW	20050613_7.9Mw_19.32S_69.04W_111KM_ARICA CERRO LA CRUZ_NS	20050613	2005	7.9	178.81	SiberRiskChile	Intraslab
129	20071114_7.7Mw_22.24S_70.07W_39KM_TOCOPILLA PUERTO_EW	20071114_7.7Mw_22.24S_70.07W_39KM_TOCOPILLA PUERTO_NS	20071114	2007	7.7	27.85	SiberRiskChile	Interface
130	20100227_8.8Mw_36.10S_73.08W_30KM_CURICO_EW	20100227_8.8Mw_36.10S_73.08W_30KM_CURICO_NS	20100227	2010	8.8	73.40	SiberRiskChile	Interface
131	20140401_8.2Mw_19.57S_70.91W_38KM_PB01_EW	20140401_8.2Mw_19.57S_70.91W_38KM_PB01_NS	20140401	2014	8.2	86.82	SiberRiskChile	Interface

132	20140401_8.2Mw_19.57S_70.91W_38KM_PB08_EW	20140401_8.2Mw_19.57S_70.91W_38KM_PB08_NS	20140401	2014	8.2	86.99	SiberRiskChile	Interface
133	20140401_8.2Mw_19.57S_70.91W_38KM_PB02_EW	20140401_8.2Mw_19.57S_70.91W_38KM_PB02_NS	20140401	2014	8.2	79.19	SiberRiskChile	Interface
134	20140401_8.2Mw_19.57S_70.91W_38KM_HMBCX_EW	20140401_8.2Mw_19.57S_70.91W_38KM_HMBCX_NS	20140401	2014	8.2	60.16	SiberRiskChile	Interface
135	20140401_8.2Mw_19.57S_70.91W_38KM_MNMCX_EW	20140401_8.2Mw_19.57S_70.91W_38KM_MNMCX_NS	20140401	2014	8.2	82.59	SiberRiskChile	Interface
136	20140401_8.2Mw_19.57S_70.91W_38KM_T08A_EW	20140401_8.2Mw_19.57S_70.91W_38KM_T08A_NS	20140401	2014	8.2	49.13	SiberRiskChile	Interface
137	20140401_8.2Mw_19.57S_70.91W_38KM_T03A_EW	20140401_8.2Mw_19.57S_70.91W_38KM_T03A_NS	20140401	2014	8.2	45.40	SiberRiskChile	Interface
138	20140401_8.2Mw_19.57S_70.91W_38KM_PB11_EW	20140401_8.2Mw_19.57S_70.91W_38KM_PB11_NS	20140401	2014	8.2	71.24	SiberRiskChile	Interface
139	20140401_8.2Mw_19.57S_70.91W_38KM_PSGCX_EW	20140401_8.2Mw_19.57S_70.91W_38KM_PSGCX_NS	20140401	2014	8.2	50.43	SiberRiskChile	Interface
140	20140401_8.2Mw_19.57S_70.91W_38KM_T09A_EW	20140401_8.2Mw_19.57S_70.91W_38KM_T09A_NS	20140401	2014	8.2	47.11	SiberRiskChile	Interface
141	20140401_8.2Mw_19.57S_70.91W_38KM_GO01_EW	20140401_8.2Mw_19.57S_70.91W_38KM_GO01_NS	20140401	2014	8.2	100.94	SiberRiskChile	Interface
142	20140401_8.2Mw_19.57S_70.91W_38KM_TA01_EW	20140401_8.2Mw_19.57S_70.91W_38KM_TA01_NS	20140401	2014	8.2	38.85	SiberRiskChile	Interface
143	20140401_8.2Mw_19.57S_70.91W_38KM_T06A_EW	20140401_8.2Mw_19.57S_70.91W_38KM_T06A_NS	20140401	2014	8.2	45.31	SiberRiskChile	Interface

144	20140401_8.2Mw_19.57S_70.91W_38KM_T05A_EW	20140401_8.2Mw_19.57S_70.91W_38KM_T05A_NS	20140401	2014	8.2	44.67	SiberRiskChile	Interface
145	20150823_6Mw_29.72S_71.25W_50KM_C09O_EW	20150823_6Mw_29.72S_71.25W_50KM_C09O_NS	20150823	2015	6	55.29	SiberRiskChile	Interface
146	20150823_6Mw_29.72S_71.25W_50KM_C20O_EW	20150823_6Mw_29.72S_71.25W_50KM_C20O_NS	20150823	2015	6	57.63	SiberRiskChile	Interface
147	20150916_7.6Mw_31.59S_71.79W_16KM_C18O_EW	20150916_7.6Mw_31.59S_71.79W_16KM_C18O_NS	20150916	2015	7.6	138.12	SiberRiskChile	Interface
148	20150916_7.6Mw_31.59S_71.79W_16KM_C23O_EW	20150916_7.6Mw_31.59S_71.79W_16KM_C23O_NS	20150916	2015	7.6	54.86	SiberRiskChile	Interface
149	20150916_7.6Mw_31.59S_71.79W_16KM_C11O_EW	20150916_7.6Mw_31.59S_71.79W_16KM_C11O_NS	20150916	2015	7.6	87.62	SiberRiskChile	Interface
150	20150916_8.4Mw_31.55S_71.86W_11KM_C10O_EW	20150916_8.4Mw_31.55S_71.86W_11KM_C10O_NS	20150916	2015	8.4	67.85	SiberRiskChile	Interface
151	20150916_8.4Mw_31.55S_71.86W_11KM_C23O_EW	20150916_8.4Mw_31.55S_71.86W_11KM_C23O_NS	20150916	2015	8.4	49.87	SiberRiskChile	Interface
152	20150916_8.4Mw_31.55S_71.86W_11KM_CO06_EW	20150916_8.4Mw_31.55S_71.86W_11KM_CO06_NS	20150916	2015	8.4	25.86	SiberRiskChile	Interface
153	20150916_8.4Mw_31.55S_71.86W_11KM_CO03_EW	20150916_8.4Mw_31.55S_71.86W_11KM_CO03_NS	20150916	2015	8.4	56.36	SiberRiskChile	Interface
154	20150916_8.4Mw_31.55S_71.86W_11KM_VA03_EW	20150916_8.4Mw_31.55S_71.86W_11KM_VA03_NS	20150916	2015	8.4	84.77	SiberRiskChile	Interface
155	20150916_8.4Mw_31.55S_71.86W_11KM_C20O_EW	20150916_8.4Mw_31.55S_71.86W_11KM_C20O_NS	20150916	2015	8.4	63.01	SiberRiskChile	Interface

156	20150916_8.4Mw_31.55S_71.86W_11KM_C09O_EW	20150916_8.4Mw_31.55S_71.86W_11KM_C09O_NS	20150916	2015	8.4	100.37	SiberRiskChile	Interface
157	20150916_8.4Mw_31.55S_71.86W_11KM_C14O_EW	20150916_8.4Mw_31.55S_71.86W_11KM_C14O_NS	20150916	2015	8.4	95.44	SiberRiskChile	Interface
158	20150916_8.4Mw_31.55S_71.86W_11KM_C19O_EW	20150916_8.4Mw_31.55S_71.86W_11KM_C19O_NS	20150916	2015	8.4	54.79	SiberRiskChile	Interface
159	20150916_8.4Mw_31.55S_71.86W_11KM_C22O_EW	20150916_8.4Mw_31.55S_71.86W_11KM_C22O_NS	20150916	2015	8.4	62.02	SiberRiskChile	Interface
160	20150916_8.4Mw_31.55S_71.86W_11KM_C11O_EW	20150916_8.4Mw_31.55S_71.86W_11KM_C11O_NS	20150916	2015	8.4	46.31	SiberRiskChile	Interface
161	20150916_8.4Mw_31.55S_71.86W_11KM_C18O_EW	20150916_8.4Mw_31.55S_71.86W_11KM_C18O_NS	20150916	2015	8.4	75.82	SiberRiskChile	Interface
162	20150926_6.3Mw_30.79S_71.42W_40KM_C11O_EW	20150926_6.3Mw_30.79S_71.42W_40KM_C11O_NS	20150926	2015	6.3	60.37	SiberRiskChile	Interface
163	20150926_6.3Mw_30.79S_71.42W_40KM_CO03_EW	20150926_6.3Mw_30.79S_71.42W_40KM_CO03_NS	20150926	2015	6.3	80.56	SiberRiskChile	Interface
164	20150926_6.3Mw_30.79S_71.42W_40KM_C10O_EW	20150926_6.3Mw_30.79S_71.42W_40KM_C10O_NS	20150926	2015	6.3	80.16	SiberRiskChile	Interface
165	20150926_6.3Mw_30.79S_71.42W_40KM_C23O_EW	20150926_6.3Mw_30.79S_71.42W_40KM_C23O_NS	20150926	2015	6.3	124.45	SiberRiskChile	Interface
166	20150926_6.3Mw_30.79S_71.42W_40KM_C18O_EW	20150926_6.3Mw_30.79S_71.42W_40KM_C18O_NS	20150926	2015	6.3	99.82	SiberRiskChile	Interface
167	20150926_6.3Mw_30.79S_71.42W_40KM_C14O_EW	20150926_6.3Mw_30.79S_71.42W_40KM_C14O_NS	20150926	2015	6.3	122.27	SiberRiskChile	Interface

168	20151107_6.8Mw_30.87S_71.43W_47KM_C14O_EW	20151107_6.8Mw_30.87S_71.43W_47KM_C14O_NS	20151107	2015	6.8	130.72	SiberRiskChile	Interface
169	20151107_6.8Mw_30.87S_71.43W_47KM_C18O_EW	20151107_6.8Mw_30.87S_71.43W_47KM_C18O_NS	20151107	2015	6.8	108.51	SiberRiskChile	Interface
170	20151107_6.8Mw_30.87S_71.43W_47KM_C23O_EW	20151107_6.8Mw_30.87S_71.43W_47KM_C23O_NS	20151107	2015	6.8	119.59	SiberRiskChile	Interface
171	20151107_6.8Mw_30.87S_71.43W_47KM_C07O_EW	20151107_6.8Mw_30.87S_71.43W_47KM_C07O_NS	20151107	2015	6.8	99.72	SiberRiskChile	Interface
172	20151107_6.8Mw_30.87S_71.43W_47KM_CO03_EW	20151107_6.8Mw_30.87S_71.43W_47KM_CO03_NS	20151107	2015	6.8	84.89	SiberRiskChile	Interface
173	20151107_6.8Mw_30.87S_71.43W_47KM_CO06_EW	20151107_6.8Mw_30.87S_71.43W_47KM_CO06_NS	20151107	2015	6.8	55.33	SiberRiskChile	Interface
174	20151107_6.8Mw_30.87S_71.43W_47KM_C10O_EW	20151107_6.8Mw_30.87S_71.43W_47KM_C10O_NS	20151107	2015	6.8	90.85	SiberRiskChile	Interface
175	20151107_6.8Mw_30.87S_71.43W_47KM_C20O_EW	20151107_6.8Mw_30.87S_71.43W_47KM_C20O_NS	20151107	2015	6.8	110.49	SiberRiskChile	Interface
176	20151107_6Mw_30.72S_71.37W_48KM_C10O_EW	20151107_6Mw_30.72S_71.37W_48KM_C10O_NS	20151107	2015	6	77.12	SiberRiskChile	Interface
177	20151121_6Mw_30.61S_71.8W_34KM_CO06_EW	20151121_6Mw_30.61S_71.8W_34KM_CO06_NS	20151121	2015	6	38.14	SiberRiskChile	Interface
178	20151219_6Mw_30.64S_71.31W_49KM_C18O_EW	20151219_6Mw_30.64S_71.31W_49KM_C18O_NS	20151219	2015	6	88.09	SiberRiskChile	Interface
179	20160210_6.4Mw_30.63S_71.65W_37KM_CO06_EW	20160210_6.4Mw_30.63S_71.65W_37KM_CO06_NS	20160210	2016	6.4	37.34	SiberRiskChile	Interface

180	20160725_6Mw_26.11S_70.48W_60KM_A10F_EW	20160725_6Mw_26.11S_70.48W_60KM_A10F_NS	20160725	2016	6	97.66	SiberRiskChile	Interface
181	20160725_6Mw_26.11S_70.48W_60KM_A05C_EW	20160725_6Mw_26.11S_70.48W_60KM_A05C_NS	20160725	2016	6	151.09	SiberRiskChile	Interface
182	20160725_6Mw_26.11S_70.48W_60KM_GO02_EW	20160725_6Mw_26.11S_70.48W_60KM_GO02_NS	20160725	2016	6	149.72	SiberRiskChile	Interface
183	20160725_6Mw_26.11S_70.48W_60KM_A16C_EW	20160725_6Mw_26.11S_70.48W_60KM_A16C_NS	20160725	2016	6	105.18	SiberRiskChile	Interface
184	20160725_6Mw_26.11S_70.48W_60KM_AC01_EW	20160725_6Mw_26.11S_70.48W_60KM_AC01_NS	20160725	2016	6	61.29	SiberRiskChile	Interface
185	20161104_6.4Mw_35.06S_71W_95KM_M02L_EW	20161104_6.4Mw_35.06S_71W_95KM_M02L_NS	20161104	2016	6.4	96.75	SiberRiskChile	Intraslab
186	20170424_6.9Mw_33.09S_72.09W_24KM_VA01_EW	20170424_6.9Mw_33.09S_72.09W_24KM_VA01_NS	20170424	2017	6.9	49.10	SiberRiskChile	Interface
187	20170424_6.9Mw_33.09S_72.09W_24KM_BO04_EW	20170424_6.9Mw_33.09S_72.09W_24KM_BO04_NS	20170424	2017	6.9	171.24	SiberRiskChile	Interface
188	20171010_6.3Mw_18.49S_69.74W_99KM_A16P_EW	20171010_6.3Mw_18.49S_69.74W_99KM_A16P_NS	20171010	2017	6.3	131.65	SiberRiskChile	Intraslab
189	20171010_6.3Mw_18.49S_69.74W_99KM_A19P_EW	20171010_6.3Mw_18.49S_69.74W_99KM_A19P_NS	20171010	2017	6.3	115.04	SiberRiskChile	Intraslab
190	20180121_6.2Mw_18.88S_69.61W_129KM_A19P_EW	20180121_6.2Mw_18.88S_69.61W_129KM_A19P_NS	20180121	2018	6.2	153.66	SiberRiskChile	Intraslab
191	20180121_6.2Mw_18.88S_69.61W_129KM_T15A_EW	20180121_6.2Mw_18.88S_69.61W_129KM_T15A_NS	20180121	2018	6.2	202.36	SiberRiskChile	Intraslab

192	20180121_6.2Mw_18.88S_69.61W_129KM_A16P_EW	20180121_6.2Mw_18.88S_69.61W_129KM_A16P_NS	20180121	2018	6.2	145.28	SiberRiskChile	Intraslab
193	20180121_6.2Mw_18.88S_69.61W_129KM_GO01_EW	20180121_6.2Mw_18.88S_69.61W_129KM_GO01_NS	20180121	2018	6.2	161.18	SiberRiskChile	Intraslab
194	20180410_6.2Mw_31.0S_71.54W_74KM_C23O_EW	20180410_6.2Mw_31.0S_71.54W_74KM_C23O_NS	20180410	2018	6.2	125.88	SiberRiskChile	Intraslab
195	20180410_6.2Mw_31.0S_71.54W_74KM_C08O_EW	20180410_6.2Mw_31.0S_71.54W_74KM_C08O_NS	20180410	2018	6.2	92.29	SiberRiskChile	Intraslab
196	20180410_6.2Mw_31.0S_71.54W_74KM_CO03_EW	20180410_6.2Mw_31.0S_71.54W_74KM_CO03_NS	20180410	2018	6.2	111.04	SiberRiskChile	Intraslab
197	20180410_6.2Mw_31.0S_71.54W_74KM_CO06_EW	20180410_6.2Mw_31.0S_71.54W_74KM_CO06_NS	20180410	2018	6.2	82.77	SiberRiskChile	Intraslab
198	20180410_6.2Mw_31.0S_71.54W_74KM_C29O_EW	20180410_6.2Mw_31.0S_71.54W_74KM_C29O_NS	20180410	2018	6.2	91.92	SiberRiskChile	Intraslab
199	20180410_6.2Mw_31.0S_71.54W_74KM_C11O_EW	20180410_6.2Mw_31.0S_71.54W_74KM_C11O_NS	20180410	2018	6.2	98.23	SiberRiskChile	Intraslab
200	20180410_6.2Mw_31.0S_71.54W_74KM_C18O_EW	20180410_6.2Mw_31.0S_71.54W_74KM_C18O_NS	20180410	2018	6.2	136.75	SiberRiskChile	Intraslab
201	20180907_6.1Mw_28.91S_70.17W_97KM_C27O_EW	20180907_6.1Mw_28.91S_70.17W_97KM_C27O_NS	20180907	2018	6.1	123.32	SiberRiskChile	Intraslab
202	20181101_6.3Mw_19.65S_69.41W_101KM_PB11_EW	20181101_6.3Mw_19.65S_69.41W_101KM_PB11_NS	20181101	2018	6.3	104.90	SiberRiskChile	Intraslab
203	20181101_6.3Mw_19.65S_69.41W_101KM_GO01_EW	20181101_6.3Mw_19.65S_69.41W_101KM_GO01_NS	20181101	2018	6.3	103.49	SiberRiskChile	Intraslab

204	20181101_6.3Mw_19.65S_69.41W_101KM_T12A_EW	20181101_6.3Mw_19.65S_69.41W_101KM_T12A_NS	20181101	2018	6.3	112.86	SiberRiskChile	Intraslab
205	20181101_6.3Mw_19.65S_69.41W_101KM_T15A_EW	20181101_6.3Mw_19.65S_69.41W_101KM_T15A_NS	20181101	2018	6.3	137.34	SiberRiskChile	Intraslab
206	20190120_6.7Mw_30.28S_71.36W_50KM_C09O_EW	20190120_6.7Mw_30.28S_71.36W_50KM_C09O_NS	20190120	2019	6.7	99.76	SiberRiskChile	Interface
207	20190120_6.7Mw_30.28S_71.36W_50KM_C11O_EW	20190120_6.7Mw_30.28S_71.36W_50KM_C11O_NS	20190120	2019	6.7	78.02	SiberRiskChile	Interface
208	20190120_6.7Mw_30.28S_71.36W_50KM_C19O_EW	20190120_6.7Mw_30.28S_71.36W_50KM_C19O_NS	20190120	2019	6.7	54.08	SiberRiskChile	Interface
209	20190120_6.7Mw_30.28S_71.36W_50KM_C14O_EW	20190120_6.7Mw_30.28S_71.36W_50KM_C14O_NS	20190120	2019	6.7	98.77	SiberRiskChile	Interface
210	20190120_6.7Mw_30.28S_71.36W_50KM_C27O_EW	20190120_6.7Mw_30.28S_71.36W_50KM_C27O_NS	20190120	2019	6.7	125.67	SiberRiskChile	Interface
211	20190120_6.7Mw_30.28S_71.36W_50KM_C22O_EW	20190120_6.7Mw_30.28S_71.36W_50KM_C22O_NS	20190120	2019	6.7	60.88	SiberRiskChile	Interface
212	20190120_6.7Mw_30.28S_71.36W_50KM_C08O_EW	20190120_6.7Mw_30.28S_71.36W_50KM_C08O_NS	20190120	2019	6.7	117.10	SiberRiskChile	Interface
213	20190120_6.7Mw_30.28S_71.36W_50KM_C29O_EW	20190120_6.7Mw_30.28S_71.36W_50KM_C29O_NS	20190120	2019	6.7	63.15	SiberRiskChile	Interface
214	20190120_6.7Mw_30.28S_71.36W_50KM_C18O_EW	20190120_6.7Mw_30.28S_71.36W_50KM_C18O_NS	20190120	2019	6.7	82.97	SiberRiskChile	Interface
215	20190120_6.7Mw_30.28S_71.36W_50KM_C10O_EW	20190120_6.7Mw_30.28S_71.36W_50KM_C10O_NS	20190120	2019	6.7	56.90	SiberRiskChile	Interface

216	20190120_6.7Mw_30.28S_71.36W_50KM_C23O_EW	20190120_6.7Mw_30.28S_71.36W_50KM_C23O_NS	20190120	2019	6.7	177.34	SiberRiskChile	Interface
217	20190120_6.7Mw_30.28S_71.36W_50KM_CO03_EW	20190120_6.7Mw_30.28S_71.36W_50KM_CO03_NS	20190120	2019	6.7	102.07	SiberRiskChile	Interface
218	20190120_6.7Mw_30.28S_71.36W_50KM_CO05_EW	20190120_6.7Mw_30.28S_71.36W_50KM_CO05_NS	20190120	2019	6.7	65.03	SiberRiskChile	Interface
219	20191104_6.1Mw_31.81S_71.34W_56KM_CO04_EW	20191104_6.1Mw_31.81S_71.34W_56KM_CO04_NS	20191104	2019	6.1	70.59	SiberRiskChile	Interface
220	AKTH020305261824-E	AKTH020305261824-N	Off Miyagi	2003	7	140.90	kik-net	Interface
221	AKTH060806140843-E	AKTH060806140843-N	Iwate - Miyagi Nairiku	2008	6.9	26.94	kik-net	Interface
222	AKTH180806140843-E	AKTH180806140843-N	Iwate - Miyagi Nairiku	2008	6.9	49.97	kik-net	Interface
223	HDKH050309260450-E	HDKH050309260450-N	Tokachi-oki	2003	7.9	150.10	kik-net	Interface
224	IBRH141104111716-E	IBRH141104111716-N	Fukushima Hamadori	2011	6.6	26.50	kik-net	Intraslab
225	IBRH161104111716-E	IBRH161104111716-N	Fukushima Hamadori	2011	6.6	37.59	kik-net	Intraslab
226	IWTH030305261824-E	IWTH030305261824-N	Off Miyagi	2003	7	107.85	kik-net	Interface
227	IWTH031103111509-E	IWTH031103111509-N	Off Iwate	2011	7.4	78.72	kik-net	Interface
228	IWTH031104072332-E	IWTH031104072332-N	Off Miyagi - 2011	2011	7.1	173.20	kik-net	Intraslab
229	IWTH090305261824-E	IWTH090305261824-N	Off Miyagi	2003	7	134.82	kik-net	Interface
230	IWTH130305261824-E	IWTH130305261824-N	Off Miyagi	2003	7	122.15	kik-net	Interface

231	IWTH140806140843-E	IWTH140806140843-N	Iwate - Miyagi Nairiku	2008	6.9	100.08	kik-net	Interface
232	IWTH170305261824-E	IWTH170305261824-N	Off Miyagi	2003	7	94.47	kik-net	Interface
233	IWTH171104072332-E	IWTH171104072332-N	Off Miyagi - 2011	2011	7.1	158.95	kik-net	Intraslab
234	IWTH180305261824-E	IWTH180305261824-N	Off Miyagi	2003	7	79.18	kik-net	Interface
235	IWTH180806140843-E	IWTH180806140843-N	Iwate - Miyagi Nairiku	2008	6.9	65.61	kik-net	Interface
236	IWTH230508161146-E	IWTH230508161146-N	Honshu	2005	7.1	115.11	kik-net	Interface
237	IWTH230806140843-E	IWTH230806140843-N	Iwate - Miyagi Nairiku	2008	6.9	69.77	kik-net	Interface
238	IWTH270305261824-E	IWTH270305261824-N	Off Miyagi	2003	7	61.90	kik-net	Interface
239	IWTH270508161146-E	IWTH270508161146-N	Honshu	2005	7.1	107.34	kik-net	Interface
240	IWTH270806140843-E	IWTH270806140843-N	Iwate - Miyagi Nairiku	2008	6.9	45.67	kik-net	Interface
241	IWTH271104072332-E	IWTH271104072332-N	Off Miyagi - 2011	2011	7.1	108.11	kik-net	Intraslab
242	MYGH030508161146-E	MYGH030508161146-N	Honshu	2005	7.1	92.93	kik-net	Interface
243	MYGH030806140843-E	MYGH030806140843-N	Iwate - Miyagi Nairiku	2008	6.9	58.43	kik-net	Interface
244	MYGH031104072332-E	MYGH031104072332-N	Off Miyagi - 2011	2011	7.1	96.14	kik-net	Intraslab
245	MYGH040305261824-E	MYGH040305261824-N	Off Miyagi	2003	7	67.34	kik-net	Interface

246	MYGH040508161146-E	MYGH040508161146-N	Honshu	2005	7.1	105.09	kik-net	Interface
247	MYGH040806140843-E	MYGH040806140843-N	Iwate - Miyagi Nairiku	2008	6.9	41.59	kik-net	Interface
248	MYGH041104072332-E	MYGH041104072332-N	Off Miyagi - 2011	2011	7.1	102.40	kik-net	Intraslab
249	MYGH110305261824-E	MYGH110305261824-N	Off Miyagi	2003	7	66.87	kik-net	Interface
250	MYGH110508161146-E	MYGH110508161146-N	Honshu	2005	7.1	89.90	kik-net	Interface
251	MYGH110806140843-E	MYGH110806140843-N	Iwate - Miyagi Nairiku	2008	6.9	59.50	kik-net	Interface
252	MYGH120305261824-E	MYGH120305261824-N	Off Miyagi	2003	7	61.93	kik-net	Interface
253	MYGH120508161146-E	MYGH120508161146-N	Honshu	2005	7.1	88.99	kik-net	Interface
254	MYGH120806140843-E	MYGH120806140843-N	Iwate - Miyagi Nairiku	2008	6.9	58.45	kik-net	Interface

Appendix C

Soil profiles compiled in this study

Profiles originally compiled in this study

The soil profiles compiled in this study are presented in this section. For each soil profile, description, thickness, unit weight, and shear wave velocity (V_s) of the soil in each layer are given. The entry “NA” indicates that the information is not available.

C.1 Profile 01 – Seattle Fire Station #28, Washington

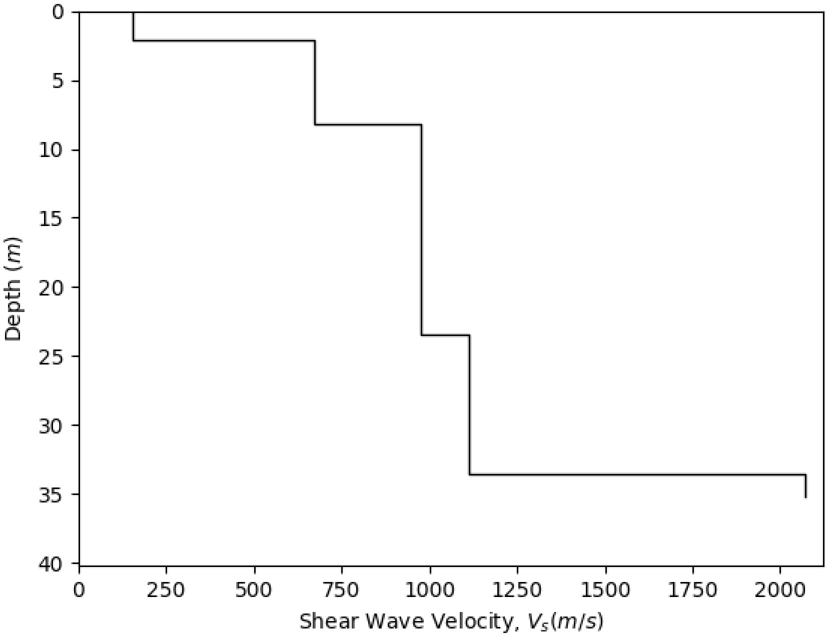

Fig C1. Shear wave velocity profile for Profile 01

Table C1. Layer properties for Profile 01

Layer description	Thickness (m)	Unit weight (kN/m^3)	V_s (m/s)
NA	2.13	17	152.5
NA	6.1	17	670.56
NA	15.24	18	975.36
NA	10.01	22	1112.52

C.2 Profile 02 – SEATAC Fire Station, Washington

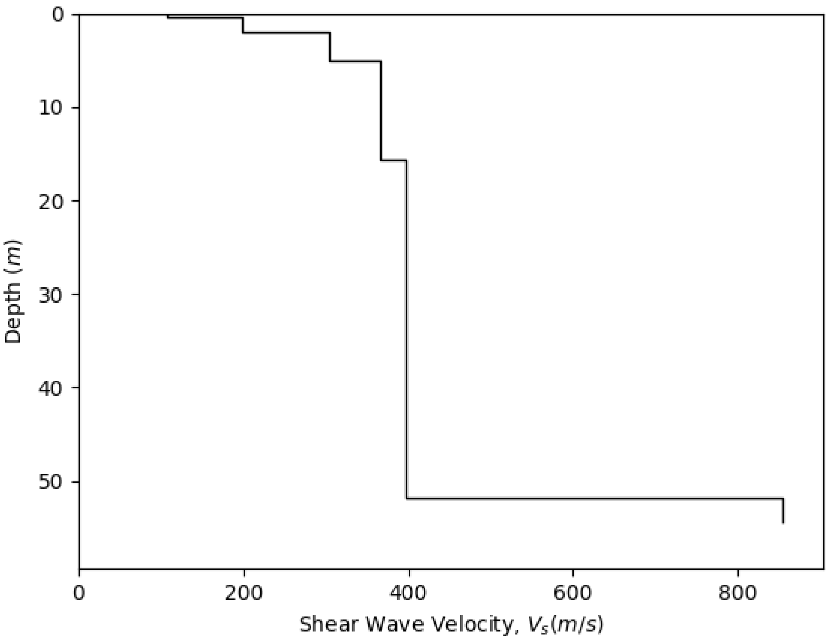

Fig C2. Shear wave velocity profile for Profile 02

Table C2. Layer properties for Profile 02

Layer description	Thickness (m)	Unit weight (kN/m^3)	V_s (m/s)
NA	0.46	16.5	106.68
NA	1.52	16.5	198.12
NA	3.05	17.5	304.8
NA	10.67	17.5	365.76
NA	36.12	17.5	396.24

C.3 Profile 03 – Echo Lake BPA station, Washington

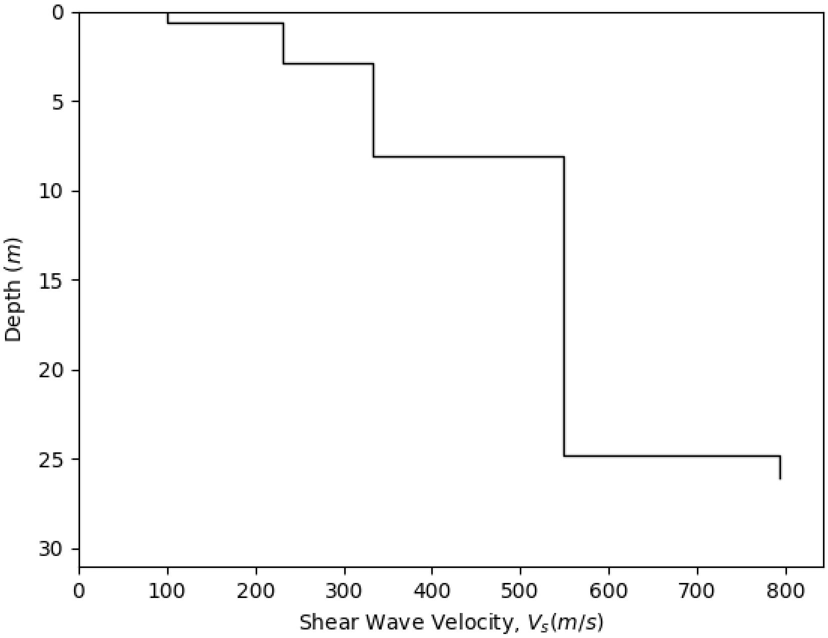

Fig C3. Shear wave velocity profile for Profile 03

Table C3. Layer properties for Profile 03

Layer description	Thickness (m)	Unit weight (kN/m^3)	V_s (m/s)
NA	0.6	16.5	100.6
NA	2.3	17	231.7
NA	5.3	17.5	332.3
NA	16.7	18	548.8

C.4 Profile 04 – Kitsap County Airport, Bremerton, Washington

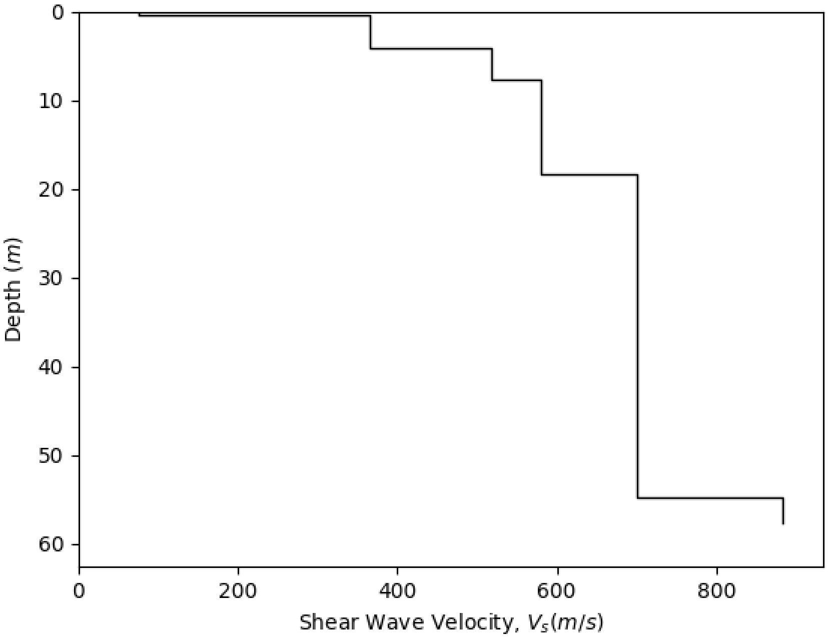

Fig C4. Shear wave velocity profile for Profile 04

Table C4. Layer properties for Profile 04

Layer description	Thickness (m)	Unit weight (kN/m^3)	V_s (m/s)
NA	0.43	16	76.2
NA	3.66	17.5	365.76
NA	3.66	18	518.16
NA	10.67	18	579.12
NA	36.454	19	701.04

C.5 Profile 05 – Monroe BPA Substation, Washington

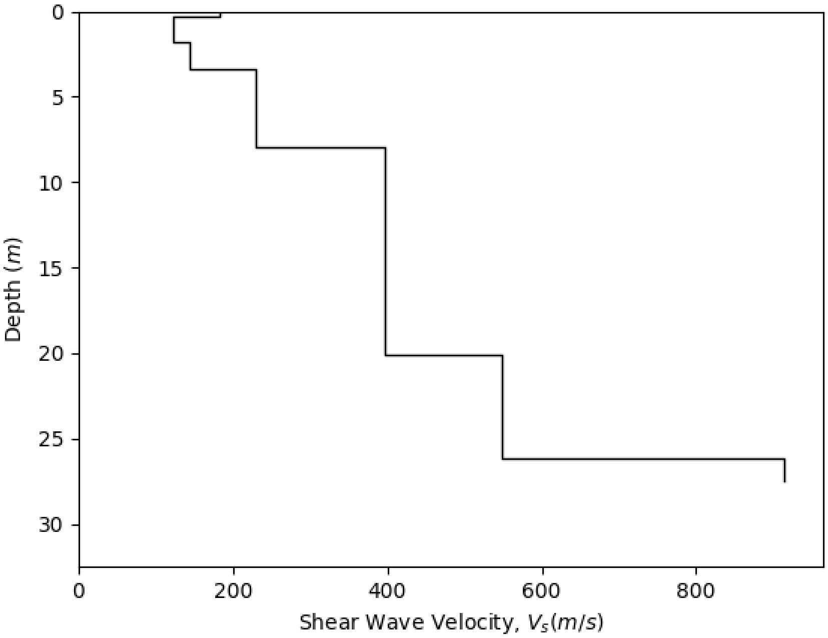

Fig C5. Shear wave velocity profile for Profile 05

Table C5. Layer properties for Profile 05

Layer description	Thickness (m)	Unit weight (kN/m^3)	V_s (m/s)
NA	0.3	16.5	182.88
NA	1.52	16.5	121.92
NA	1.52	16.5	143.26
NA	4.57	17	228.6
NA	12.19	17.5	396.24
NA	6.1	18	548.64

C.6 Profile 06 – Maple Valley, Renton, Washington

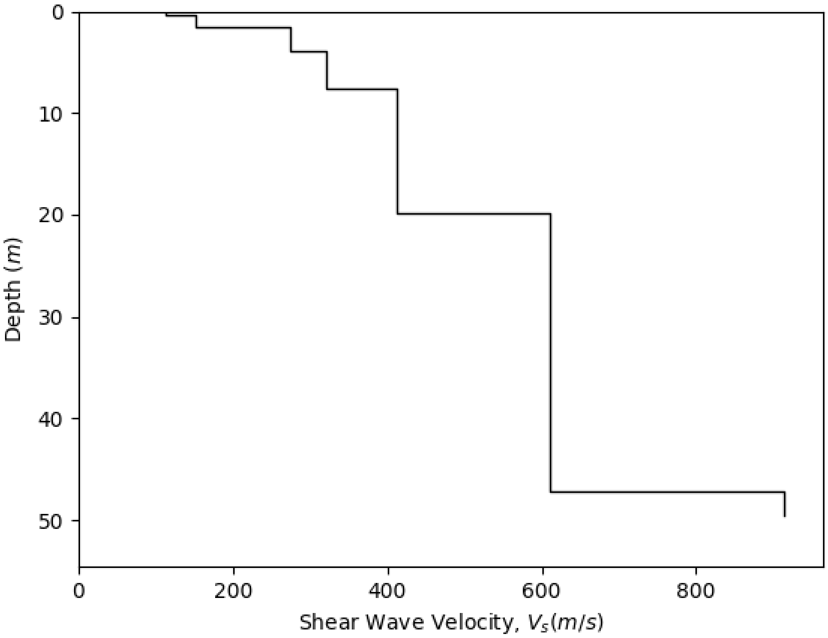

Fig C6. Shear wave velocity profile for Profile 06

Table C6. Layer properties for Profile 06

Layer description	Thickness (m)	Unit weight (kN/m^3)	V_s (m/s)
NA	0.3	16.5	112.78
NA	1.22	16.5	152.4
NA	2.44	17	274.32
NA	3.66	17.5	320.04
NA	12.19	17.5	411.48
NA	27.43	19	609.6

C.7 Profile 07 – Camp Murray, Tillicum, Washington

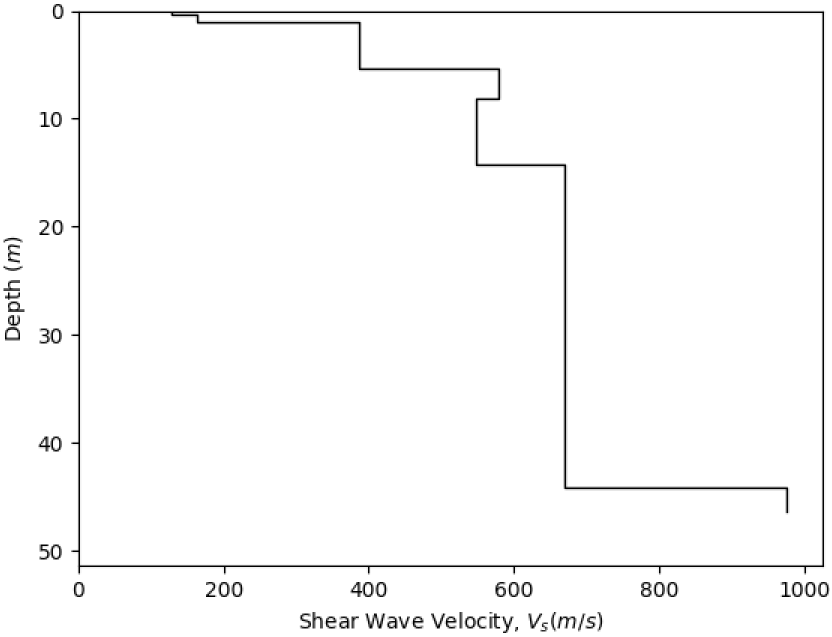

Fig C7. Shear wave velocity profile for Profile 07

Table C7. Layer properties for Profile 07

Layer description	Thickness (m)	Unit weight (kN/m^3)	V_s (m/s)
NA	0.3	16.5	128.016
NA	0.76	16.5	163.068
NA	4.27	17.5	387.096
NA	2.74	18	579.12
NA	6.1	18	548.64
NA	30.02	19	670.56

C.8 Profile 08 - Raver BPA Substation, Washington

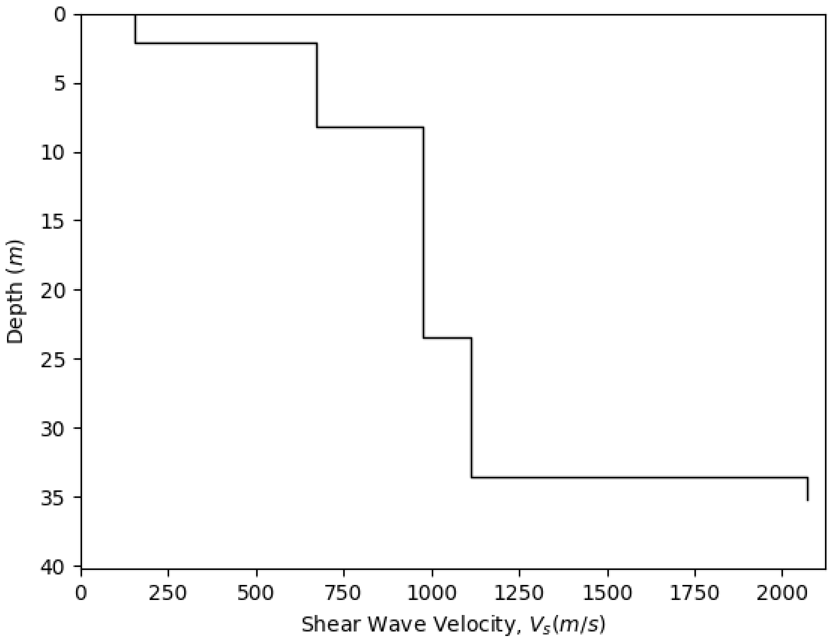

Fig C8. Shear wave velocity profile for Profile 08

Table C8. Layer properties for Profile 08

Layer description	Thickness (m)	Unit weight (kN/m^3)	V_s (m/s)
NA	2.14	16.5	152.4
NA	6.1	19	670.56
NA	15.24	20	975.36
NA	10.06	22	1112.52

C.9 Profile 09 – Hazelwood school, Renton, Washington

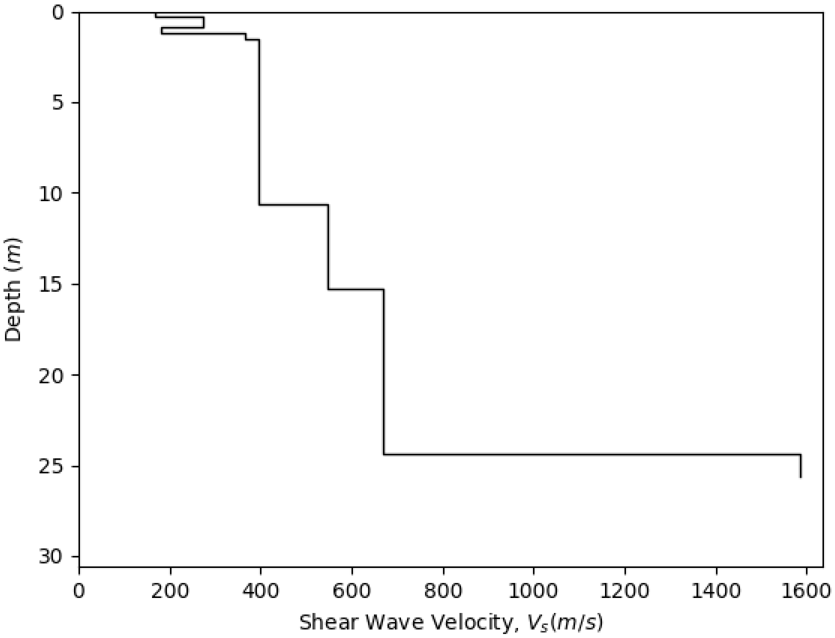

Fig C9. Shear wave velocity profile for Profile 09

Table C9. Layer properties for Profile 09

Layer description	Thickness (m)	Unit weight (kN/m^3)	V_s (m/s)
NA	0.3	16.5	167.64
NA	0.55	17	274.32
NA	0.37	16.5	182.88
NA	0.3	17.5	365.76
NA	9.14	17.5	396.24
NA	4.57	18	548.64
NA	9.14	19	670.56

C.10 Profile 10 – Seward Park, Seattle, Washington

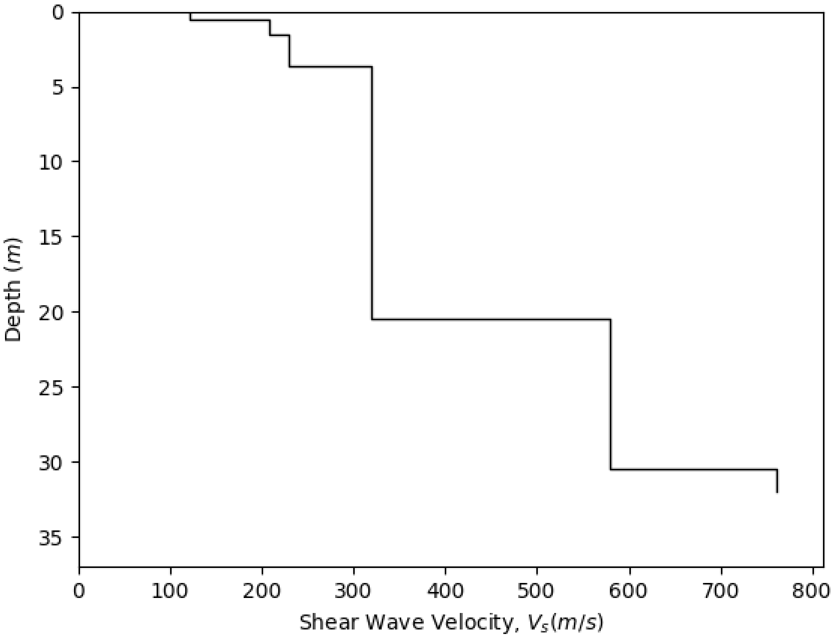

Fig C10. Shear wave velocity profile for Profile 10

Table C10. Layer properties for Profile 10

Layer description	Thickness (m)	Unit weight (kN/m^3)	V_s (m/s)
NA	0.52	16.5	121.92
NA	1.01	17	207.264
NA	2.14	17	228.6
NA	16.76	17.5	320.04
NA	10.06	18	579.12

C.11 Profile 11 – University of Puget Sound, Tacoma, Washington

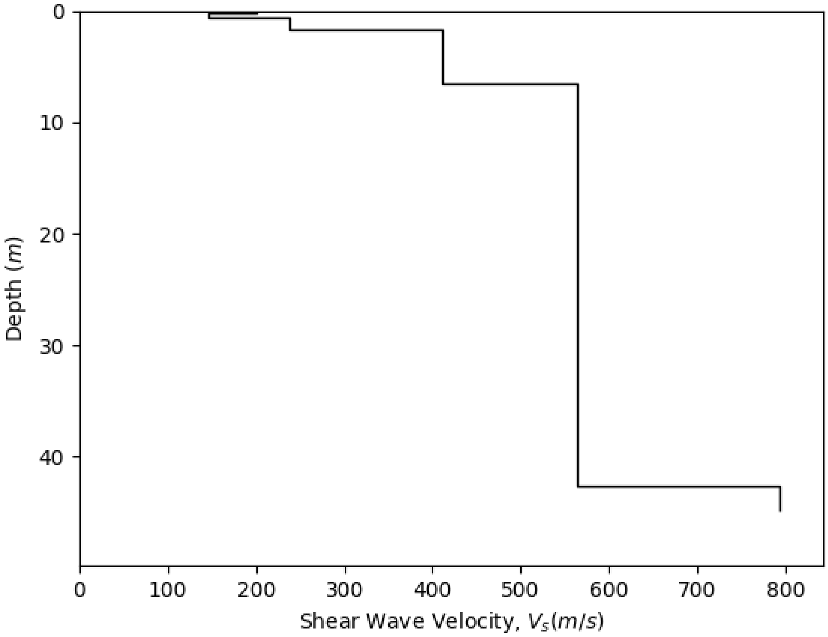

Fig C11. Shear wave velocity profile for Profile 11

Table C11. Layer properties for Profile 11

Layer description	Thickness (m)	Unit weight (kN/m^3)	V_s (m/s)
NA	0.15	17	201.168
NA	0.46	16.5	146.304
NA	1.07	17	237.744
NA	4.88	17.5	411.48
NA	36.12	18	563.88

C.12 Profile 12 – Wilburton Center, Bellevue, Washington

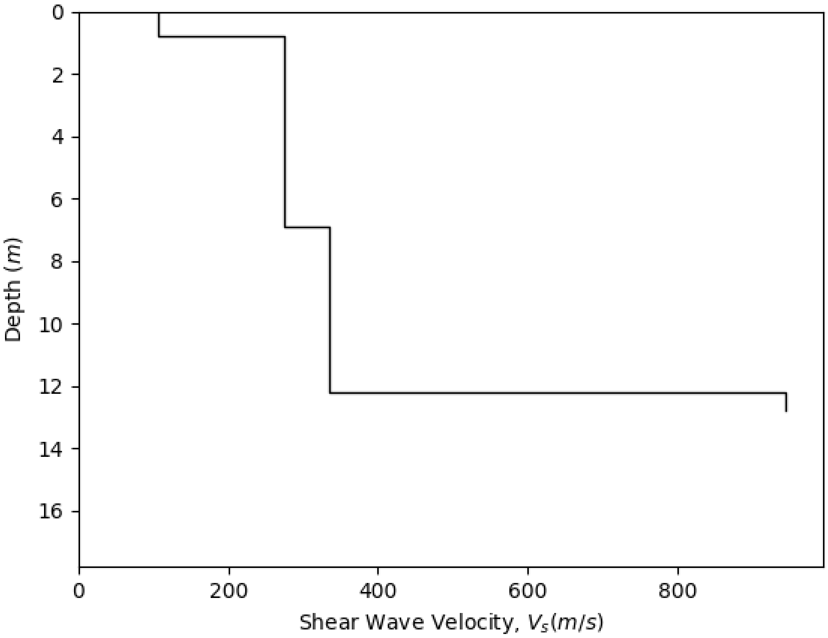

Fig C12. Shear wave velocity profile for Profile 12

Table C12. Layer properties for Profile 12

Layer description	Thickness (m)	Unit weight (kN/m^3)	V_s (m/s)
NA	0.79	16.5	106.68
NA	6.1	17	274.32
NA	5.3	17.5	335.28

C.13 Profile 13 – Arica Costanera, Chile

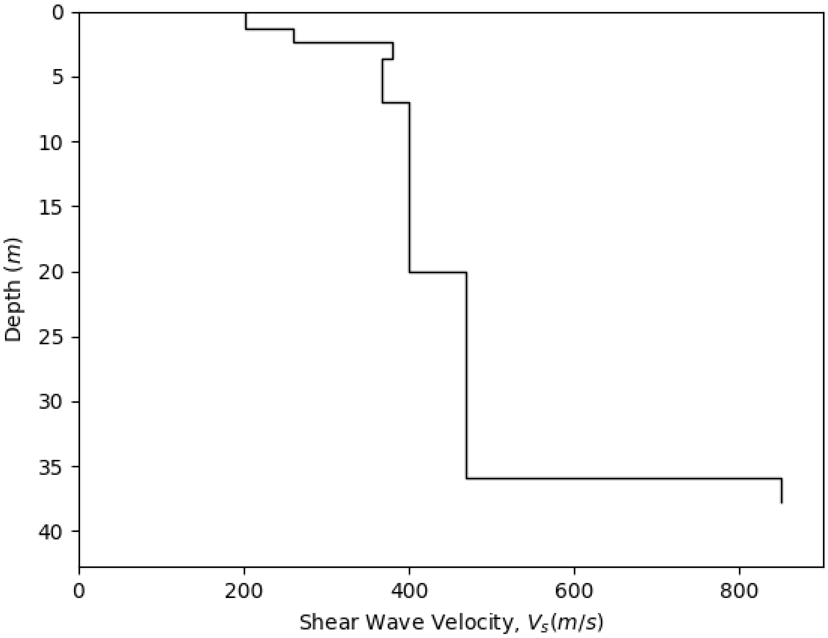

Fig C13. Shear wave velocity profile for Profile 13

Table C13. Layer properties for Profile 13

Layer description	Thickness (m)	Unit weight (kN/m^3)	V_s (m/s)
NA	1.27	18	201
NA	1.08	18	260
NA	1.25	18	380
NA	3.41	18	367
NA	13.02	18	399
NA	15.92	19.5	469

C.14 Profile 14 – Arica Casa, Chile

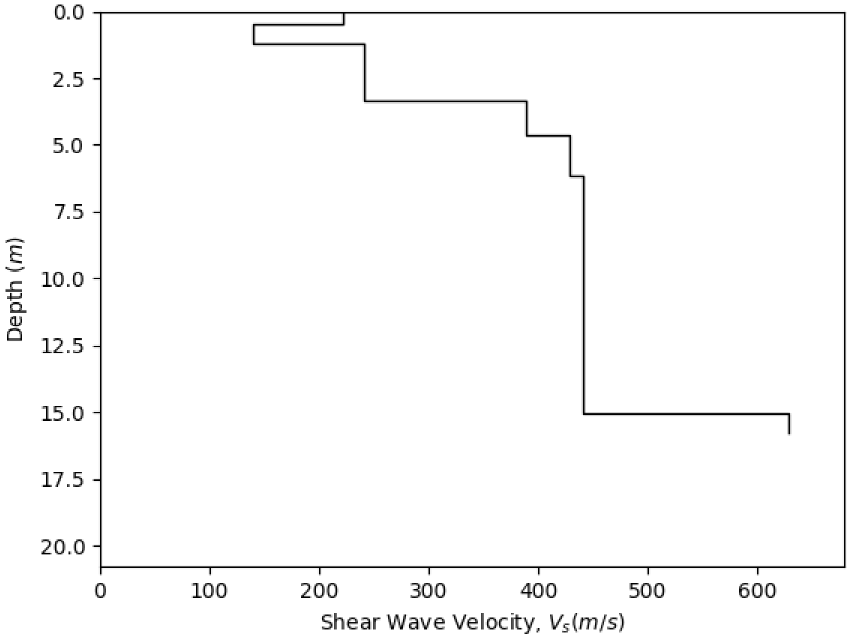

Fig C14. Shear wave velocity profile for Profile 14

Table C14. Layer properties for Profile 14

Layer description	Thickness (m)	Unit weight (kN/m^3)	V_s (m/s)
NA	0.5	18	222
NA	0.71	18	140
NA	2.14	18	241
NA	1.27	18	389
NA	1.52	19.5	429
NA	8.9	19.5	441

C.15 Profile 15 – Poconchile, Chile

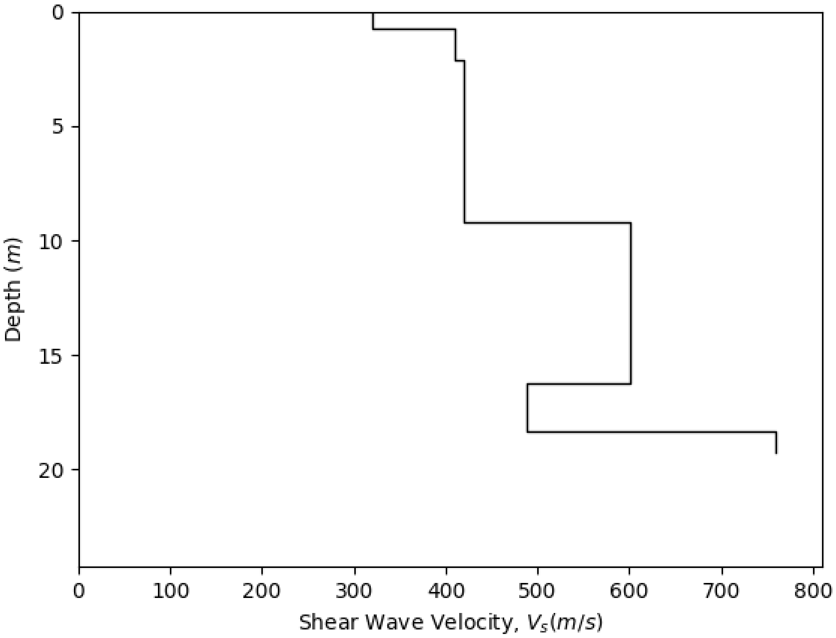

Fig C15. Shear wave velocity profile for Profile 15

Table C15. Layer properties for Profile 15

Layer description	Thickness (m)	Unit weight (kN/m^3)	V_s (m/s)
NA	0.725	18	320
NA	1.432	19.5	410
NA	7.08	19.5	420
NA	7.02	19.5	601
NA	2.08	19.5	489

C.16 Profile 16 – Moquegua, Peru

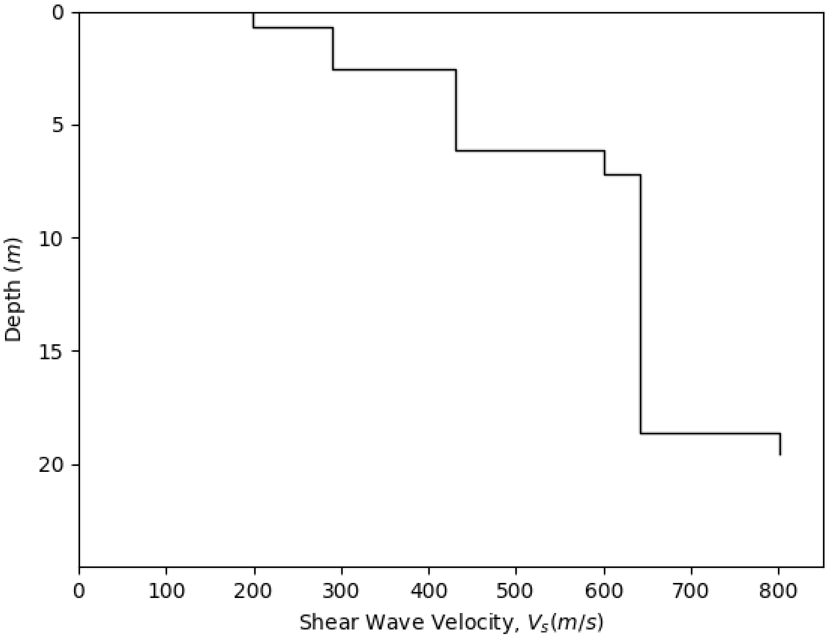

Fig C16. Shear wave velocity profile for Profile 16

Table C16. Layer properties for Profile 16

Layer description	Thickness (m)	Unit weight (kN/m^3)	V_s (m/s)
NA	0.68	18	199
NA	1.9	18	290
NA	3.55	19.5	430
NA	1.07	19.5	600
NA	11.42	19.5	641

C.17 Profile 17 - Tsuchiura, Ibaraki, Japan

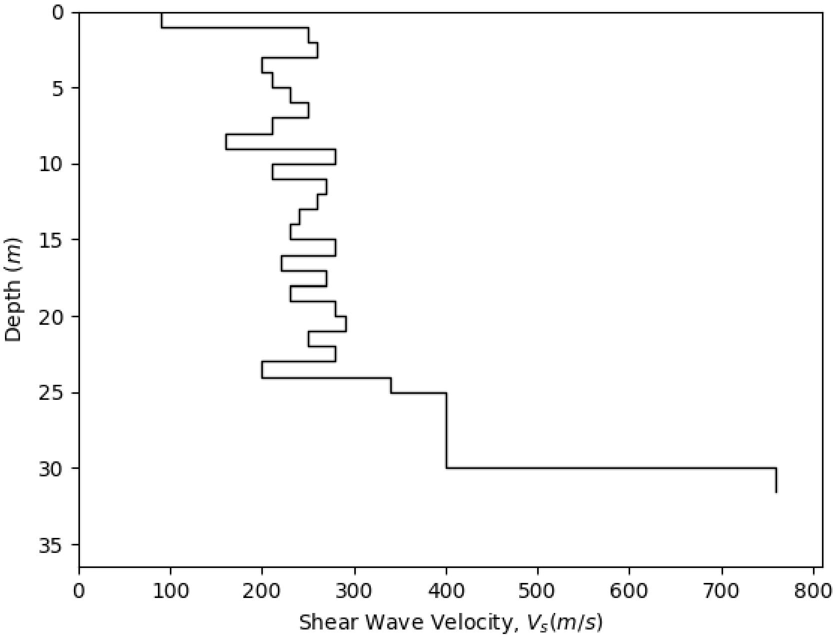

Fig C17. Shear wave velocity profile for Profile 17

Table C17. Layer properties for Profile 17

Layer description	Thickness (m)	Unit weight (kN/m^3)	V_s (m/s)
Clayey sand	1	16	90
Clayey sand	1	16	250
Clayey sand	1	17	260
Clayey sand	1	17	200
Clayey sand	1	17	210
Clayey sand	1	17	230
Clayey sand	1	17	250
Silt	1	17	210
Silt	1	17	160
Silt	1	17	280
Silt	1	17	210
Silt	1	17	270
Silt	1	17	260
Silt	1	17	240
Silt	1	17	230

Silt	1	17	280
Silt	1	18	220
Sand	1	18	270
Sand	1	18	230
Silt	1	18	280
Sand	1	18	290
Sand	1	18	250
Sand	1	18	280
Silt	1	18	200
Silt	1	18	340
Sand	1	18	400
Sand	1	18	400
Sand	1	18	400
Silt	1	18	400
Silt	1	18	400

C.18 Profile 18 – Sendai, Miyagi, Japan

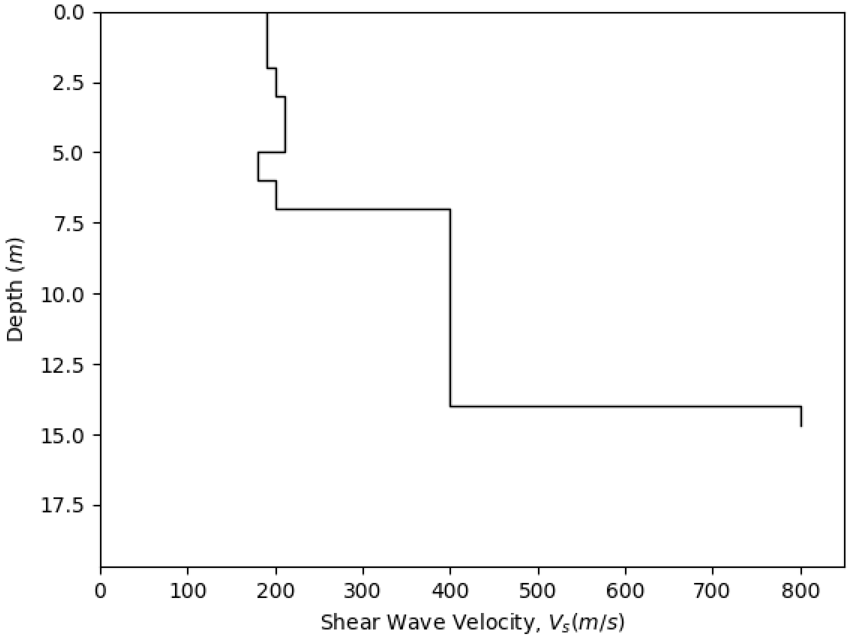

Fig C18. Shear wave velocity profile for Profile 18

Table C18. Layer properties for Profile 18

Layer description	Thickness (m)	Unit weight (kN/m^3)	V_s (m/s)
Organic silt	2	16	190
Sandy clay	1	18	200
Sandy clay	2	18	210
Gravel	1	21	180
Gravel	1	21	200
Gravel	7	21	400

C.19 Profile 19 – Ozu, Kumamoto, Japan

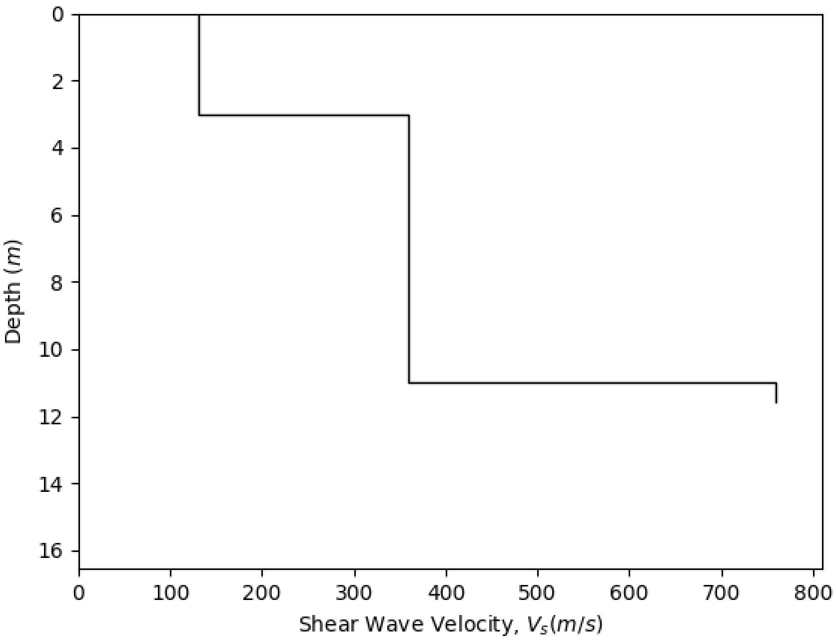

Fig C19. Shear wave velocity profile for Profile 19

Table C19. Layer properties for Profile 19

Layer description	Thickness (m)	Unit weight (kN/m^3)	V_s (m/s)
Fill	1	13.6	130
Sand	1	15.4	130
Sand	1	16.6	130
Sand	1	17.1	360
Sand	1	16.9	360
Sand	1	17.2	360
Volcanic Ash	1	17.8	360
Volcanic Ash	1	18.3	360
Volcanic Ash	1	18.1	360
Volcanic Ash	1	17.9	360
Volcanic Ash	1	17.9	360

C.20 Profile 20 – Takamori, Kumamoto, Japan

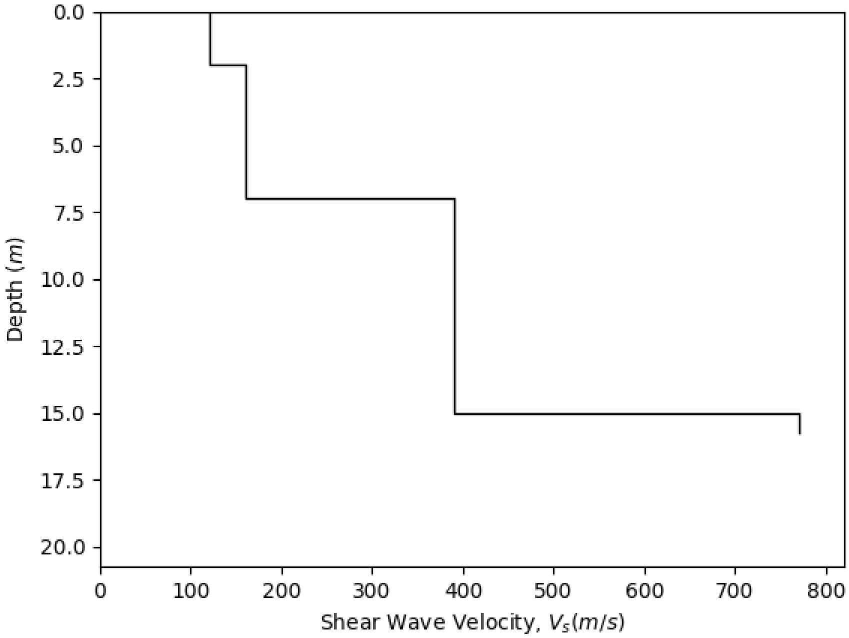

Fig C20. Shear wave velocity profile for Profile 20

Table C20. Layer properties for Profile 20

Layer description	Thickness (*m*)	Unit weight (kN/m^3)	V_s (*m/s*)
Volcanic ash	1	14.9	120
Volcanic ash	1	15.2	120
Volcanic ash	1	15.2	160
Volcanic ash	1	15.5	160
Volcanic ash	1	15.6	160
Volcanic ash	1	15.7	160
Volcanic ash	1	16.4	160
Volcanic ash	1	18	390
Volcanic ash	1	19.1	390
Volcanic ash	1	19.2	390
Volcanic ash	1	19.8	390
Volcanic ash	1	19.1	390
Volcanic ash	1	19.6	390
Volcanic ash	1	19.5	390
Volcanic ash	1	19.6	390

C.21 Profile 21 - Uto, Kumamoto, Japan

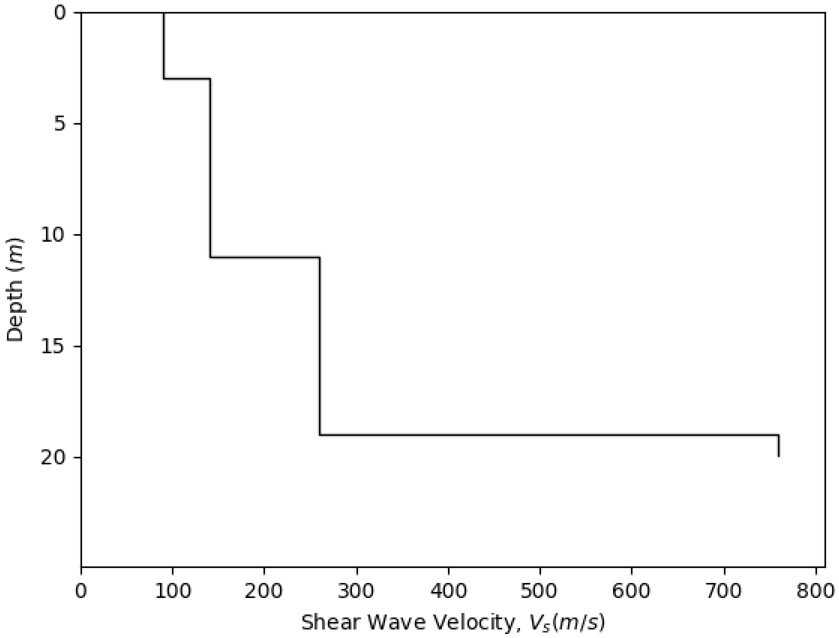

Fig C21. Shear wave velocity profile for Profile 21

Table C21. Layer properties for Profile 21

Layer description	Thickness (m)	Unit weight (kN/m^3)	V_s (m/s)
Fill soil	1	16.2	90
Clay	1	17	90
Clay	1	16.1	90
Sand	2	17.2	140
Volcanic ash	1	17.3	140
Volcanic ash	1	17.6	140
Volcanic ash	1	18.1	140
Volcanic ash	1	17.7	140
Volcanic ash	1	17.6	140
weathered rock	1	17.3	140
weathered rock	3	17.1	260
weathered rock	1	17.3	260
weathered rock	1	17.7	260
weathered rock	3	18.2	260

C.22 Profile 22 – Yamato, Kumamoto, Japan

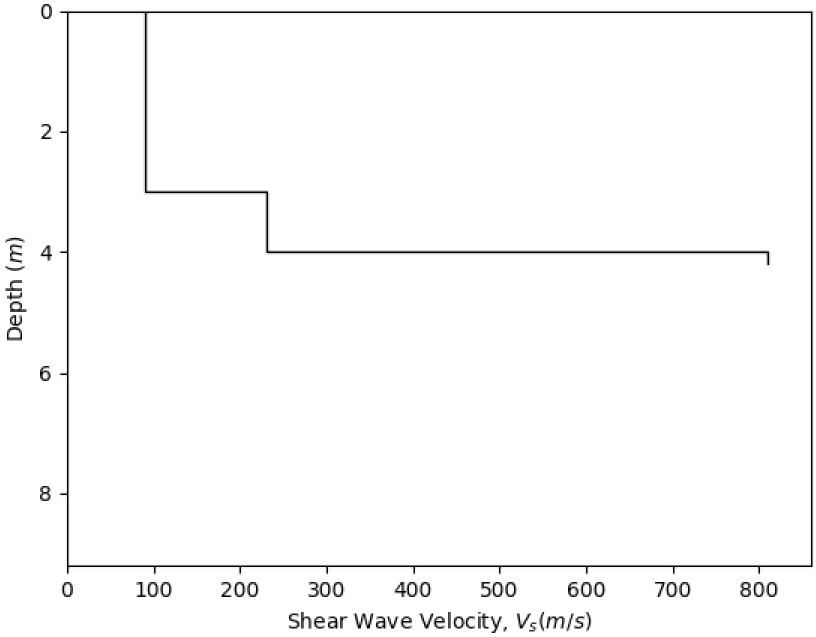

Fig C22. Shear wave velocity profile for Profile 22

Table C22. Layer properties for Profile 22

Layer description	Thickness (m)	Unit weight (kN/m^3)	V_s (m/s)
Fill soil	1	16.3	90
Clay	2	16.3	90
Gravel	1	20	230

C.23 Profile 23 – Misato, Kumamoto, Japan

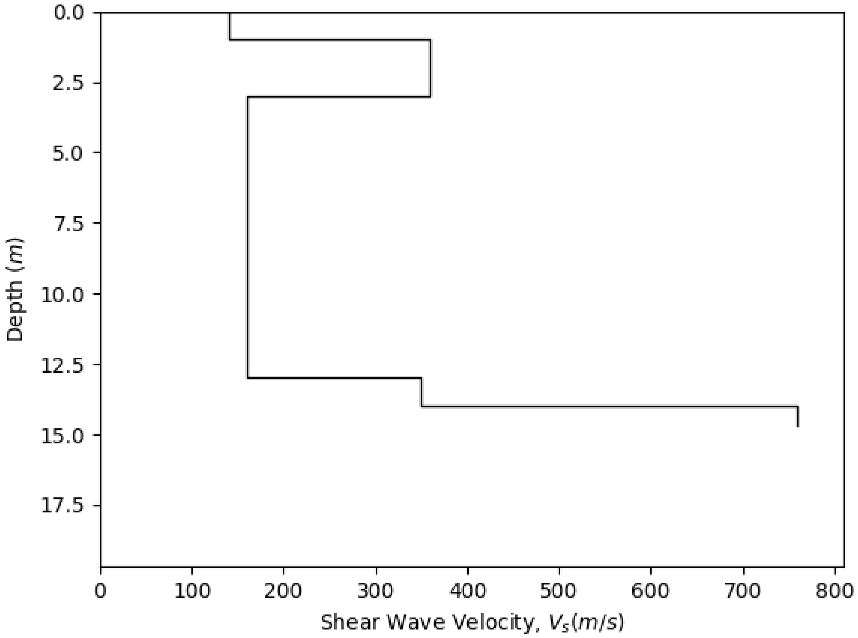

Fig C23. Shear wave velocity profile for Profile 23

Table C23. Layer properties for Profile 23

Layer description	Thickness (m)	Unit weight (kN/m^3)	V_s (m/s)
Fill soil	1	16.2	140
Fill soil	1	17.1	360
Gravelly soil	1	16.6	360
Volcanic ash	1	15.8	160
Volcanic ash	1	15.1	160
Volcanic ash	1	15.9	160
Volcanic ash	1	16.7	160
Volcanic ash	1	16.3	160
Volcanic ash	1	17	160
Volcanic ash	1	16.9	160
Volcanic ash	1	17.4	160
Volcanic ash	1	16.7	160
Volcanic ash	1	17.3	160
Weathered rock	1	21.6	350

C.24 Profile 24 – Onahama Port, Iwaki, Japan

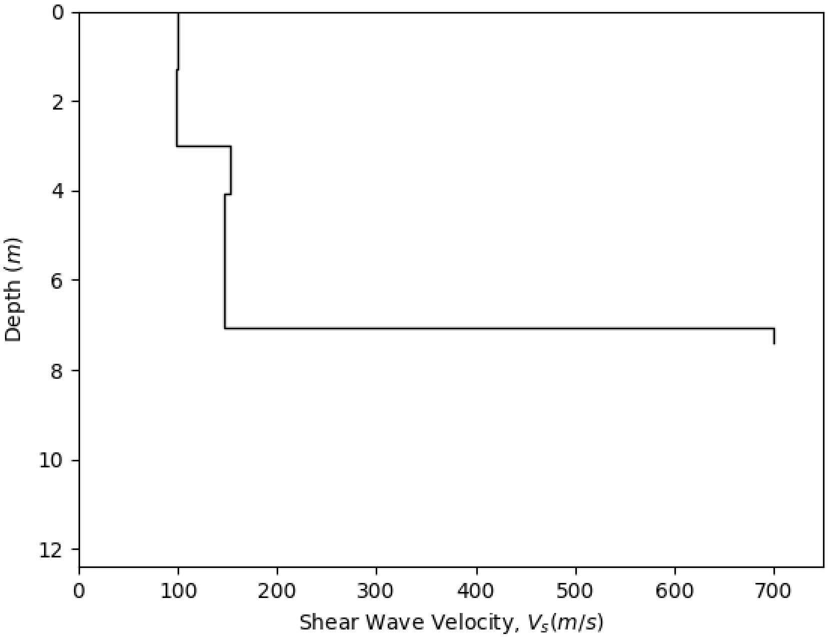

Fig C24. Shear wave velocity profile for Profile 24

Table C24. Layer properties for Profile 24

Layer description	Thickness (m)	Unit weight (kN/m^3)	V_s (m/s)
NA	1.3	15	100
NA	1.7	17	99
NA	1.06	18	152
NA	3	18	146

C.25 Profile 25 – Port Island, Hyogo, Japan

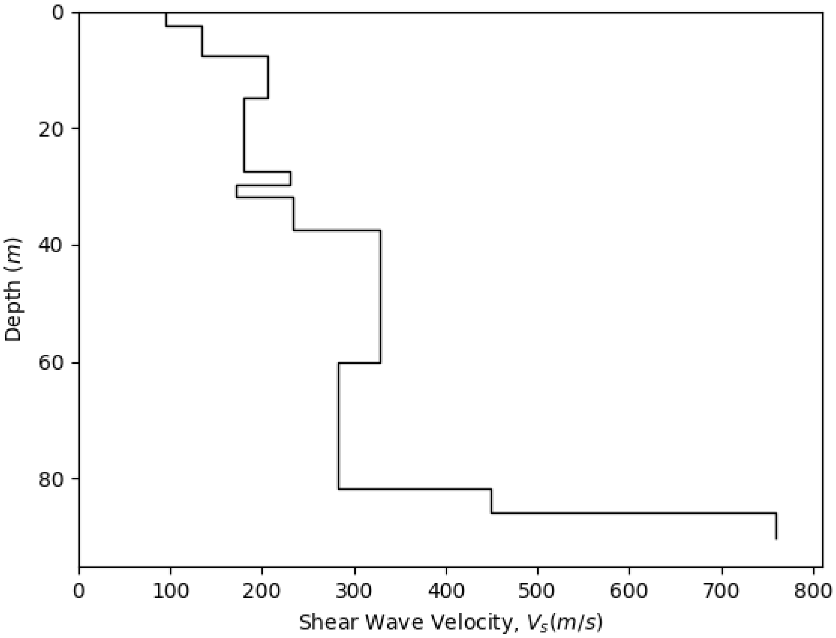

Fig C25. Shear wave velocity profile for Profile 25

Table C25. Layer properties for Profile 25

Layer description	Thickness (m)	Unit weight (kN/m^3)	V_s (m/s)
Saturated sandy gravel fill	2.46	19	94
Saturated sandy gravel fill	5.12	19	134
Sand with gravel fill	7.23	19	206
Alluvial clay, alluvial sand	12.66	16.5	180
Alluvial sand	2.34	19	231
Alluvial sand and oiluvial sand with gravel layers	1.92	19	172
Oiluvial sand with gravel	5.75	19	233
Oiluvial sand with gravel and Oiluvial clay layers	22.55	19	328
Sand with gravel	21.61	19	282

Sand with gravel	4.26	19	449

C.26 Profile 26 – Sakaiminato, Tottori, Japan

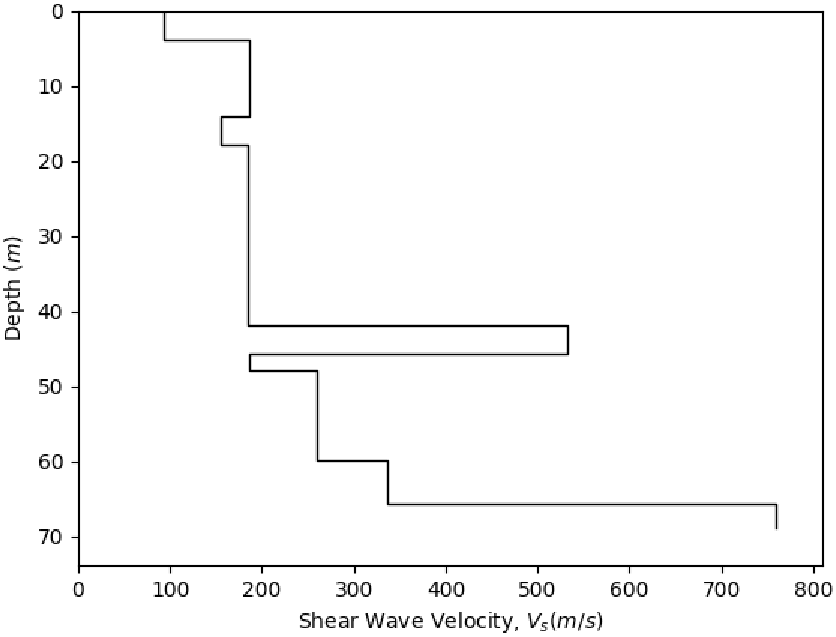

Fig C26. Shear wave velocity profile for Profile 26

Table C26. Layer properties for Profile 26

Layer description	Thickness (*m*)	Unit weight (kN/m^3)	V_s (*m/s*)
Silty sand	3.90	17	93
Silty sand, silt, and clay layers	10.10	17	186
Clay	3.96	16	155
Clay and silty sand	23.85	16	185
Silty sand	3.93	17	533
Clay	2.14	16	186
Clay, silty sand, and clay layers	11.98	16	259
Silt, silty sand, and silt layers	5.77	18	337

C.27 Profile 27 – Osato, Miyagi, Japan

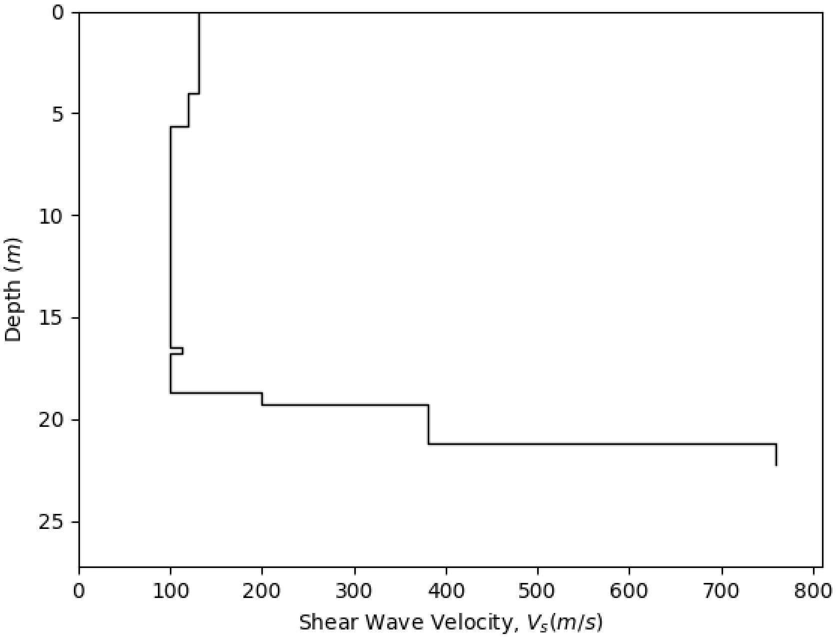

Fig C27. Shear wave velocity profile for Profile 27

Table C27. Layer properties for Profile 27

Layer description	Thickness (*m*)	Unit weight (kN/m^3)	V_s (*m/s*)
Clay	2.5	16	130
Sand,5-15%Clay	1.5	19	130
Clay	0.3	16.5	120
Sand,5-15%Clay	1.3	19	120
Clay	10.9	16.5	100
Sand	0.3	19	113
Peat	1.1	14	100
Clay	0.8	16	100

Appendix D

R code for mixed effects regression and bootstrapping

D.1. Required packages

This section documents the regression code written in R programming language, that was used to develop the models proposed in this study. R interpreter can be downloaded from https://www.r-project.org/

First, the required packages need to be installed and imported.

```
install.packages(c('lme4','dplyr', 'iterators','foreach', 'broom','bazar',
'tictoc'))

library('lme4')

library('dplyr')

library('iterators')

library('foreach')

library('broom')

library('bazar')

library('tictoc')
```

Next, the site response data should be loaded.

```
df<-read.csv("Site response data.csv",header = TRUE)
```

D.2. n_{eq} regression

The model for number of equivalent cycles is linear and therefore is developed using linear mixed effects regression. The regression can be implemented using the function `lmer`. `(1|type/EQ)` indicates the nested random effect corresponding to the event type (i.e., Interface or Intraslab) and earthquake events. `(1|Profile)` indicates the random effect corresponding to soil profiles. `summary(model_neq)` provides the summary of the fitted model with all the coefficients and their standard errors. The random effects (i.e., the event term and the site term) can be accessed using `ranef(model_neq)`

```
model_neq<-lmer(ln_neq ~ Magnitude + ln_amax + ln_Vs30 + (1|type/EQ) + (1|Profile), data = df)

summary(model_neq)

ranef(model_neq)
```

D.3. r_d regression

The model for stress reduction factor is non-linear and therefore is developed using non-linear mixed effects regression. The regression can be implemented using the function ‘nlmer’.

As opposed to ‘lmer’, ‘`nlmer`’ requires a set functional form and initial values for all the coefficients. `parnames_rd_fun` sets up the regression coefficients in the model. `startval_rd_fun` gives the starting values for each coefficient to be used in the regression. These starting values play an important role in the convergence of regression results. Values that are too far off from the true values will result in non-convergence. A good practice is to start with values from coefficients values stated in the literature and vary them. Another approach will be performing a generalized regression to obtain a good starting estimate for the coefficients. Finally, the functional form for the model is established using the `deriv()` function.

```
parnames_rd_fun <- c("b1","b2","b3","b4","b5","b6","b7","b8")


startval_rd_fun = c(b1 = 2.0235, b2 = 0.7787, b3 = 0.6226,
                    b4 = -0.0836, b5 = 0.1173, b6 = 0.1513,
                    b7 = 0.048, b8 = -0.0015)
```

```
rd_fun_deriv = deriv(expression(1-(b1+b4*Magnitude+b5*ln_amax+
                                     b8*Vs12)/
                                  (1 + exp(-(log(Depth)-(b2+b6*Magnitude))/(b
3+b7*Magnitude)))),
                     namevec = parnames_rd_fun,
                     function.arg = c(parnames_rd_fun,"Magnitude","ln_amax","
Vs12","Depth"))
```

The regression can then be performed using ‘nlmer’.

```
model <- nlmer(rd ~ rd_fun_deriv(b1,b2,b3,b4,b5,b6,b7,b8,Magnitude,ln_amax,Vs
12,Depth) ~ (b1|type/EQ) + (b1|Profile) ,
                 data=df, start = startval_rd_fun, verbose=FALSE)

summary(model_rd)

ranef(model_rd)
```

D.4. Bootstrapping

To perform bootstrapping, 10,000 points are selected in random from the site response data and the regression are performed with the selected subset. This process is repeated for 1000 times. Then the mean and standard deviation of the coefficients from each iteration are computed.

The model for n_{eq} is simple and does not require starting values for coefficients. There, bootstrapping for n_{eq} model can be done using a simple ‘for’ loop. However, the model for r_d is a little more involve and requires starting values. The r_d model will run into convergence errors very often and therefore, a simple ‘for’ loop would not suffice. To handle the convergence errors with any arbitray iteration, `foreach` package in R offers a solution. Also note that the approach with `foreach` can be applied for the n_{eq} model as well.

```
sample_size = 10000


#This is the bootstrap command - icount is the number of iterations,
errorhandling removes failed iterations
```

```r
x = foreach(icount(1000), .combine = 'rbind', .packages='lme4',.errorhandling = 'remove') %dopar% {

  df_sample = df[sample(nrow(df), sample_size), ]

  model <- nlmer(rd ~ rd_fun_deriv(b1,b2,b3,b4,b5,b6,b7,b8,Magnitude,ln_amax,Vs12,Depth) ~ (b1|type/EQ) + (b1|Profile) ,
                 data=df_sample, start = startval_rd_fun, verbose=FALSE)
#Model for rd



  model<-lmer(ln_neq ~ Magnitude + ln_amax + ln_Vs30 + (1|type/EQ) + (1|Profile), data = df_sample) #Model for neq


  #This makes the exported row of results for the bootstrap dataframe

  {

    name = i

    bic = BIC(model)

    aic = AIC(model)

    loglik = summary(model)$logLik[1]

    aic_bic_loglik = data.frame(c(aic,bic,loglik),row.names = c('AIC','BIC','LogLikelihood'))

    colnames(aic_bic_loglik) = name

    coefficents = data.frame(fixef(model))

    colnames(beta) = name

    ref = as.data.frame(VarCorr(model))[,c('grp','sdcor')]

    ref <- data.frame(ref[,-1], row.names = ref[,1])

    row.names(ref) = paste0(row.names(ref), '_StDev')

    result = data.frame(t(rbind(aic_bic_loglik,coefficents,ref)))

    colnames(result) = gsub('X', '', colnames(result))


  }
```

```
  result #dataframe with all iteration results
}

summary = rbind(apply(x, 2, mean), apply(x, 2, sd)) #Computes the mean and standard deviation of the coefficients
```